Advancements in Optical Coherence Tomography: Innovations and Applications for Ophthalmology and Dermatology

Jie Lu

A dissertation
submitted in partial fulfillment of the
requirements for the degree of

Doctor of Philosophy

University of Washington
2023

Reading Committee:

Ruikang K. Wang (Chair)
Matthew O'Donnell
Nina Lu

Program Authorized to Offer Degree:
Bioengineering

University of Washington

Abstract

Advancements in Optical Coherence Tomography: Innovations and Applications for Ophthalmology and Dermatology

Jie Lu

Chair of the Supervisory Committee:

Ruikang K. Wang

Bioengineering

Optical coherence tomography (OCT) is a well-established imaging modality widely used in ophthalmology and is emerging as a valuable clinical tool in dermatology. OCT angiography (OCTA), an advanced extension of OCT, utilizes intrinsic blood flow movement to generate angiographic images beneath the tissue surface, eliminating the need for contrast agents. This thesis demonstrates the capabilities of OCT in high-resolution imaging of 3D structures and microvasculature in the human eye and skin under diverse conditions.

The opening chapter of this thesis serves as an introduction to OCT technology, providing a foundation for the subsequent chapters. In Chapter 2, we delve into novel algorithms and methods developed for OCT imaging. We begin with a straightforward yet highly effective approach for estimating the optical attenuation coefficient (OAC) from OCT images. OAC not only enhances OCT imaging contrast but also serves as a valuable physical parameter for assessing tissue properties, as alterations in tissue morphology and content can impact OAC. Building on this, we leverage the OAC to enhance OCT imaging contrast,

leading to the development of algorithms for more precise and efficient segmentation of epidermal thickness in the OCT imaging of skin tissue, and retinal pigment epithelium (RPE) and calcified drusen in the imaging of retina tissue. Additionally, we introduce TransUnet, an innovative deep learning-based method developed for accurate segmentation of the outer retinal layer (ORL). Through this progressive exploration of OCT technology and advanced algorithms, our research significantly improves imaging segmentation and analysis in OCT clinical applications.

Building on this foundation, Chapter 3 showcases the remarkable capabilities and potentials of OCT in clinical ophthalmology. Firstly, we investigate the symmetry of interocular choroidal thickness and vascularity index measurements in normal eyes using SS-OCT, finding choroidal differences between normal fellow eyes in adults without obvious pathology. This study aids clinicians and researchers in distinguishing expected asymmetric changes in normal eyes from changes associated with diseases. Secondly, we examine variations in the ORL thickness among different stages of age-related macular degeneration (AMD), revealing significant differences in ORL thickness measurements among various AMD stages, indicating the potential of ORL thickness as an independent biomarker for predicting AMD progression.

Lastly, in Chapter 4, we discuss the clinical applications of OCT for dermatology. Firstly, we integrate pressure sensors with a handheld probe to facilitate imaging of micro vasculature, addressing the challenge of uncontrollable mechanical stress during contact mode imaging of the skin. This handheld scanning probe with built-in pressure sensors provides real-time feedback to control the mechanical stress, enabling repeatable and reliable OCTA images for a more accurate investigation of skin conditions. Secondly, we employ a clinical-prototype OCT system to image severe burn wounds at multiple scan sites across two time points. Quantitative analysis of vascular area density and surface roughness offers key insights into the pathophysiological mechanisms responsible for wound healing, potentially serving as critical biological indicators in future clinical evaluation and monitoring of wound healing. Lastly, we demonstrate the potential of OCT alongside OCTA to non-invasively image and

monitor human skin graft health and integration over time, providing valuable insights for wound healing monitoring after skin graft surgery.

In conclusion, this thesis contributes to the advancement of OCT technology through the development of novel algorithms and its applications in clinical ophthalmology and dermatology. The research presented here significantly enhances imaging segmentation and analysis in OCT and offers valuable insights for disease diagnosis and monitoring in ophthalmology and wound healing evaluation in dermatology.

Table of Contents

List of Figures

List of Tables

Acknowledgement

First and foremost, I would like to express my sincere gratitude and appreciation to my advisor, Dr. Ruikang (Ricky) Wang. I am deeply grateful that he accepted me as his PhD student and recognized my potential, even though I lacked an engineering background at the time. Dr. Wang has been a constant source of support since I joined Wang's Lab. He not only provided me with an excellent research environment but also mentored me by setting a great example. His emphasis on productivity and persistence has shaped me into a dedicated researcher.

Next, I would like to extend my heartfelt thanks to my supervisory committee members, Dr. Marco Salviato, Dr. Nina Lu, Dr. Matthew O'Donnell, Dr. Azadeh Yazdan-Shahmorad. I am immensely grateful for the time they dedicated to me and their valuable suggestions that greatly contributed to the completion of my thesis.

I would also like to express my deep appreciation to my collaborators and mentors: Dr. Philip J Rosenfeld from Bascom Palmer Eye Institute, whose expertise in age-related macular degeneration and logical research mindset have been instrumental in my development; and Dr. Steven Jacques, whose profound understanding of optics engineering and clear research approach have expanded my knowledge of optical properties.

Furthermore, I am indebted to my colleagues, Dr. Anthony Deegan and Dr. Geng Wang. I vividly remember the invaluable support they provided when I initially joined Wang's Lab. Dr. Geng Wang's exceptional patience in teaching me coding and Dr. Deegan's generous assistance in drafting scientific manuscripts, despite my limited prior experience, have made a significant impact on my growth as a researcher. Additionally, I extend my deepest appreciation to Dr. Nhan Le, Dr. Peijun Tang, Dr. Qinqin Zhang, Dr. Zhongdi Chu, Dr. Yuandong Li, Dr. Hao Zhou, Yuxuan Cheng, Zhiying Xie, Xiao Zhou, Teng Liu, Ziyu Liu, Dr. Mengxi Shen, Dr. Farhan E. Hiya, Yuxin Xia and Qing Chao for their professional and personal support. I cherish the fond memories we shared and wish each of them the very best.

Last but certainly not least, I would like to express my heartfelt gratitude to my husband, Dr. Jianyu Huang, and parents, Mr. Guosen Lu and Mrs. Weiqin Zhang. Their unconditional love and support have been a constant source of encouragement and strength. Without them, I do not believe I could have been able to reach this point. Thank them from the bottom of my heart.

1 Chapter 1. Introduction

1.1 Significance and research motivation

Optical coherence tomography (OCT) is a well-established depth-resolved imaging technique, generating images through the time delay and magnitude of light echoes in a similar way to how ultrasonography utilizes sound waves to image tissue structures (1,2). It can generate cross-sectional images of biological tissues in vivo, enabling the visualization of 3D microanatomical information with a field of view (FOV) spanning from a few to tens of square centimeters, a high resolution from 1 to 20 um, and a relatively remarkable imaging depth extending up to approximately 2 mm (1,2). Due to its non-invasive, cellular-level resolution and real-time capabilities, OCT has rapidly expanded and is currently widely used in ophthalmology and dermatology (3,4). This thesis aims to amplify the impact of OCT on clinical practice.

In the field of ophthalmology, age-related macular degeneration (AMD) is a leading cause of permanent vision loss among individuals aged 50 and above (5,6). Vision loss is typically associated with the late-stage AMD, which manifests as geographic atrophy (GA) and/or exudative AMD (6). While intraocular injection of vascular endothelial growth factor (VEGF) inhibitors can resolve the exudation associated with neovascularization in AMD (7), there is currently no effective treatment available to stop the formation or progression of GA (8). Most recently, the U.S. Food and Drug Administration (FDA) has approved first treatment for slowing the rate of GA growth. Nevertheless, there remains an urgent imperative to identify early, clinically measurable markers that can function as biomarkers for predicting eyes at the highest risk of GA progression, particularly in the context of clinical trials aimed at early intervention and disease prevention. The widespread utilization of optical coherence tomography (OCT) in ophthalmology has significantly facilitated the identification of OCT biomarkers associated with the transition from early to late AMD. These biomarkers include the central drusen volume (9–11)·(12), the presence of calcified/refractile drusen (13,14), hyperreflective foci (15–17), reticular pseudodrusen (17–19), choroidal thinning (20), and outer retinal atrophy (including photoreceptor degeneration) (19,21,22). Hence, one of the objectives of this thesis is to automate the identification and segmentation of calcified drusen and the outer retinal layer, thereby enabling a comprehensive assessment of AMD progression. Additionally, this thesis endeavors to establish a baseline for interocular asymmetry within healthy eyes. This baseline serves as a valuable resource for clinicians and researchers, aiding in the discrimination between pathological disparities and natural physiological variations.

In the field of dermatology, according to the World Health Organization (WHO), every year burn wounds result in approximately 180, 000 deaths and nearly 11 million injuries that require medical treatment worldwide (23). Despite such a high incidence and the major advances in therapeutic strategies for severe burn wounds, clinicians and researchers are still in need of a non-invasive imaging tool capable of accurately assessing the burn wound. Currently, clinical evaluation and healing assessments are largely based on wound appearance, sensitivity to pin prick, and blood refill (24), which have an accuracy rate of only 60 – 75%, even with an experienced burn surgeon (24). Laser Doppler imaging is at times used to aid assess blood perfusion of burns, but laser Doppler imaging is difficult to detect detailed vascular morphology due to its limited resolution and is not able to provide direct depth and structural information (25–27). Biopsies are at times considered a suitable alternative for assessing burn wounds, but obvious shortcomings, such as additional damage to an already severely traumatized skin, limit the use of such an invasive technique in the wound evaluation. Skin autografting is a form of reconstructive surgery that involves the transfer of skin from a healthy donor site to a recipient site in a need of repair on the same person. It has been widely used as a treatment strategy to improve the quality of life for patients suffering from burn damage. OCT has the potential to serve as an imaging tool that can address the various limitations of current assessment techniques, thereby enhancing the evaluation and monitoring of burn wound healing and the integration of skin autografts. To minimize the external force applied to the skin surface during OCT contact imaging and enable non-invasive OCT imaging of burn wound healing, this thesis initially introduces the integration of a pressure sensor with an OCT handheld probe. Subsequently, the objectives of this thesis encompass demonstrating OCT potential in assessing burn wound healing, visualizing and monitoring the integration of skin autografts, and exploring the physiological mechanisms underlying human wound healing.

1.2 Optical Coherence Tomography

The fundamental principle underlying OCT is based on low coherence interferometry. In simple terms, the light emitted from the light source is divided into two paths: the reference arm and the sample arm. The reference arm travels to the reference mirror, reflects back, while the sample arm travels to the sample and reflects back from different depths within it. Subsequently, the reflected light from both arms is combined, resulting in observable interference when the optical path lengths of the two arms matches.

Currently, there are two implementations of OCT: time-domain OCT (28) and Fourier domain OCT (FD-OCT) (29). FD-OCT offers distinct advantages in sensitivity and imaging speed compared to time-domain OCT (30). Although the concept of using OCT in biomedical imaging was proposed in the 1990s (1), it was

the introduction of FD-OCT that sparked the recent development of a wide range of OCT applications in various fields.

According to FD-OCT theory, the spectral power amplitude of the backscattered wave corresponds to the Fourier transform of the axial distribution of the object's scattering property. One significant advantage of FD-OCT over time-domain OCT is that it acquires depth information from the sample simultaneously, eliminating the need to move the reference mirror. This results in improved system sensitivity for measuring backscattered light, typically exceeding 20 dB compared to time-domain OCT. This advantage enables faster imaging speed while using limited light power, as dictated by laser safety standards, for imaging living tissue.

The high speed of FD-OCT systems has facilitated the imaging of not only tissue structure but also the investigation of functional parameters. For example, OCT-based angiography (OMAG) allows in vivo blood flow imaging without the need for exogenous agents, utilizing the inherent contrast provided by the endogenous light scattering from moving blood cells (3).

FD-OCT systems can be classified into two versions: Spectral-domain OCT (SD-OCT) and swept-source OCT (SS-OCT) (31). In SD-OCT, the optical frequency components are captured simultaneously using a dispersive element and a linear array detector (e.g., line scan camera). On the other hand, in SS-OCT, the optical frequency components are captured by a single detector (e.g., photodiode) in a time-encoded sequence achieved by sweeping the frequency of the laser source.

In this chapter, I provide a summary of the techniques utilized in this dissertation, including SS-OCT, SD-OCT, and the OMAG method.

1.3 Spectral domain optical coherence tomography

Spectral domain OCT employs a broad-spectrum light source and a spectrometer, as shown in Fig 1.1, illustrating its fundamental system configuration. With the aid of a spectrometer, the interference pattern, after recombination, is split into various wavelength components by a grating and subsequently detected by a line-scanning camera. The detected interferogram then undergoes Fourier transform, where the frequency corresponds to the depth and the amplitude corresponds to the reflectivity of the sample, generating an A-line. By utilizing a two-dimensional (2D) scanner, multiple A-lines can be obtained to form a B-scan, and by acquiring multiple B-scans, a three-dimensional (3D) volume can be achieved.

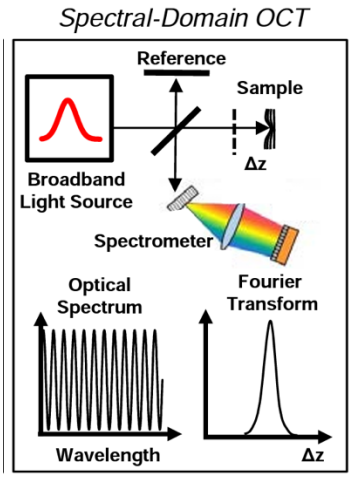

Fig 1.1 Schematic illustration of basic SD-OCT set up (32).

The primary limitations of a typical SD-OCT system include the range of optical measurements and the speed of the line-scan camera. According to the sampling theorem (33), the optical ranging distance is constrained by the number of detectors in the spectrometer (pixels on the line-scan camera), while the depth resolution is determined by the spectral bandwidth of the light source. Additionally, line-scan cameras operating with 1300nm light sources typically achieve speeds of approximately 100-200 kHz, which imposes restrictions on SD-OCT systems used in applications requiring rapid data acquisition. On a positive note, SD-OCT systems offer greater stability, easier maintenance, and cost-effectiveness when compared to SS-OCT systems.

1.4 Swept-source optical coherence tomography.

Unlike SD-OCT, SS-OCT employs a frequency scanning light source and a photodiode detector. In SD-OCT, the interferogram spectrum is spatially resolved using a grating, whereas in SS-OCT, the interferogram spectrum is obtained by sweeping different light wavelengths from the light source sequentially. Each swept wavelength corresponds to a different depth location in the sample after Fourier transform. With a slightly modified setup (shown in Fig 1.2), SS-OCT offers several advantages over SD-OCT, including reduced sensitivity loss along the depth, extended imaging range, and faster imaging speed (34).

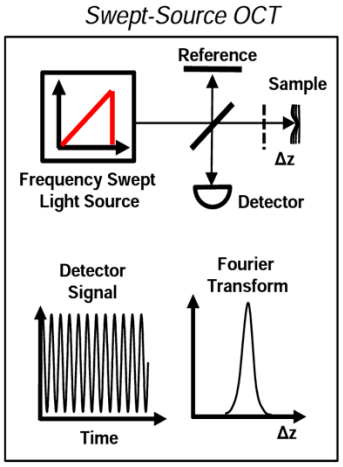

Fig 1.2 Schematic illustration of basic SS-OCT set up (32).

1.5 Optical Coherence tomography angiography

OCT angiography (OCTA) is a functional extension of OCT. When obtaining 3D data from a biological sample, signals are captured from both stationary and moving particles at a single time point. By acquiring multiple OCT scans at different time points, static tissue signals exhibit minimal variation, while signals from moving particles display significant variation in both amplitude and phase. OCTA distinguishes vessels from the surrounding static tissues by analyzing the differences in OCT signal variation over time. Over the past decade, various OCTA techniques have been developed, classified into different groups based on their utilization of 1) the phase component of the OCT signal, 2) the amplitude component of the signal, or 3) the entire complex OCT signal (35).

OCTA has gained significant popularity in both clinical ophthalmology and dermatology, regardless of the specific OCTA techniques employed. This growing preference for OCTA over traditional dye-based angiography can be attributed to several factors. Firstly, OCTA offers a faster and safer imaging method. Secondly, it is a 3D imaging technique that allows for the detailed visualization of vascular structures across different layers of tissues. Additionally, OCTA provides high lateral resolution, enabling the imaging of capillaries.

1.6 Scope of the thesis

This thesis focuses on the utilization of OCT in both ophthalmology and dermatology to advance clinical practice. In Chapter 2, we delve into novel algorithms and methods developed for OCT imaging. This thesis begins with a method to estimate the optical attenuation coefficient (OAC) from OCT images, enhancing

contrast and providing valuable tissue information. This research utilizes OAC to improve segmentation of various tissue structures, including epidermal thickness, retinal pigment epithelium (RPE), calcified drusen, and introduces TransUnet, a deep learning-based approach for precise outer retinal layer (ORL) segmentation. These advancements significantly enhance OCT imaging analysis in various applications. In Chapter3, the research aims to enhance the diagnosis and management of AMD by automating the identification of AMD biomarkers, specifically calcified drusen and the outer retinal layer. Additionally, it seeks to establish a baseline for healthy eye asymmetry. In Chapter4, the thesis addresses the critical need for a non-invasive tool to assess burn wound healing and skin autograft integration. The objectives encompass evaluating burn wound healing, monitoring skin autograft integration, and exploring the underlying mechanisms of wound healing. Ultimately, this research strives to significantly improve clinical outcomes in both fields through the innovative application of OCT technology.

2 Chapter 2: New algorithms and methods for OCT imaging

In this Chapter, we delve into novel algorithms and methods developed for OCT imaging. We begin with a straightforward yet highly effective approach for estimating the optical attenuation coefficient (OAC) from OCT images. OAC not only enhances OCT imaging contrast but also serves as a valuable physical parameter for assessing tissue characteristics, as alterations in tissue morphology and content can impact OAC. Building on this, we leverage the OAC to enhance OCT imaging contrast, leading to the development of algorithms for more precise and efficient segmentation of epidermal thickness, retinal pigment epithelium (RPE), and calcified drusen. Additionally, we introduce TransUnet, an innovative deep learning-based method developed for accurate segmentation of the outer retinal layer (ORL). Through this progressive exploration of OCT technology and advanced algorithms, our research significantly improves imaging segmentation and analysis in OCT applications.

2.1 OCT - derived optical attenuation coefficient (OAC)

2.1.1 Introduction

OCT light attenuates along its path due to light absorption and scattering (36); a characteristic that is unavoidable, but by measuring such attenuation, one can significantly increase the levels of image contrast in areas that would otherwise be difficult to distinguish. Such a parameter can be estimated from OCT data and has been applied to the study of ophthalmology, as well as skin and brain imaging, to facilitate structural segmentation and visualization (37,38). With the primary source of light scattering in the skin being

filamentous proteins, i.e. the structural element of the skin, and the principal filamentous protein of the dermis, i.e. collagen, being approximately 10 times larger than that of the epidermis, i.e. keratin (39,40), we believe the dermis may exhibit larger OAC measures compared to the epidermis. This detail, therefore, allows OAC to provide enhanced contrast of the DEJ and facilitate the accurate automatic segmentation of the epidermis.

Furthermore, in addition to OAC being used to improve imaging contrast, it can also serve as a physical parameter for evaluating tissue characteristics because changes in tissue morphology and content can alter a tissue's OAC. Previous works have shown promising results in the application of OAC to monitoring skin wound healing, assessing burn scars, identifying brain cancer, and evaluating brain damage. Although each study above has been successful in clarifying exciting findings regarding changes of tissue properties, each is not without its particular disadvantages. For example, those skin-related studies have not segmented the DEJ to distinguish the dermal layer, which might cause the epidermis and dermis to be considered one when calculating OAC. As mentioned above, epidermal and dermal layers exhibit different OAC properties; therefore, it is critical to measure such layers separately. Moreover, the authors are unaware of any research currently using OCT to explore the OAC changes in human skin from acute burns at different time points post-injury.

2.1.2 Method

2.1.2.1 Clinical Proposal

The use of OCT was approved by the University of Washington institutional review board (IRB). Our study included eight participants, all over 18 years of age, with burns constituting > 1% total body surface area (TBSA). All participants voluntarily gave written informed consent, and then underwent OCT scanning at two time points (referred to as imaging sessions), one within 2 – 7 days of being injured and the other within 15 – 21 days of being injured. The interval between both imaging sessions was approximately 2 weeks. For each participant, several burn sites, 2 – 4, were scanned based on the assessment of the attending surgeon. For comparative purposes, each participant also had scans taken of adjacent or contralateral normal skin.

2.1.2.2 OCT Imaging

OCT scanning was performed using an in-house-built swept-source OCT (SS-OCT) system with a central wavelength of 1310 nm, and a bandwidth of 100 nm. More detailed system information is available in our

previous publications (34). The handheld probe was specifically designed with a sample spacer to keep the skin at a fixed distance from the objective lens.

A drop of sterile glycerin was applied to the skin surface immediately prior to OCT scanning to act as a refractive index matching medium; thereby, reducing hyper-reflective artifacts and increasing imaging depth. Each OCT scan covered a region of ~ 9 × 9 × 1.5 mm (~ 800 × 800 × 200 pixels) in the x (fast axis), y (slow axis) and z (penetration into the skin) directions, respectively, with a lateral resolution of ~ 11 μm (9 mm / 800) and an axial resolution of ~ 7 μm. For each 3D scan, the acquisition time was approximately 30 seconds.

2.1.2.3 Optical Attenuation Coefficient (OAC) Estimation

The OAC of a specific biological tissue is related to the OCT signal intensity that is back-scattered from the sample, with the OCT signal intensity being affected by the focus location. Therefore, the confocal function of the OCT system should be taken into account when quantifying OAC. Faber *et al*. (41) proposed the following depth-wise model:

$$I(z) \propto h(z)e^{-2\mu z},$$

Where μ is the OAC and z is the OCT signal depth. The $h(z)$ is the confocal function and can be expressed as:

$$h(z) = \left(\left(\frac{z-z_0}{z_R}\right)^2+1\right)^{-1},$$

Where z_0 is the focal plane depth, and z_R is the apparent Rayleigh range expressed as:

$$z_R = \alpha n z_r \ ,$$

Where α equals 2 for diffuse reflectors, n is the refractive index (we used n = 1.37 in this study (39)), and z_r is the Raleigh range of the Gaussian beam. In our OCT system, an objective lens (LSM03, ThorLabs) with a z_R of ~ 133.0 μm was installed. The confocal function for the OCT intensity could be removed by dividing the OCT intensity by function $h(z)$.

Whilst sensitivity roll-off is another factor that affects OCT signal intensity, our previous publication demonstrated that the sensitivity of this SS-OCT system was almost unchanged and was maintained at > 100 dB within the depth range of 8 mm (11). The imaging depth used here did not exceed 2 mm; therefore, the effect of sensitivity roll-off was not considered here during OAC estimation.

To estimate OAC, several models have been proposed to describe the OCT signal, including single-scattering model, multiple-scattering model, and full electromagnetic wave model. Among them, the single-scattering model is the most common model. In this study, we used the depth-resolved method for quantifying OAC, one of the methods based on the single-scattering method (36):

$$\mu(z) \approx \frac{I(z)}{2\Delta \sum_{z+1}^{N} I(z)},$$

Where $I(z)$ indicates the OCT signal intensity and $\mu(z)$ represents the OAC at *z-th* pixel along the depth. Δ is the pixel size, approximately 7 μm in this study, and N is the last pixel of each A-line. Here, it is assumed that most of the light had already been completely attenuated at the N-*th* pixel.

2.1.2.4 OAC Estimation of Acute Burn Skin

Here, a mean intensity projection (MIP) image with a depth of ~ 140 μm was taken from immediately below the DEJ to avoid the effects of the epidermis and noise floor. These MIP images were generated by mapping the average OAC value at each A-line on to a 2D map, termed an *en face* map. The *en face* maps were then color coded to show OAC value ranging from 0 – 6 mm^{-1}.

2.1.3 Result

Shown in Fig 2.1 are the OAC maps. Fig 2.1 A, D, and G show the OAC maps of normal skin from patient #1, patient #2, and patient #3, respectively. OAC estimations vary between participants, but each participant's map shows homogenously distributed variations in OAC. Both phenomena are to be expected. Comparatively, however, the maps derived from both imaging session following injury depict alterations in OAC value distributions with each participant, and an overall decrease in OAC values (as seen by the increase in blue coloration). Following injury, Patient #1 initially showed a sharp decrease in OAC value in imaging session #1 (Fig 2.1 B), which then appeared to be rising in imaging session #2 (Fig 2.1 C). Comparatively, both patients #2 and #3 did not suffer a similar decrease in OAC value in imaging session

#1 (Fig 2.1 E and H, respectively), but did appear to have lower OAC values in imaging session #2 (Fig 2.1 F and I, respectively).

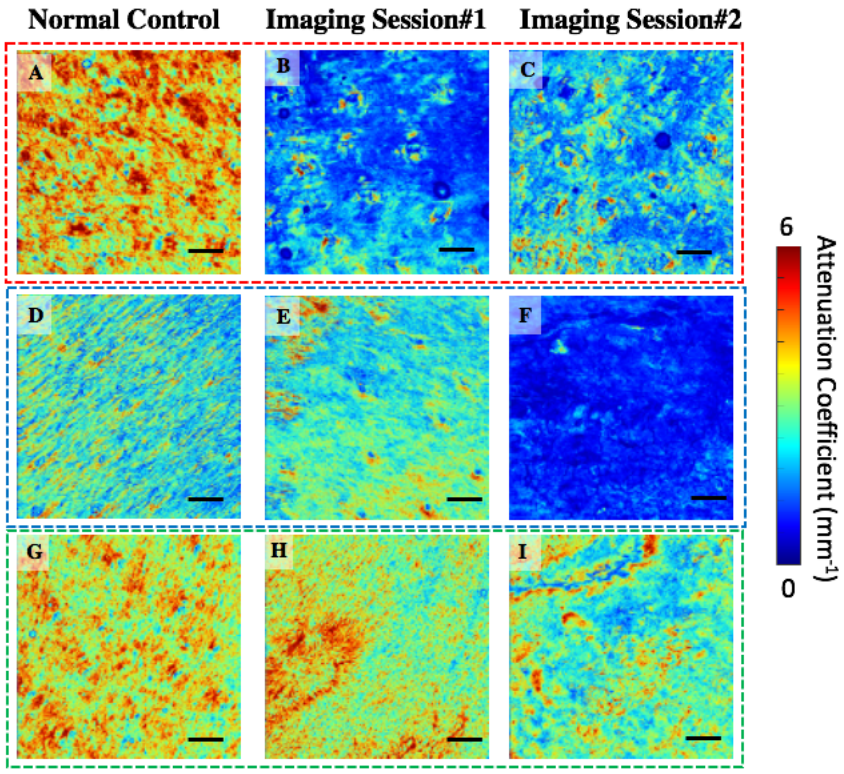

Fig 2.1 En face projected OAC maps obtained from the dermis layer.
(**A, B, C**) patient #1, (**D, E, F**) patient #2, and (**G, H, I**) patient #3. All en face images are mean intensity projected representing the depth of approximately 140 μm. Color bar represents OAC value. Scale bar represents 1 mm. OAC, optical attenuation coefficient.

Shown in Fig 2.6 are the averaged OAC measurements representing all eight study participants with 28 burn sites over two imaging sessions. To reduce the bias caused by individual differences, we presented the ratio of the averaged OAC between the burn site and the healthy site (referred as normalized OAC). Overall, the OAC measurements in imaging session #2 were significantly lower than those of imaging session #1. Moreover, the 95% confidence interval (CI) of the normalized OAC from the burn sites in imaging session #1 and imaging session #2 was 0.7593 to 0.9295 and 0.6279 to 0.7881, respectively. Thus, the OAC of the burn sites during the two imaging sessions appeared to be smaller than comparable measures of the normal skin.

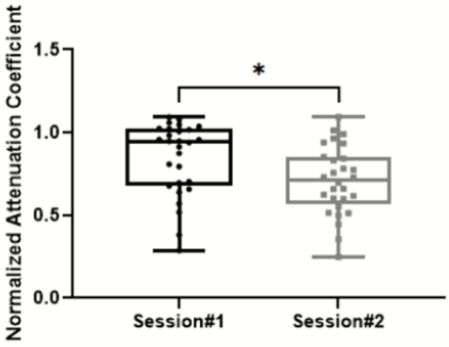

Fig 2.2 Comparison of normalized OAC between imaging session #1 and imaging session #2.
Boxplots show interquartile range, whiskers minimum to maximum. OAC, optical attenuation coefficient. *P ≤ 0.05.

2.1.4 Discussion and conclusion

Acute burn-damaged skin undergoes significant changes in content and structure during the wound healing process (42), which can be reflected in the OAC of the tissue. These significant changes can be arranged temporally and associated with four distinct yet overlapping stages of healing, i.e., hemostasis, inflammation, proliferation and maturation (43). In concordance with our imaging timeline and the numerous features we observed, most of our study participants were experiencing the inflammatory stage in imaging session #1, and the proliferation stage in imaging session #2. It is our deduction that the reduced back-scattered light resulting in a reduction in OAC in imaging session #1 was being caused by an excess of fluid, a typical feature of inflammation and injured blood vessels, or severe collagen damage, a typical feature of burn-damaged skin (42). The reduction in OAC values observed both qualitatively and quantitatively in imaging session #2 (Fig 2.1 and 2.2, respectively) is thought to be caused by the newly generated tissue whose optical properties differ from those of normal tissue before injury. In all, the OAC mapping derived from our OCT data has the potential to both aid in our understanding of the pathological changes known to occur in human skin following acute burn injury and serve as an indicator of tissue injury.

2.2 Epidermal thickness segmentation using OAC

2.2.1 Introduction

When researching novel techniques for burn assessment, an increasing level of attention is being paid to optical coherence tomography (OCT) because of its cellular level resolution, non-invasive nature, and real-time, three-dimensional (3D) imaging capabilities (2). With a remarkable capacity for extension, OCT is being applied in numerous forms to a wide variety of scenarios to acquire data from multiple angles and

sources. Lindert *et al*. (44), for example, utilized OCT to identify specific imaging patterns related to burn depth, including a loss of the epidermal and papillary dermal thickness, and an altered surface roughness. Kim *et al*. (45), too, utilized another form of OCT, polarization-sensitive OCT (PS-OCT), to investigate the birefringence of burned skin, highlighting a smaller birefringence in burned skin compared to that of healthy skin. Another promising form of OCT is OCT-based angiography (OCTA), which is a functional extension of OCT that can provide vascular information without the need for invasive contrast agents. A number of studies have demonstrated the potential of OCTA to both qualitatively and quantitatively assess the vascular response to burn injury over time. Despite the increased applicability of OCT in its various forms, however, studies regarding the visualization and subsequent measuring of epidermal thickness in skin post-injury are limited. Epidermal thickness is a critically important parameter to evaluate re-epithelialization during the burn wound recovery (46) and other dermatologic conditions.

2.2.2 Method

Clinical proposal and OCT imaging were the same as section 2.1.2.

The epidermal layer was segmented from the skin surface to the dermal epidermal junction (DEJ) using a set of algorithms shown in Fig 2.3. The first step in our algorithms involved the detection of the skin surface (Fig 2.3 B and C). Briefly, a Gaussian filter was applied to reduce speckle noise on each OCT B-frame. Then, a gradient function was used to obtain the rate of OCT intensity change at each A-line. Finally, the skin surface was detected by finding the maximum gradients at each A-line. The second step aimed to improve DEJ contrast by estimating OAC, as described in section 2.1.2.3 (Fig 2.3 D). The third step was DEJ detection (Fig 2.3 E and F), but unlike the surface detection, the DEJ was detected within a defined region instead of the entire A-line. The upper boundary was the estimated skin surface and the lower boundary was 50 pixels (~ 350 μm, as the average epidermal thickness is about 150 μm) below the skin surface. We then identified the first gradient value within a specific range (based on the imaging intensity range) within the defined region to highlight the DEJ. After automatic segmentation was complete, we manually checked for accuracy. The last step measured the distance between the skin surface and DEJ. Fig 2.3 G shows the resulting epidermal thickness map, where a color-code was applied to represent a thickness range of 0 – 350 μm.

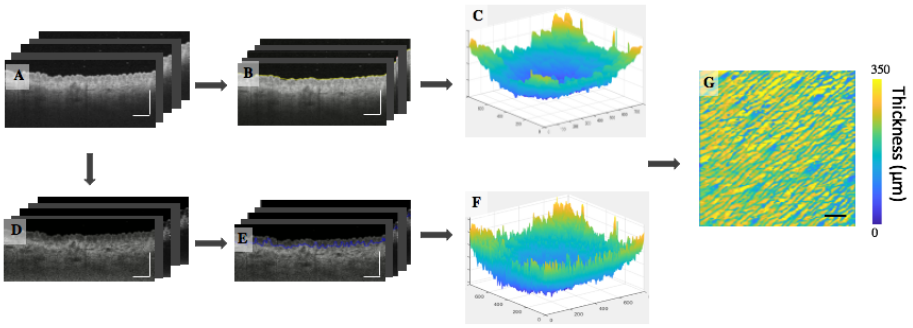

Fig 2.3 A schematic of epidermal segmentation.
(**A**) Unaltered OCT B-frames. (**B**) The same B-frame shown in (A) with the skin surface highlighted. (**C**) A 3D visualization of the skin surface highlighted in (B). (**D**) OAC B-frame derived from the B-frame depicted in (A). OAC B-frame highlighting the position of the DEJ. (**F**) A 3D visualization of the DEJ highlighted in (**E**). (**G**) Epidermal thickness map derived from OCT and OAC B-frames. Color bar represents a depth of range of 0–350 μm. Scale bar represents 1 mm. 3D, three-dimensional; DEJ, dermal–epidermal junction; OAC, optical attenuation coefficient; OCT, optical coherence tomography.

2.2.3 Result

Shown in Fig 2. 4 are comparisons between the segmentation results derived from both OCT and OAC data. OCT B-frames provided a significantly higher contrast at the skin surface for surface location efforts, but OAC B-frames provided a significantly higher contrast at the DEJ for a more easily detectable DEJ (Fig 2.4 A, B, D, E and G). When combined, the accuracy of automatic DEJ segmentation was made significantly more accurate. Fig 2.4 A and B show two representative OCT B-frames, highlighting how a low DEJ contrast would make epidermal segmentation inaccurate. Fig 2.4 D and E show the corresponding B-frames, only this time with OAC applied, highlighting how an improved DEJ contrast would help epidermal segmentation. Furthermore, as shown in Fig 2.4 H, without manual segmentation correction, epidermal thicknesses obtained from OCT B-frames alone would provide significantly higher thickness measurements than those obtained from OAC B-frames.

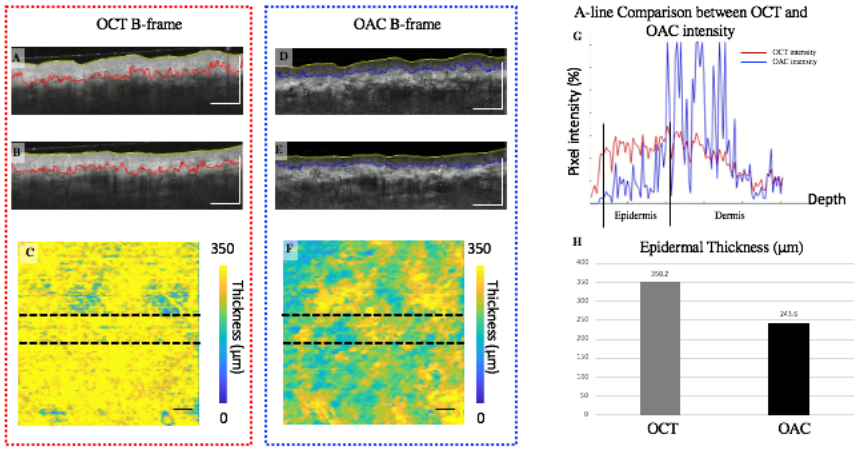

Fig 2.4 Demonstration of OCT- and OAC-derived epidermal thickness maps. OAC maps enhancing DEJ contrast and the accuracy of automatic segmentation of the epidermis.
(**A** and **B**) Unaltered OCT B-frames corresponding to the black dash line in (**C**). Supposed DEJ highlighted by red lines. (**D** and **E**) OAC B-frames corresponding to the black dash line in (**F**). DEJ highlighted by blue lines. (C) Epidermal thickness map derived from segmentation results shown in A and B. (F) Epidermal thickness derived from segmentation results shown in D and E. (**G**) A single A-line comparison between OCT and OAC intensity (shown in percentage difference from mean). (**H**) The comparison of epidermal thickness measurements between using OCT maps and OAC maps. Whiskers represent standard deviation. DEJ, dermal–epidermal junction; OAC, optical attenuation coefficient; OCT, optical coherence tomography.

Fig 2.5 shows epidermal thickness maps derived from three representative participants (here referred to as patient #1, patient #2, and patient #3). Generally, Fig 2.5 shows that whilst the epidermal thicknesses of the normal sites may differ between patients (an expected occurrence, especially when one takes into account that the healthy sites are at different locations on the body), the maps appear homogenous in terms of thickness distribution and overall topography (Fig 2.5 A, F, I, N, Q and V). In contrast, the epidermal thicknesses from the burn sites of each participant are more heterogenous and varies dramatically between the participants, whilst also having no discernable texture or homogenous topography (Fig 2.5 C, G, K, O, S and W, and Fig 2.5 E, H, M, P, U and X). More specifically, Fig 2.5 B, J and R show the burn-damaged sites at 6-, 6- and 5-days post-injury, respectively, with approximate scan locations highlighted. Fig 2.5 C, K and S are the epidermal thickness maps corresponding to Fig 2.5 B, J and R. Fig 2.5 D, L and T show the burn-damaged sites at 20-, 20- and 19-days post-injury, respectively, with approximate scan locations highlighted. Fig 2.5 E, M and U are the epidermal thickness maps corresponding to Fig 2.5 D, L and T. Following injury, patient #1 demonstrated a significantly increased epidermal thickness in imaging session #1 (Fig 2.5 C) compared to that of the normal site (Fig 2.5 A), which then began to thin and normalize in imaging session #2 (Fig 2.5 E), although it was still not as thick as the healthy site. Following injury, patient #2 demonstrated a significantly decreased epidermal thickness in imaging session #1 (Fig

2.5 K) compared to that of the normal site (Fig 2.5 I), which then thickened in imaging session #2 (Fig 2.5 M) to the point it was then thicker than the normal site. Similarly, following injury, patient #3 demonstrated similar changes in epidermal thickness to that of patient #2 (Fig 2.5 Q and S), although the epidermal thickness did not recover to the point of being thicker than the normal site in imaging session #2 (Fig 2.5 U).

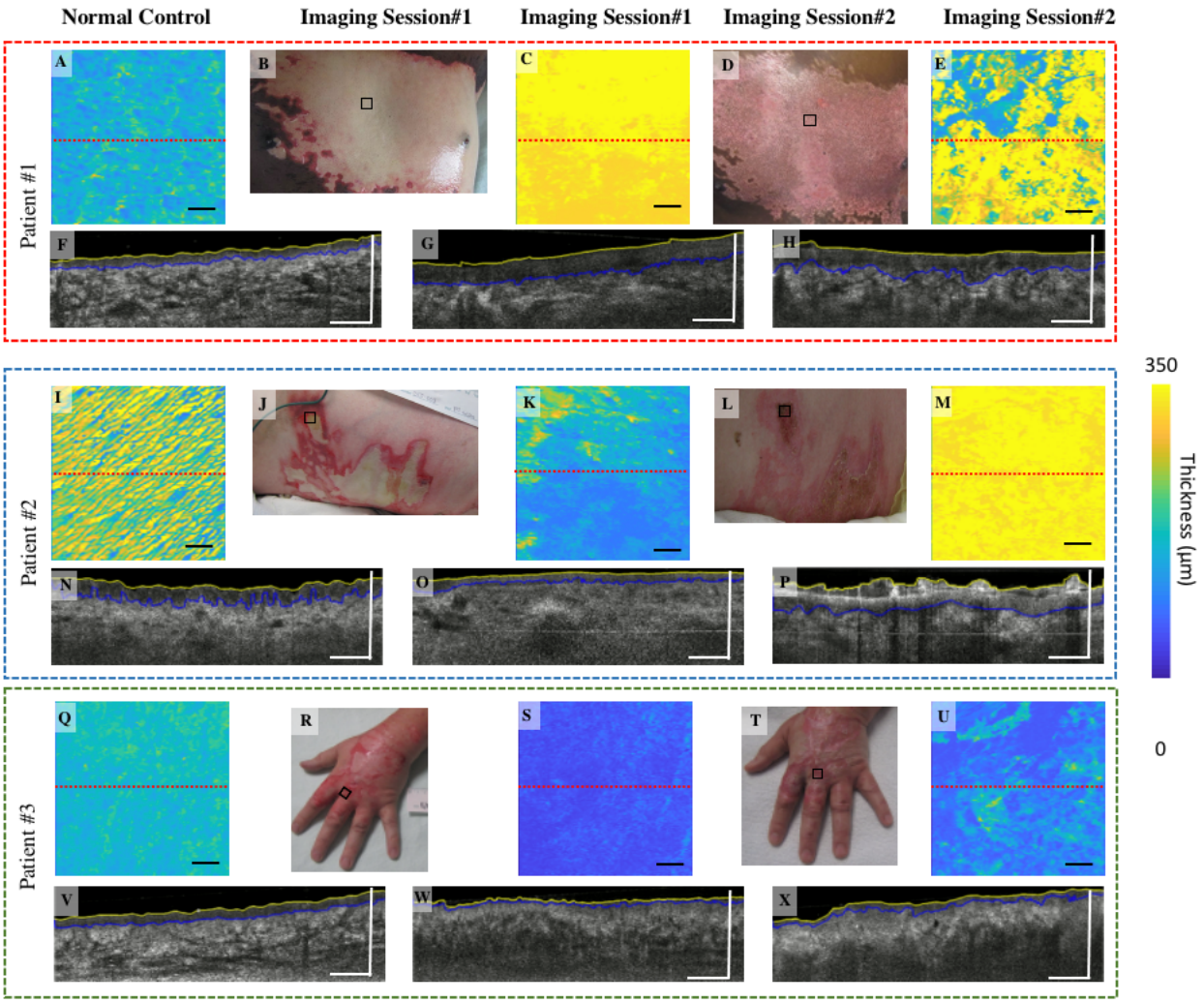

Fig 2.5 The epidermal thickness maps of three representative burn cases (referred to as patient #1, patient #2, patient #3) spanning two imaging sessions.
(**A**, **I**, and **Q**) Epidermal thickness maps of the healthy skin. (**F**, **N**, and **V**) Cross-sectional OCT B-frames corresponding to the locations highlighted with perforated red lines in A, I, and Q, respectively. (**B**, **J**, and **R**) Photographs of the burned sites in imaging session #1 with approximate scan locations highlighted. (**C**, **K**, and **S**) Epidermal thickness map of the burned sites in imaging session #1. (**G**, **O**, and **W**) Cross-sectional OCT B-frames corresponding to the locations highlighted with perforated red lines in C, K, and S respectively. (**D**, **L**, and **T**) Photographs of the burned sites in imaging session #2 with approximate scan locations highlighted. (**E**, **M**, and **U**) Epidermal thickness map of the burned sites in imaging session #2. (**H**, **P**, and **X**) Cross-sectional OCT B-frames corresponding to the locations highlighted with perforated red lines in E, M, and U, respectively. Yellow lines highlight

the skin surface. Blue lines highlight the dermal-epidermal junction. Color bar represents a depth of range of 0–350 μm. Scale bar represents 1 mm. OAC, optical attenuation coefficient; OCT, optical coherence tomography

Shown in Fig 2.6 are the averaged epidermal thickness measurements representing all eight study participants with 28 burn sites over two imaging sessions. To reduce the bias caused by individual differences, we presented the ratio of the averaged epidermal thickness between the burn site and the healthy site (referred as normalized epidermal thickness). Despite individual variances, we did not observe any significant difference in normalized epidermal thickness between both imaging sessions.

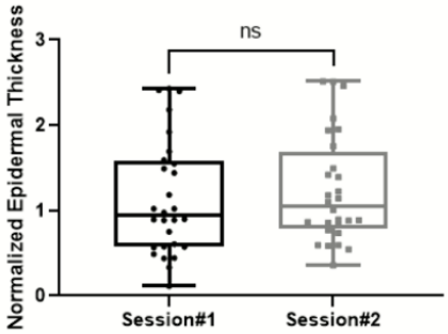

Fig 2.6 Comparison of normalized epidermal thickness between imaging session #1 and imaging session #2.
ns: not statistically significant. Boxplots show interquartile range, whiskers minimum to maximum.

2.2.4 Discussion and conclusion

Qualitative and quantitative assessments of the epidermis of burned skin are important factors required for accurately evaluating the healing process. In this study, we have demonstrated the ability of OCT-derived OAC to assist in the automated assessment of the epidermis (Fig 2.5), which is an advancement from previous studies that performed epidermal segmentation from OCT intensity information(47–51). Our automated protocols also have the potential to augment assessment accuracy and efficiency with OAC maps, whilst also increasing applicability, as OAC has been shown to be a critical physical parameter for evaluating tissue characteristics (52).

Qualitatively, we demonstrated using automatically-generated maps that epidermal thickness differs in burn-damaged skin compared to that of healthy normal skin (Fig 2.5). Whilst it is not the intention to provide any form of clinical diagnosis in this study, many factors are known to cause abnormal epidermal thickness in the burned skin, including a loss of partial skin, edema, scab generation, epidermal regeneration, and so on (53). Combined, these medical traits might explain why it was difficult to find uniform

characteristics of the epidermal thickness among different individuals (Fig 2.5 and 2.6). Changes in epidermal thickness could be an important biomarker used in monitoring the burn wound healing process, as such a feature is not typically easily distinguishable through normal clinical evaluation methods. Our segmentation method, with the assistance of OAC, could provide greatly improved epidermal information to help clinicians or surgeons closely monitor burn wounds as they heal.

To conclude, our study has demonstrated that OCT-derived OAC can be used to enhance imaging contrast and facilitate the automated segmentation and quantification of the epidermal layer, as well as help to aid in our understanding of the pathological changes that occur in human skin following acute burn injury, which could serve in future as an objective indicator of tissue injury and subsequent repair.

2.3 Calcified drusen segmentation using OAC

2.3.1 Introduction

Age-related macular degeneration (AMD) is a leading cause of irreversible vision among the elderly worldwide (6). Drusen are the hallmark feature of early and intermediate AMD and are characterized by accumulations of extracellular material that build up in the space between Bruch's membrane (BM) and the elevated retinal pigment epithelium (RPE) (13,15). The progression and pathogenesis of AMD have not been fully understood, but the calcification of drusen is considered an indicator of increased risk of late AMD (13,15). Therefore, identifying and quantifying calcified drusen would be of great clinical importance in the evaluation and monitoring of AMD progression and for the understanding of the pathological basis of calcified drusen.

OCT is a well-established imaging modality that has been widely utilized in ophthalmology for retinal disease diagnosis and treatment management because of its ability to provide non-invasive, depth-resolved, high-resolution information (4). On OCT B-scans, drusen appear as localized elevations and disruptions of the structure of RPE (54), while calcified drusen can be identified from heterogeneous internal reflectivity within drusen (HIRD) (14,55). Liu et al. (56) reported that calcified drusen appear as dark foci on en face subRPE SS-OCT images obtained from a slab defined by boundaries from 64 to 400 μm under BM. These dark foci appear due to the hypotransmission of light into the choroid and are named choroidal hypotransmission defects (hypoTDs). Compared with OCT B-scans, the en face image provides the reviewers and graders an overview of the entire scanned region at a single glance.

Using a similar subRPE en face OCT imaging strategy, our group successfully identified and quantified geographic atrophy (GA) by developing an automated algorithm to detect choroidal hypertransmission defects (hyperTDs) (57). Rather than detecting hyperTDs, we used a similar strategy to detect choroidal

hypoTDs to identify and quantify calcified drusen (56). However, hypoTDs can also result from other anatomic features in the scan other than calcified drusen, such as hyperreflective foci, a thickened RPE layer, vitelliform material, and large retinal pigment epithelial detachments (58), which complicates the grading of calcified drusen from subRPE slabs. Currently, in clinical practice, clinicians and researchers identify the various causes of hypoTDs on subRPE slabs by manually checking the corresponding B-scans. As a result, the task of identifying and quantifying calcified drusen by manual segmentation on subRPE images is labor-intensive, particularly when the corresponding B-scans need to be checked for each hypoTD, and this task is subject to grader variability. Thus, there remains a clinical need for an automated algorithm capable of identifying and quantifying calcified drusen.

Several automated algorithms have been developed and tested to automatically segment retinal anatomic features on OCT images or fundus images, including traditional computer vision (59–61) and machine/deep learning approaches (62–68). However, the identification of calcified drusen presents some unique challenges, especially since the characteristic features of these drusen on 2D en face images sometimes overlap with other causes of hypoTDs. In this study, we propose a simple yet efficient strategy to automatically identify, segment, and quantify calcified drusen on OCT imaging.

2.3.2 Method

2.3.2.1 Participants and Imaging acquisition

Patients were enrolled in a prospective SS-OCT imaging study at the Bascom Palmer Eye institute. This study was approved by the institutional review board (IRB) of the University of Miami, Miller School of Medicine and was performed in accordance with the tenets of the Declaration of Helsinki (as revised in 2013) and complied with the Health Insurance Portability and Accountability Act of 1996. All participants provided written informed consent before imaging. OCT scanning was carried out using a 6×6 mm^2 macular swept-source OCT angiography (SS-OCTA) scanning protocol (PLEX® Elite 9000, Carl Zeiss Meditec, Dublin, CA, USA). This instrument was equipped with a 100 kHz swept laser source with a central wavelength of 1050 nm and a spectral bandwidth of 100 nm, providing an axial resolution of ~5.5 μm and a lateral resolution of ~20 μm estimated at the retinal surface. The 6 × 6 mm^2 scans consisted of 1536 pixels on each A-line (3 mm), 500 A-lines on each B-scan, and 2 repeated B-scans at each B-scan position. OCT scans were excluded from the study if signal strength was less than 7 or evident motion artifacts were observed. After being retrospectively reviewed, the eyes were included in this study only when the B-scans were present with drusen that contained hyperreflective contents with a hyperreflective cap and a hypo-reflective core (Figs. 2.7 A-C) or without a hypo-reflective core (Figs. 2.7 D-F) accompanied by choroidal hypoTDs.

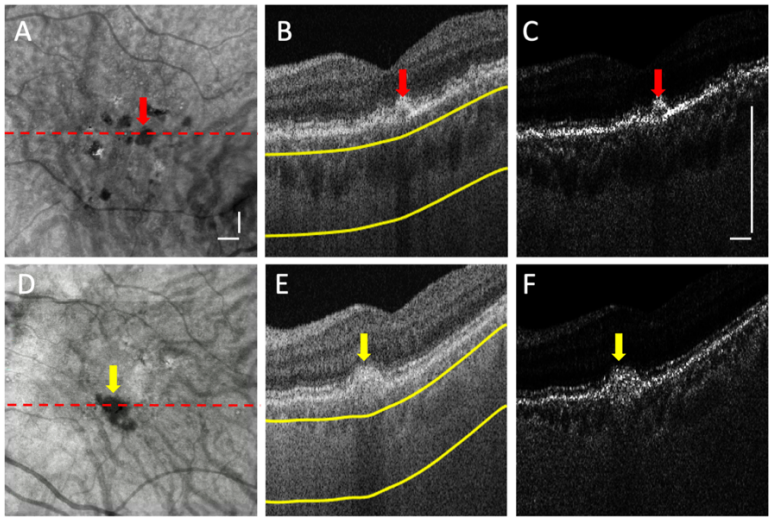

Fig 2.7. Examples of calcified drusen
on the representative OCT scans from (A-C) an eye with calcified drusen with a hyperreflective cap and a hypo-reflective core (Red arrow), and (D-F) an eye with calcified drusen with hyperreflective contents but without a hypo-reflective core (Yellow arrow). (A, D) enface subRPE OCT image obtained from a slab defined by 64μm to 400μm below the Bruch's membrane (BM) shown as yellow lines in (B, E), where hypoTDs appear as the dark foci. (B, E), Representative B-scans passing through calcified drusen at the locations highlighted by dashed lines in (A, D), and (C, F) correspondingly converted OAC B-scans, respectively. Scale bar represents 500 µm.

2.3.2.2 OAC estimation from OCT volumes

That the OCT signals in the scan dataset were converted to the corresponding optical attenuation coefficient (OAC) at each pixel has been described in 2.1.2.3.

2.3.2.3 Considerations when segmenting RPE

As mentioned above, drusen are characterized by a localized elevation of the RPE on OCT B-scans, and calcified drusen are a subset of drusen in which the accumulated extracellular material possesses higher scattering property (i.e., higher OAC values) when compared with the soft drusen. Therefore, it is important to first identify and segment drusen, for which an accurate segmentation of both RPE and BM is critical. While BM segmentation has proved robust using the manufacture automated segmentation algorithm (which is adopted in this study), the RPE segmentation is a more challenging task. An incorrect segmentation of RPE would lead to difficulty in the identification of the calcified drusen.

Typically, the distance between the RPE and BM at each A-line is utilized to construct a 2D drusen map and to visualize and quantify the drusen. In a previous study, the RPE was located by finding the position of the pixel along each A-line with the largest OAC value above the BM. While this strategy has been successfully used to segment the RPE in many studies, it can run into problems when there are structures with higher OAC values than that of RPE located above the BM (Fig. 2.8), such as hyperreflective foci (e.g.

migrated pigment, Figs. 2.8 A-C) and calcified drusen (Fig. 2.8 E-G). A possible approach to mitigate this complication is to use a median filter and a local regression with weighted linear least squares and a 2nd-degree polynomial model to physically smooth and correct the inaccurate RPE segmentation(69). Such mitigation works to correct the inaccurate RPE segmentation caused by the hyperreflective foci (Fig. 2.8 D), but unfortunately does not work well for the cases with calcified drusen where the corrected RPE appears lower than the actual RPE positions (Fig. 2.8 H). For this reason, we further modified the RPE segmentation algorithm by introducing a RPE location correction, Zc, defined as:

$$Z_c = \frac{1}{2}(\Delta_{FWHM} - \Delta_{RPE}) \qquad (2)$$

where $\Delta_{FWHM}$is the full-width-half-maximum (FWHM) width defined by the OAC peak alone the A-line, and Δ_{RPE} is the RPE width. This means that the RPE location is modified by moving the prior location up by an amount of Zc. Zhou et al found that with SS-OCT imaging, $\Delta_{RPE}$is approximately between 25 and 30 μm (70). In this study, we used a constant $\Delta_{RPE}= 25\mu m,$ which is consistent with the measurements for older subjects (70). This approach works because the calcified drusen is a highly scattering mass that would make the FWHM appear wider than that at the soft drusen (see Fig.2.9, Fig. 2.9 D vs Fig. 2.9 E).

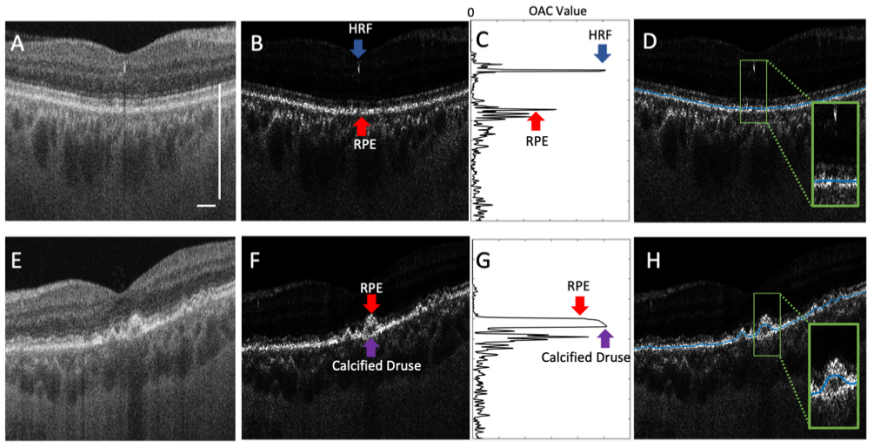

Fig 2.8 Effects of hyper reflective foci (HRF) and calcified drusen on retinal pigment epithelium (RPE) segmentation.
(A) OCT B-scan and (B) corresponding optical attenuation coefficient (OAC) B-scan with a HRF (blue arrow). (C) A single OAC A-line through HRF with two peaks highlighted, due to HRF (blue arrow) and RPE (red arrow), respectively, which would make the direct OAC segmentation of RPE erroneous. (D) OAC B-scan with the RPE segmentation (blue line) after filtering and smoothing. (E) OCT B-scan and (F) corresponding OAC B-scan with a calcified druse (purple arrow). (G) A single OAC A-line through the calcified druse where the difficulty to segment the RPE appears apparent. (H) OAC B-scan with the erroneous RPE segmentation (blue line) at the calcified druse. Scale bar represents 500 µm.

Figure 2.9 shows such an example where at the locations of calcified drusen, the corrected RPE segmentation (yellow line) appears to match well with the actual RPE position (Fig. 2.9 C and 2.9 F) while the manufacture's segmentation method (blue line) and the direct OAC with filtering method (red line) appear to be less accurate. In regions where the RPE is normal or where soft drusen are present (Fig. 2.9 C), the new RPE segmentation does not deviate significantly from the prior strategies because the FWHM

values are sufficiently close to the normal RPE width. Figs. 2.9 G-I show drusen maps from the manufacturer's method (Fig. 2.9 G), the prior OAC method (Fig. 2.9 H) and the new strategy (Fig. 2.9 I), respectively, illustrating this new RPE segmentation provides more accurate drusen volume quantification, particularly in the areas with calcified drusen (pointed by the red and white arrows in Fig. 2.9 C, F, and I).

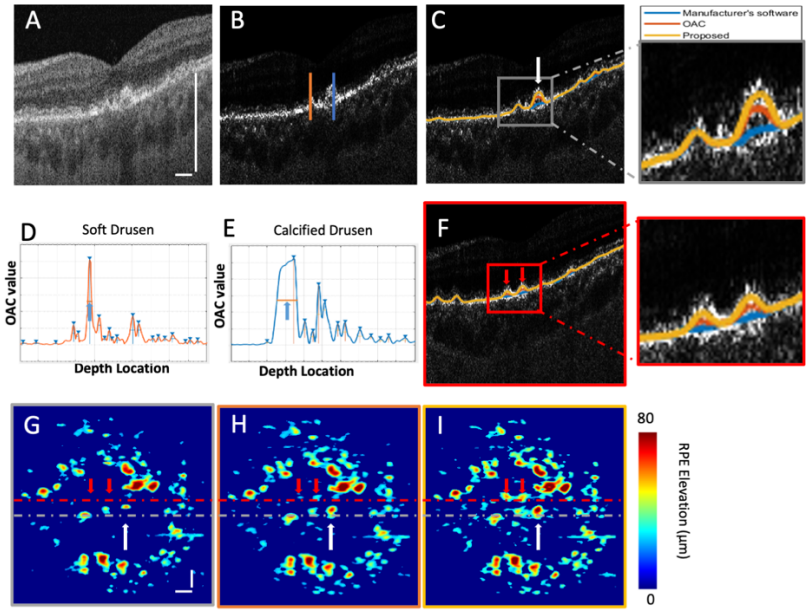

Fig 2.9 The comparison of the retinal pigment epithelium (RPE) segmentation performances on the soft drusen and calcified drusen among the manufacturer's approach, OAC method and proposed method.
(A) OCT B-scan and (B) corresponding optical attenuation coefficient (OAC) B-scan with soft drusen and calcified drusen with its location highlighted by gray dashed lines in G-I. (C) The same OAC B-scan as in (B) overlaid with the segmented RPE lines obtained by the manufacture software (blue line), OAC method (red line) and the proposed method (yellow line), respectively. (D) A single OAC A-line through the soft druse at the orange line position in (B), where the FWHM at the RPE peak is seen narrow (blue arrow). (E) A single OAC A-line through the calcified druse at the blue line location marked in (B), where the FWHM peak is seen wide (blue arrow) that was used to correct the RPE segmentation lines. (F). Another example OAC B-scan with calcified drusen with its locations marked by dashed red lines in (G-I) overlaid with the segmented RPE lines obtained by the manufacture approach (blue line), OAC method (red line) and proposed method (yellow line), respectively. (G-I) the drusen maps generated from 3D scans by displaying the distances between the Bruch's membrane (BM) and the RPE segmented by (G) the manufacture approach, (H) the OAC method and (I) the proposed method, respectively. Note that the distance information is coded with color shown in the color bar where the dynamic range was made purposely tighter to show the differences between different methods. White and red arrows indicate the regions of calcified drusen where the RPE segmentations are more accurate by the proposed method but underestimated by either the manufacture or OAC methods. Scale bar represents 500 μm.

2.3.2.4 Automated segmentation of calcified drusen

The next step is to segment the calcified drusen from the drusen. Because calcified drusen contain heterogeneous high scattering material that produce higher OAC values than the soft drusen (Fig. 2.7), the calcified drusen from the drusen can be isolated by mapping the OAC values within the space between (but excluding) RPE and BM. In order to minimize the possibility of false positive identifications due to small deviations in the segmentations (see below), we used the hypoTDs information to constrain the mapping of calcified drusen.

The workflow schematic of the algorithm is shown in Fig. 2.10. Two parallel steps, each generating a binary map (Fig. 2.10 F and 2.10 I, respectively) from a 3D SS-OCT scan, are combined to produce a final binary map (Fig. 2.10 J) to represent the regions occupied by the calcified drusen.

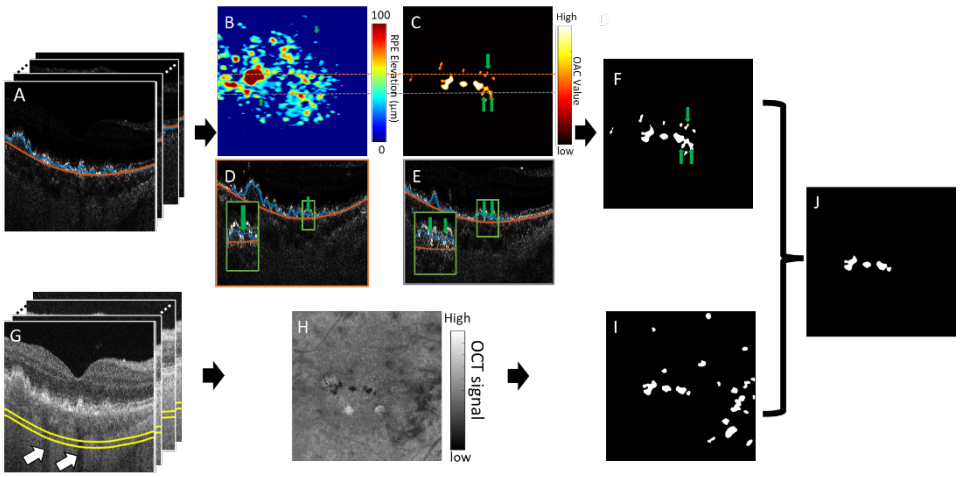

Fig 2.10 Schematic of the workflow for the proposed automated segmentation of calcified drusen from a SS-OCT volume scan. (A) Optical attenuation coefficient (OAC) B-scans with the segmentation lines of six pixels below retinal pigment epithelium (RPE, the blue line) to two pixels above Bruch's membrane (BM, the orange line) highlighted. (B) the drusen maps resulted from displaying the distances between the Bruch's membrane (BM) and the retinal pigment epithelium (RPE). (C) en face maximum mean projection OAC image of the slab defined by the two lines shown in (A). (D-E) Representative OAC B-scans with its locations marked by dashed red lines in (B and C) overlaid with the segmentation lines of six pixels below RPE (the blue line) to two pixels above BM (the orange line), showing small deviations in the RPE segmentations leading to false positive detection of calcified drusen (the green arrow). (F) The first binary mask derived from (C). (G) OCT B-scans with the segmentation lines (the yellow lines) located within the sclera region to define the slab thickness of 40μm, where the first line is determined by shifting the BM segmentation line by the maximum choroidal thickness in the volume. (H) en face sub-choroid OCT image of the slab defined the two lines shown in (G). (F) the second binary mask derived from (H). (J) Final binary mask resulted from the product between (F) and (I) to indicate the regions of calcified drusen.

The first step is to obtain a binary map indicating the regions where heterogeneous scattering material may possibly be present between the RPE and BM. A drusen map (Fig. 2.10 B) was first generated from the scanned OCT volume (Fig. 2.10 A) using the corrected RPE segmentation discussed in the last section. Note that the drusen volume can be easily calculated from the drusen map shown in Fig.4B. From this drusen map, an en face OAC images (Fig. 2.10 C) was then obtained from a slab taken from six pixels (~12 μm) below RPE segmentation line to two pixels (~4 μm) above the BM segmentation line (shown in blue and orange lines in Fig. 2.10 A) using the mean of the first six maximum OAC values at each A-line. A binary image (Fig. 2.10 F) is then generated from this en face OAC map by using the automated Otsu's histogram thresholding method and removing small areas less than 125 μm in greatest linear dimension (GLD, consistent with human grader criterion). Theoretically, this binary image would be sufficient to identify the regions occupied by large drusen (≥125 μm in GLD) with high OAC values. In practice, there is no guarantee that the segmentations of RPE are perfect, especially in the area with a V-shape appearance at the border region of some drusen, for example at the positions pointed by green arrows in Fig.2.10 D-E,

which would make the RPE segmentation to slightly deviate from the true RPE position. Such deviation can lead to false positive identification of the calcified drusen (e.g., those pointed by the green arrows in Fig. 2.10 C and Fig. 2.10 F). One approach to minimize such false positive identifications is to further optimize the proposed RPE segmentation strategy by taking these special cases into the formulation of the segmentation algorithm. However, in this study, we instead introduced a constraint on the resulting binary map (Fig. 2.10 F), i.e., the 2nd step below.

The second step is to obtain a binary map corresponding to hypoTDs in the sclera, which is used to constrain the possible locations of calcified drusen identified from the 1st step. Conventionally, the hypoTDs can be identified from the en face structural image generated by the subRPE slab. However, the large choroidal vessels often complicate the identification of the hypoTDs using this method. To avoid this complication, we instead defined a slab located within the sclera where the OCT signal is more homogeneous, while preserving the appearance of the hypoTDs (e.g., pointed by arrow in Fig. 2.10 G). The largest distance between BM and choroid-sclera boundary, denoted as X μm for simplicity, was first calculated using a validated and published automated algorithm (38). Then the slab from X μm to (X + 40) μm below BM (shown in yellow lines in Fig. 2.10 G) was used to generate an en face OCT sub-choroid image using a mean intensity projection method (Fig. 2.10 H). Finally, the en face OCT sub-choroid image was binarized (Fig. 2.10 I) using a locally adaptive thresholding method.

The final binary map (Fig. 2.10 J) is obtained by the product between the first (Fig. 2.10 F) and second (Fig. 2.10 I) binary maps, showing the regions that are occupied by the calcified drusen. With this final binary map, it is then trivial to calculate the calcified drusen volumes when combined with the drusen map shown in Fig. 2.10 B.

In order to validate and compare the outcomes from the proposed automated algorithm, the calcified drusen were manually outlined by two independent expert graders (J.L. and M.S.) using Photoshop (Adobe Systems, San Jose, California, USA), and agreement was reached between the two graders regarding the area of calcified drusen. In cases of disagreement, a senior grader (P.J.R.) worked as the adjudicator.

2.3.2.5 Statistical analysis and evaluation metrics

Scatter plots along with Pearson correlation analyses were used to explore the relationship between the area and volume measurements of the calcified drusen from the manual segmentations and the automated algorithm. Statistical analysis was performed using GraphPad Prism (GraphPad Software, San Diego, CA, USA).

To evaluate the performance of the algorithms, Dice similarity coefficient (DSC), pixel-wise sensitivity, and specificity were measured on the data set:

$$\text{DSC} = \frac{2\,\text{TP}}{2\,\text{TP}+\text{FP}+\text{FN}} \quad (3)$$

$$\text{Sensitivity} = \frac{\text{TP}}{\text{TP}+\text{FN}} \quad (4)$$

$$\text{Specificity} = \frac{\text{TN}}{\text{TN}+\text{FP}} \quad (5)$$

where TP indicates true positive, TN indicates true negative, FP indicates false positive, and FN indicates false negative. Here the areas outlined by the human graders were considered as ground truth or reference standard.

2.3.3 Result

A total of 29 eyes with nonexudative AMD and calcified drusen from 29 patients were recruited in this study. 28 of these eyes contained hyper reflective foci lesions and 6 eyes had GA.

In the evaluation, we also evaluated the performances of the algorithm without employing the 2nd step to show the necessity of using the hypoTD information appearing in sub-choroid slab to minimize the false positive identifications, at least in the current study. The reason for this evaluation is that sub-choroid evaluation requires reliable OCT signals from deep choroid and sclera structures, which is achievable for SS-OCT imaging but often difficult for SD-OCT imaging. For simplicity in the evaluation, we named this evaluation as AccuRPE. Table 2.1 shows the results of our analyses. The mean DSC was 40.39 % when using the manufacturer's segmentation and 47.65 % using the OAC method, respectively. Note that the manufacture and OAC methods did not involve the sub-choroidal information. This value was improved to 51.21 % when using the proposed adjustment of RPE segmentation alone, i.e., the AccuRPE. However, when the sub-choroid information was used in the algorithm, the mean DSC of the proposed algorithm was significantly improved to 68.27% (AccuRPE vs Proposed approach, P value of paired t-test < 0.0001). Taken together, these analyses demonstrate that the proposed methods outperform either manufacture or traditional OAC approach, with the method being the most accurate when the hypoTD information in the choroid is considered in the algorithm.

Table 2.1 Performance for calcified drusen segmentation among different methods

Metrics	Manufacture approach	Prior OAC approach	Proposed approach	AccuRPE
DSC (%, mean ± SD)	40.39 ± 26.55	47.65 ± 24.16	68.27 ± 11.09	51.21 ± 20.84
Sensitivity (%, mean ± SD)	53.15 ± 29.64	70.14 ± 21.79	77.54 ± 12.24	77.40 ± 13.66
Specificity (%, mean ± SD)	98.96 ± 0.64	98.87 ± 0.76	99.60 ± 0.18	98.88 ± 0.69

AccuRPE denotes the proposed method with the step 1 only in the proposed algorithm.

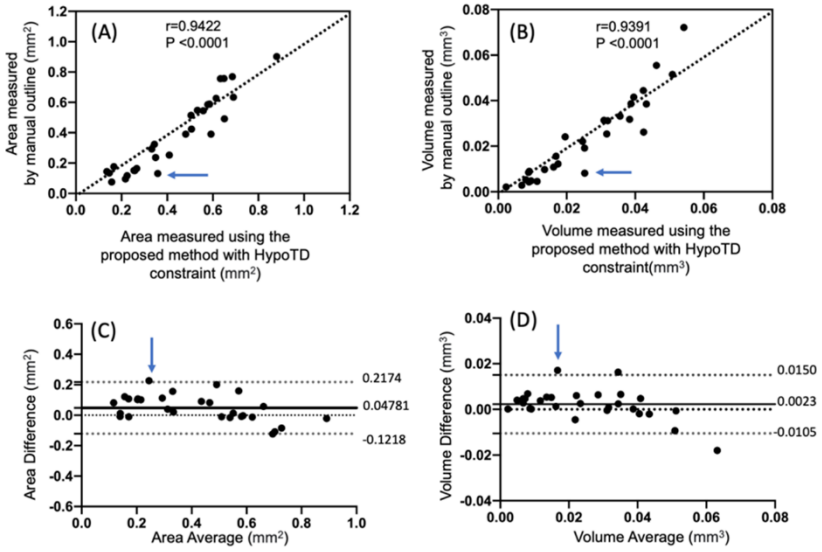

Fig 2.11 Areas and volumes of calcified drusen measured by the proposed automated methods vs the ground truth (by human graders).
(A) Scatter plot of the area measurements of identified calcified drusen against manual measurements showing a strong correlation (r=0.9422, p<0.0001), and (B) corresponding scatter plot of the volume measurements with a correlation (r=0.9391, p<0.0001). (C and D) Bland-Altman agreement analysis of identified calcified drusen against manual measurements, where the solid line represents the bias, and the dashed gray lines represent the upper and lower 95% limits of agreement.

Fig. 2.11 shows the quantitative scatter plots of the areas and volume measurements of identified calcified drusen along with Pearson's correlation analyses for the proposed algorithm vs the manual segmentations, respectively. A significant correlation was found between the measurements of the calcified drusen area ($r = 0.9422$, $p < 0.0001$, Fig. 2.11 A), and the corresponding volume measurements ($r = 0.9391$, $p < 0.0001$, Fig. 2.11 B). Bland-Altman analysis showed that the average bias of the area measurements was 0.04781 mm^2 (95% limits of agreement [–0.1218, 0.2174], Fig. 2.11 C) and the average bias of the corresponding volume measurements was 0.0023 mm^3 (95% limits of agreement [–0.0105, 0.0150], Fig. 2.11 D) between automated and manual approaches. Therefore, the measurements of calcified drusen computed using the proposed method tended to be a little larger than those produced by the manual segmentations.

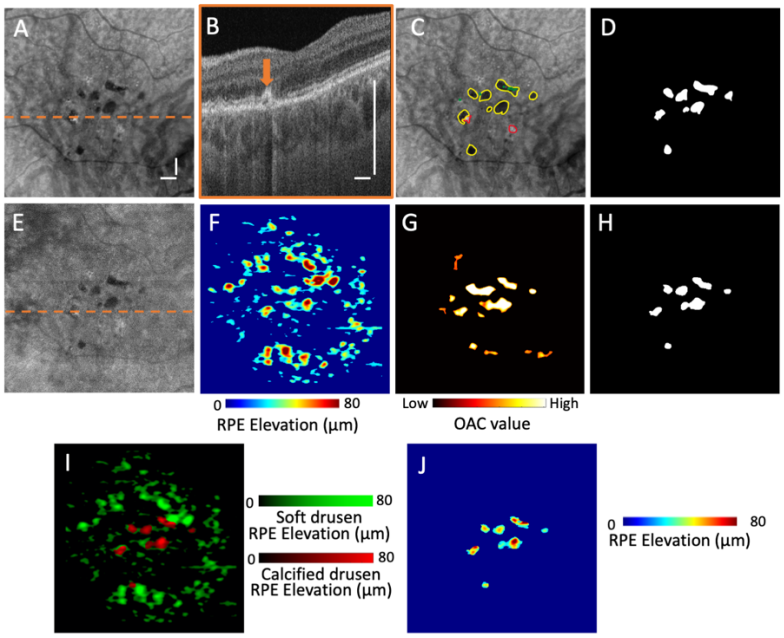

Fig 2.12. Representative segmentation results of calcified drusen taken from an eye in 68-year-old female patient by both the manual method (top row) and the proposed algorithm (bottom row).
(A) en face OCT subRPE image. (B) An OCT B-scan with its location shown as dashed line in (A) where a calcified druse can be identified. (C) Manual outlines on the subRPE image in (A) of calcified drusen (yellow outlines), hyperreflective foci (green outlines), and choroidal hypertransmission defects (red outlines). (D) Binary image showing the regions with calcified drusen segmented by human graders. (E) en face OCT sub-choroid image obtained by a slab of 40μm thickness with its anterior line defined by shifting the BM segmentation by the maximal thickness of the choroid, showing minimal contamination of choroidal vessels. (F) en face drusen map with the color indicating the elevation distance of RPE. (G) en face maximum mean projection OAC image between RPE and BM with the color indicating the values of OAC. (H) Binary map resulted from (G) to indicate the regions occupied by the calcified drusen using the automated method. (I) An en face composite map to visually indicate whether a druse is calcified within the drusen map (F), which was obtained with the aid of (H) when displaying (F) where the regions of calcified drusen are displayed with red color and the soft drusen are displayed with green color. Color bar represents the distance between RPE and BM.(J) en face calcified drusen map with the color indicating the elevation distance of RPE. Scale bar represents 500 μm.

Fig 2.12. demonstrates these results for one representative eye with nonexudative AMD and calcified drusen. Overall, there was good agreement between the segmentations from the automated strategy (Fig. 2.12 H) and those from the human graders (Fig. 2.12 D), with a dice coefficient of 75.81%. The segmentations of calcified drusen can be used to visualize the calcified drusen as a subset of all drusen, which may be useful, for example, in investigating the progression from soft drusen to calcified drusen. For example, the binary map of Fig. 2.12 H can be combined with the drusen map of Fig. 2.12 F to generate a composite map of Fig. 2.12 I to differentiate the calcified drusen (red color) from the soft drusen (green color) at a single glance. It is also trivial to show the RPE elevation map for the calcified drusen only (Fig. 2.12 J), which may also be useful in the clinical investigations. Combining the binary maps (Fig. 2.12 D and 2.12 H) with the drusen map in Fig. 2.12 F, the quantitative volume measurements of the calcified drusen were 0.0211mm^3 and 0.0246 mm^3 for the manual and automated strategies, respectively.

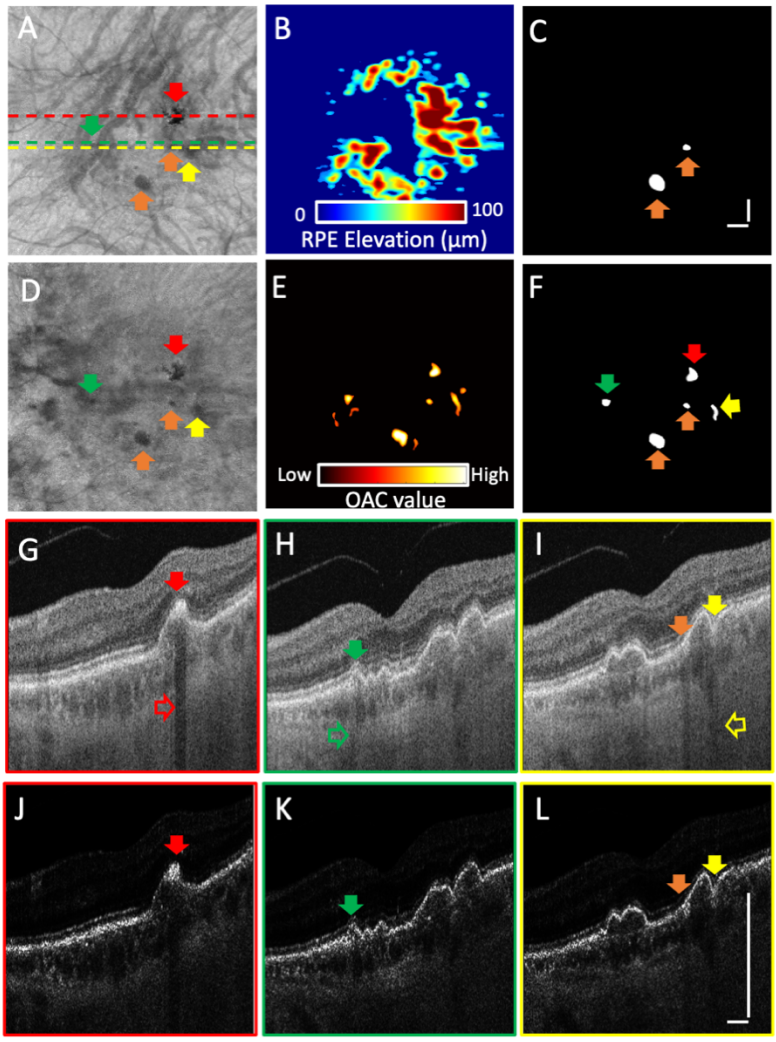

Fig 2.13. An example from an eye in 74-year-old male patient showing the areas of calcified drusen segmented by the algorithm being a relatively large disagreement with the areas segmented by human graders.
(A) en face OCT subRPE image with highlighted B-scan positions for detailed inspections of segmented calcified drusen by both the manual and automated approaches. (B) en face drusen map with the color indicating the elevation distance of RPE. (C) Binary map resulted from the manual segmentation, showing the regions identified with calcified drusen. (D) en face OCT sub-choroid image showing the hypoTDs with minimal contamination of choroidal vessels. (E) en face maximum mean projection optical attenuation coefficient (OAC) image of a slab taken between retinal pigment epithelium (RPE) to Bruch's membrane (BM), showing the OAC strength within the drusen. (F) Binary map resulted from the automated algorithm showing the regions occupied by the identified calcified drusen. (G-I) Representative OCT B-scans with their locations indicated by the dashed lines in (A); and (J-L) the corresponding OAC B-scans, respectively. In the images, the orange arrows indicate the true positive area detected by both the automated and manual methods. The green arrows point to a calcified druse that was detected by the automated method but missed by the human graders. The yellow arrows point to the position where the automated algorithm led to a false positive identification of the calcified druse due to a clear challenge of RPE segmentation at this location. The red arrows point to a pigment clump on the RPE, which was falsely identified as a calcified druse by the automated method but correctly excluded by the manual method. Scale bar represents 500 μm.

Figure 2.13 shows an example from a case (pointed by blue arrow in Fig. 2.11) with an obvious disagreement between the automated and manual segmentations (see Fig. 2.13 C vs Fig. 2.13 F). For this case, the dice coefficient was 50.68%, and the measured area and volume of calcified drusen were 0.1315 mm^2 and 0.0081mm^3 for manual segmentation, and 0.3584mm^2 and 0.0252mm^3 for the automated strategy,

respectively. To inspect in detail the possible reasons for the disagreement, we browsed through B-scan by B-scan in the 3D volume. Arrows show the representative positions with possible true/false positive and true/false negative identifications of the calcified drusen by both the manual and automated methods. The orange arrows point to the lesions that were correctly identified as calcified drusen by both the methods. The green arrows point to a true calcified druse that was correctly identified by the automated method but was missed by the human graders, probably because of its small size and undiscernible hypoTD in choroid (Fig. 2.13 A). Note that the hypoTD feature is present in the B-scan (hollow green arrow, Fig. 2.13 H) and heterogenous OCT reflectivity with the druse. The yellow arrows point to a position that was falsely identified as a calcified druse by the algorithm but correctly excluded by the human graders. This false-positive identification can be explained by an incorrect segmentation of the RPE (because of its V-shape) and by the RPE pigments clumped at the apex of the V-shape that strongly attenuates the light transmission, leading to a hypoTD appearance in the choroid and below (hollow yellow arrow, Fig. 2.13 I). The red arrows point to the position where there were migrated pigments attached to the RPE, which was falsely identified by the automated algorithm as a calcified drusen but was excluded by the manual graders. The highly scattering nature of the pigment clump that is attached to the RPE confuses the automated RPE segmentation algorithm, which overcorrects the RPE by the thickness of the pigment clump. To mitigate this mis-identification, one option is to use an automated algorithm of identifying the hyperreflective foci to exclude the regions designated as hyperpigmentation on RPE. Another option but more laborious is to manually check individual B-scans to confirm wherever the calcified drusen are correctly identified by the algorithm.

2.3.4 Discussion and conclusion

Qualitative and quantitative assessments of calcified drusen and soft drusen are of great clinical importance when evaluating AMD process. However, to the best of the authors' knowledge, no study regarding automated segmentation of calcified drusen has been reported. In this study, we proposed an automated algorithm using OCT-derived OAC features to improve the RPE segmentation and provide a more accurate drusen area map compared to previous methods. Based on this improvement, we proposed a novel automated strategy to segment and quantify the area and volume of calcified drusen. Although there is no consistent definition of calcified drusen, several groups reported that calcified drusen showed heterogeneous internal reflectivity within drusen (HIRD) on OCT B-scans (13,14,55,71,72). Moreover, Tan et al. (14) proposed a four-stage pathway for druse progression to HIRD, stating that drusen with hyperreflective contents but without a hyporeflective core were at an early stage of HIRD. In this study, both HIRD with and without a hyporeflective cores were considered to be calcified drusen, which is the

rationale of the first step in our automated strategy for segmenting calcified drusen (Fig. 2.10) because these HIRD are highly scattering and can be contrasted by OAC. Suzuki et al. (56) and Liu et al. (56) reported that there were shadows beneath calcified drusen, a feature which may be due to the attenuation or scattering of incident light caused by calcified nodules. These shadows give rise to the appearance of hypoTD on sub-RPE and sub-choroidal images. The combination of higher OAC within drusen and hypoTDs below BM are used in our automated algorithm to segment calcified drusen from 3D OCT scans.

The proposed automated algorithm was compared with calcified drusen segmentation performed by human graders. Some differences were observed when a calcified druse was small causing less attenuation of the OCT light entering the deeper structures than larger lesions, which leads to a reduced contrast of hypoTD appearance in the en-face subRPE images by the green arrows pointing to algorithm identified calcified druse in Fig. 2.13. Such low contrast appearance of hypoTDs makes the human graders difficult to judge, thus often leading to missed grading of the calcified drusen. However, in this example, the automated algorithm appears more sensitive to these small lesions, but the significance of these small lesions remains to be investigated.

There are several possible situations that may cause false positive segmentations of the calcified drusen. Fig. 2.13 shows an example where a pigment clump attached to the RPE was falsely identified as calcified drusen by the automated segmentation method. This situation presents a challenge for the proposed automated RPE segmentation, which might place the RPE above the pigment clamp leading to erroneous identification of the pigment clump as calcified drusen. These foci of hyperpigmentation can also be identified using another algorithm designed to identify these lesions (16), and any overlap between the two algorithms could be investigated further. Overall, the automated algorithm appears to have a small bias compared to manual outlines, over-estimating the areas of calcified drusen compared with the human graders (Fig. 2.11).

The current development was based on SS-OCT imaging, and it is unknown if the proposed method can be applied to spectral domain OCT (SD-OCT) datasets since SD-OCT has a worse sensitivity roll-off along the depth and higher optical scattering property of the RPE complex compared with SS-OCT. In this case, the use of the hypoTD information in the sub-choroid slab, even in the subRPE slab, could be problematic. For the development of an algorithm that would also be applicable to the SD-OCT imaging, the algorithm would be ideal if only the step 1 in the proposed automated approach (Fig. 2.10) is involved. This will be our immediate future effort to further improve and optimize the RPE segmentation algorithm so that it can cope with the special cases as we discussed above.

One important future direction is the development of deep learning algorithms to improve the performance and efficiency of calcified drusen segmentation. However, this would require annotated features from a large number of OCT datasets, which is a process that is underway. It is reasonable to believe that the

proposed automated algorithm would play an important role in guiding manual graders and facilitating the annotations of calcified drusen needed to develop deep learning algorithms.

In conclusion, we have proposed a novel strategy to segment and quantify calcified drusen via the use of its high optical scattering properties and the characteristic hypotransmission defects observed in slabs below BM. Moreover, we demonstrated an improved RPE segmentation that should provide more accurate drusen maps.

2.4 Outer retinal layer segmentation using deep learning.

2.4.1 Introduction

OCT has revolutionized the field of ophthalmology by providing high-resolution 3D images of retinal layers (32,35). These images offer invaluable insights into the microstructural and microvascular changes that arise and progress in eyes with AMD. The progression of these changes over time plays a crucial role in the staging, treatment planning, and monitoring of AMD. The widespread use of OCT in ophthalmology has facilitated the identification of OCT biomarkers associated with the progression from early to late AMD. These biomarkers include increased central drusen volume (>0.03 mm^3) (9,10), the presence of calcified/refractile drusen (13,14), hyperreflective foci (15–17), reticular pseudodrusen (17–19), components of outer retinal atrophy (19). Among these risk factors, assessing photoreceptor degeneration in OCT imaging presents a significant challenge, both technically and clinically.

It is well known that components of outer retinal atrophy encompass external limiting membrane (ELM) descent, hyporeflective wedges, ELM and ellipsoid zone (EZ) disruption, as well as the subsidence of inner nuclear layer (INL) and outer plexiform layer (OPL) (19). While directly measuring and quantifying these imaging features is challenging, outer retinal layer (ORL) thickness may serve as a surrogate marker for assessing components of outer retinal atrophy. This is because all of these imaging features contribute to the thinning of the ORL. Additionally, our previous study has reported a significant negative correlation between ORL around GA and the annual enlargement rate of GA (73), suggesting ORL thickness is a critical biomarker in predicting the growth of GA.

Although several automated algorithms have been developed and tested to automatically segment retinal layers on OCT images, such as the active contour (74), graph search (75–77), and deep learning approaches (68,78–85). However, each method has its own limitations. For example, traditional computer vision methods face challenges in handling pathologic changes, making it difficult to achieve an optimal balance between disease-related disruptions and spatial connectivity. Studies regarding deep learning methods for

OCT imaging segmentation have primarily focused on SD-OCT datasets (68,78,81,83,84), raising uncertainty about the applicability of these methods to SS-OCT datasets.

In this study, we proposed an automated algorithm capable of measuring the thickness of the ORL in both swept source OCT (SS-OCT) and spectral domain OCT (SD-OCT) datasets. In order to demonstrate the effectiveness of our algorithm across both SS-OCT and SD-OCT modalities, we performed a comparative analysis of ORL thickness measurements. These measurements were obtained by employing our proposed algorithm to both SS-OCT and SD-OCT datasets.

2.4.2 Method

This prospective OCT imaging study was approved by the Institutional Review Board of University of Miami Miller School of Medicine. The study was performed in accordance with the tenets of the Declaration of Helsinki and complied with the Health Insurance Portability and Accountability Act of 1996. Through a retrospective review of subjects enrolled from April 2016 to August 2022, a total of 199 eyes were included, comprising 80 normal eyes without any ocular disease, 30 eyes with reticular pseudodrusen only, 49 eyes displaying typical soft drusen only, and 40 eyes with late AMD accompanied by GA.

2.4.2.1 Image Acquisition

Two optical coherence tomography (OCT) instruments were utilized in this study: the PLEX Elite 9000 (Carl Zeiss, Meditec Inc., Dublin, CA) for SS-OCT and the Cirrus HD-OCT (Carl Zeiss, Meditec Inc., Dublin, CA) for SD-OCT. The SD-OCT instrument utilized a central wavelength of 840 nm and a scan rate of 68,000 A-scans/second. The scanning pattern for the 6x6 mm SD-OCT scan consisted of 350 A-scans per B-scan and 350 B-scans per volume, with each B-scan repeated twice within the macular cube protocol. This setup resulted in a uniform spacing of 30 μm between A-scans. The SS-OCTA instrument used a central wavelength of 1050 nm and a scan rate of 100,000 A-scans/second. The 6x6 mm SS-OCTA scan pattern included 500 A-scans per B-scan and 500 B-scans per volume, with each B-scan repeated twice within the macular cube protocol. This configuration provided a uniform spacing of 12 μm between A-scans. Both instruments featured a full width at half maximum axial resolution of 5 μm in tissue and an estimated transverse resolution of 15 μm at the retinal surface.

A total of 40 eyes presenting with typical soft drusen, and 40 eyes with GA, underwent both SS-OCT and SD-OCT. The remaining 119 eyes underwent SS-OCT only.

2.4.2.2 Automated Segmentation of the Outer Retinal Layer

In this study, the ORL is defined as the region extending from the inner boundary of the outer plexiform layer (OPL) to the retinal pigment epithelium (RPE) when the RPE is visible (73). However, in cases where there is complete loss of the RPE in GA lesions, the ORL is defined as the region extending from the OPL to Bruch's membrane (BM).

For medical image segmentation, convolutional neural networks (CNNs) have emerged as the dominant approach due to the ability to learn highly complex features and models across different levels of abstraction from training data (86). Among the various architectures available, U-Net (87), which consists of a symmetric encoder-decoder network, stands out as the most widely adopted. However, CNNs-based model heavily depends on the convolution operation that restricts the receptive field (e.g., 3 × 3 kernel size) and presents challenges in learning long-term information. The vision transformer (ViT), with global self-attention mechanisms, is considered a viable alternative to CNNs (88). In 2021, TransUNet was proposed, which integrates both transformers and CNNs in encoder to leverage detailed high-resolution spatial information from CNNs and the global context encoded by ViT (89). Although TransUNet has achieved a good performance in computer tomography image-based segmentation, the retinal features from the cross-sectional OCT images are highly different from the organ features in CT images. Hence, to perform the ORL segmentation task in this study, a modified TransUNet model was trained and validated with our OCT data. Fig. 2.14 demonstrates the architecture of the TransUNet model used in this study, with the specifications all labeled. The modified TransUNet model includes an encoder, decoder, and bottleneck. The encoder block consists of four convolutional layers with ReLU activation, designed to extract features from OCT images. Subsequently, a bottleneck block with six transformer layers was employed to apply multi-head self-attention to image patches, capturing long-term information for the extracted features from the previous encoder block. Finally, a decoder block with four transpose convolutional layers was utilized to upsample the feature maps, restoring their shape to match the original input data.

The Adam optimizer with a learning rate of 0.0001 was used, the model evaluation metric was defined as the intersection over union (IoU), and the loss function utilized for training was the binary crossentropy loss. This model was trained with 200 epochs with a patience for early stopping of 30 epochs, and only the model with the best metric was saved when the validation loss was not updated under 30 training epochs. For this study, the model was implemented in Keras using TensorFlow 2.9.0 as the backend, and training was conducted using a 24GB NVIDIA 4090 GPU.

With the confirmed information of clinical diagnoses, the boundaries that define the ORL were annotated from a total of 2,000 representative OCT B-scans by two clinical experts (F.H. and G.H.) using a custom-built software that was improved from the segmentation and annotation software package originally developed in. The consensus on the annotation of ORL boundaries was reached between both graders. In cases of disagreement, a senior grader (P.J.R.) was the adjudicator. For training purposes, we utilized 32 labeled eyes, with 16 eyes (i.e., 800 B-scans) from SS-OCT and 16 eyes (i.e., 800 B-scans) from SD-OCT. Within the training dataset, we further applied a 75:25 split between training and validation at the eye level to ensure an effective and reliable evaluation process. The remaining 8 labeled eyes, comprising 4 eyes (i.e., 200 B-scans) from SS-OCT and 4 eyes (i.e., 200 B-scans) from SD-OCT, were reserved for testing. These B-scans were extracted from 20 volumes of SS-OCT scans and 20 volumes of SD-OCT scans, respectively. These scans were obtained from a total of 40 eyes out of the 199 eyes included in the study. The composition of the 20 SS-OCT volume scans encompassed 2 normal eyes, 2 eyes with macular reticular pseudodrusen (RPD), 8 eyes with drusen, and 8 eyes with hyperTDs. The 20 SD-OCT volume scans comprised 10 eyes with drusen and 10 eyes with hyperTDs. Importantly, there was no overlap between the eyes included in the SS-OCT and SD-OCT scans within the training dataset. To consider the practical and pathological manifestations of AMD features in the OCT scans, the selected B-scans encompassed a diverse range of imaging features including normal scans, a range of soft drusen sizes, calcified drusen, hyperreflective foci, macular reticular pseudodrusen, and hyperTDs. The details of the training and testing datasets are shown in Table 1. To avoid over down-sampling of input images in the A-line direction, all images were first automatically cropped to 512 (A-line direction) × 500(SS-OCT)/350(SD-OCT) pixels and then were resized to 512 × 512 pixels.

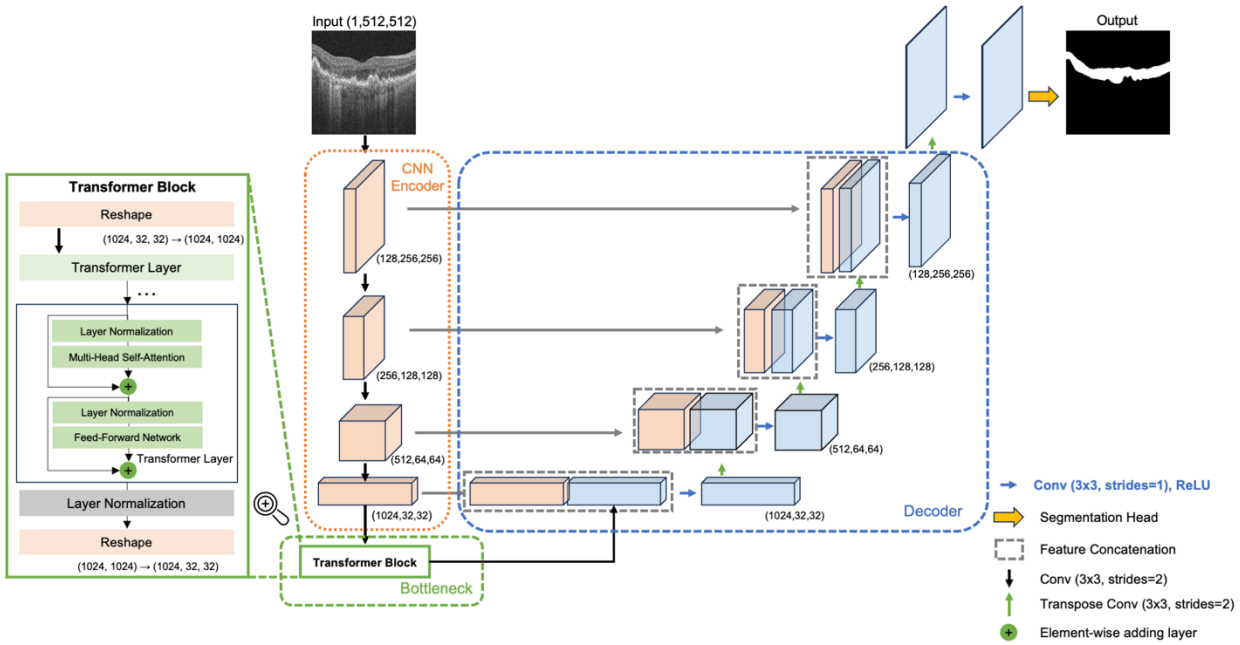

Fig 2.14 The TransUNet model architecture and specifications used to perform outer retinal layer segmentation.

Table 2.2 Training and testing datasets*

	Training	**Validation**	**Testing**
Number of eyes (SS-OCT/ SD-OCT)	24 (12/12)	8 (4/4)	8 (4/4)
Number of representative B-scans (SS-OCT/ SD-OCT)	1200 (600/600)	400 (200/200)	400 (200/200)

*Datasets were obtained from normal eyes and eyes with reticular pseudodrusen, intermediate and large drusen, calcified drusen, hypertransmission defects, and hyperreflective foci

2.4.3 Result

To compare the performance difference between original U-Net and Trans U-Net, these two separate models were trained using the same datasets shown in Table1. Table 2.3 shows their specific IoUs for training, validation, and testing datasets. In the eight eyes or 400 B-scans in the testing set, the Trans U-Net model significantly outperformed the original U-Net model (IoU: 0.9198 vs 0.9698).

Table 2.3. Training and testing results

Intersection Over Union (IoU)	Original U-Net	TransUNet
Training	0.9574	0.9850
Validation	0.9522	0.9748
Testing	0.9189	0.9698

Figure 2.15 demonstrates the automatic segmentation of two representative eyes with drusen and GA, respectively. Notably, these eyes were not included in the training dataset. Figs. 2.15 A, D, G and J show ORL thickness map obtained from the corresponding 3D OCT scan, where the color indicates the distance between OPL and RPE/BM. Figs. 2.15 B, C, E, F, H, I, K and L show OCT B-scans with blue lines indicating the inner boundary of OPL and yellow lines indicating the RPE/BM location. Bule lines and yellow lines were derived from the automatic segmentation. Figs. 2.15 A-F show images acquired and measured using SS-OCT, while Figs. 2.15 G-L show the corresponding eyes obtained and measured through SD-OCT. Overall, the automatic segmentations and measurements show substantial agreement between the results from the SS-OCT and those from the SD-OCT.

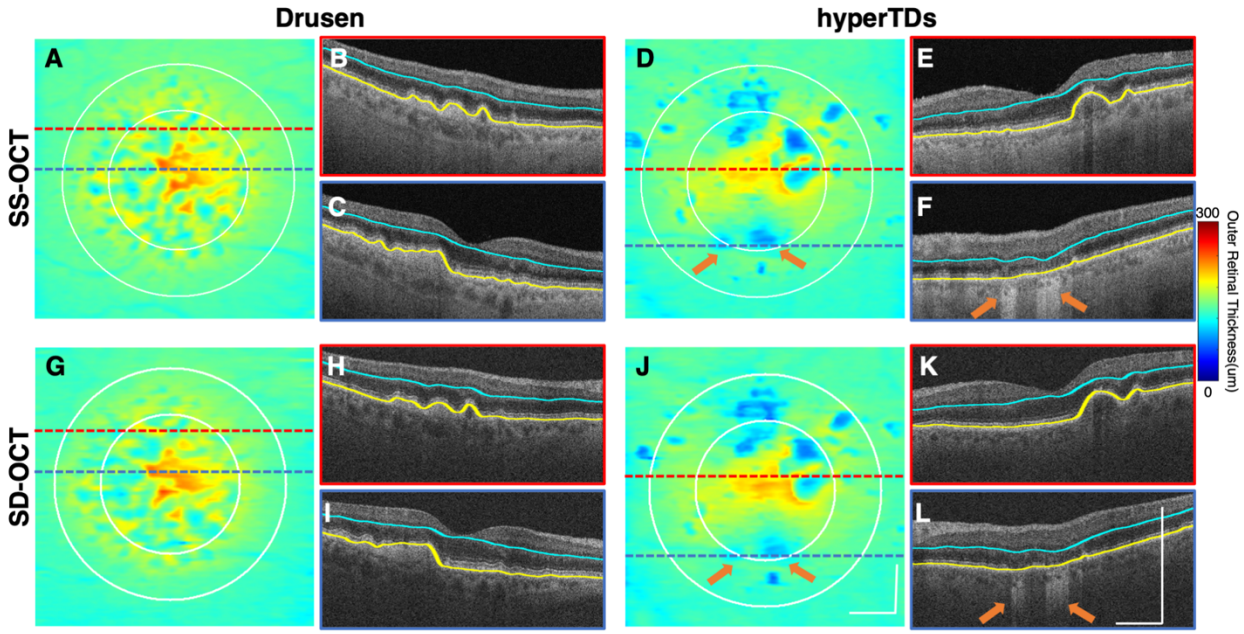

Fig 2.15 Representative automatic segmentation results of outer retinal layer (ORL) taken from an eye with soft drusen and an eye with geographic atrophy (GA) by both SS-OCT (top row) and SD-OCT (bottom row).
(A, D, G, and J) ORL thickness maps. (B, C, E, F, H, I, K and L) OCT B-scans with their locations shown as dashed lines in (A, D, G, and J) where drusen and GA can be identified. White circles indicate 3 mm and 5 mm diameter circles centered on the fovea. Scale bar represents 1mm.

In total, 40 eyes with typical soft drusen only and 40 eyes with GA were scanned by both SS-OCT and SD-OCT to compare the ORL thickness measurements from SS-OCT vs SD-OCT. Fig. 2.16 shows the quantitative scatter plots of automatic measurements of ORL thickness acquired by the SS-OCT vs the SD-OCT. A strong correlation was found between the measurements of ORL thickness in the 3-mm circle ($r = 0.9551$, $P < 0.0001$, Fig. 2.16 A) and 5-mm circle ($r = 0.9442$, $P < 0.0001$, Fig. 2.16 B) centered on the fovea. Bland-Altman analysis showed that the average bias of the measurements in the 3-mm circle was 0.5440 um (95% limits of agreement [−8.005, 9.093], Fig. 2.16 C) and the average bias of the corresponding measurements in the 5-mm circle was 1.392 um (95% limits of agreement [−5.335, 8.119], Fig. 2.16 D) between SS-OCT and SD-OCT. Therefore, the measurements of ORL thickness computed using the SS-OCT tended to be a little thicker than those produced by the SD-OCT.

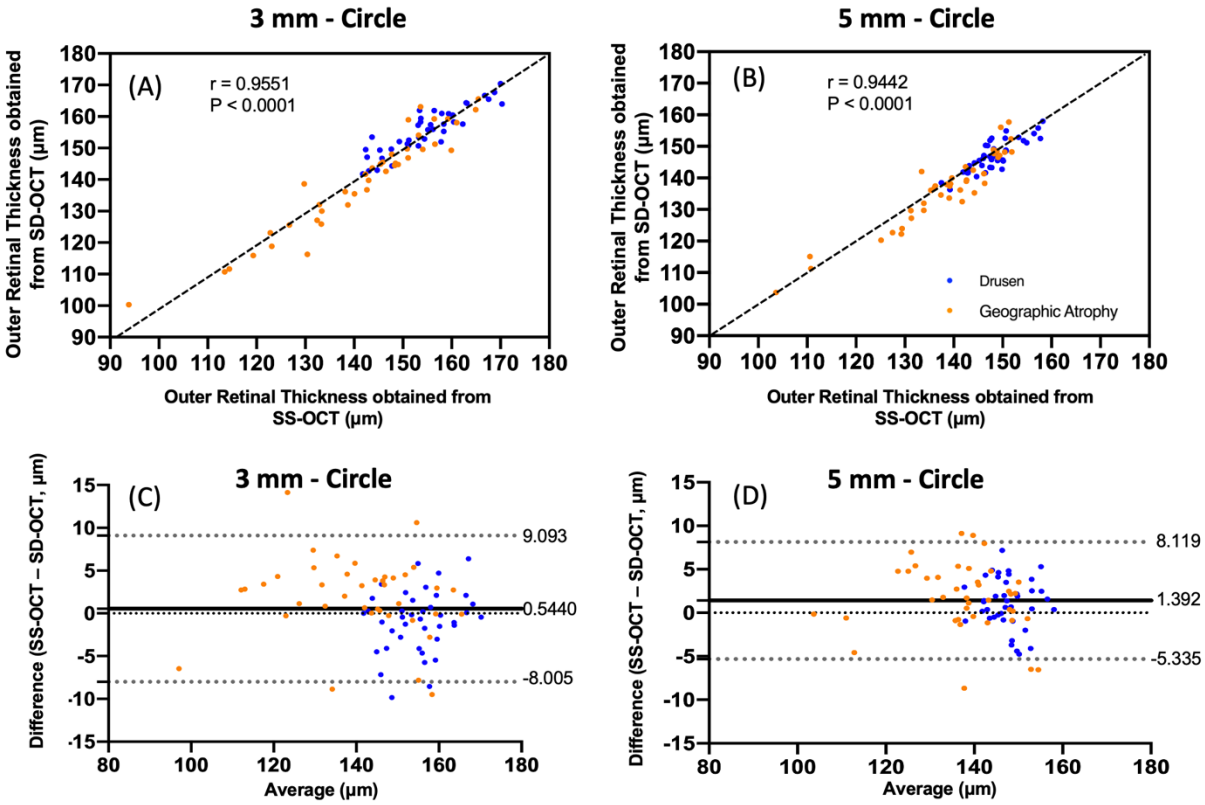

Fig 2.16 Automatic measurements of outer retinal layer (ORL) thickness acquired by the SS-OCT vs the SD-OCT.
(A) Scatter plot of the ORL measurements from SS-OCT against SD-OCT showing strong correlation in the 3 mm-circle ($r = 0.9551$, $P < 0.0001$), and (B) in 5 mm-circle ($r = 0.9442$, $P < 0.0001$) centered on the fovea. (C and D) Bland-Altman agreement analysis of ORL measurements from SS-OCT against SD-OCT, where the solid line represents the bias, and the

dashed gray lines represent the upper and lower 95% limits of agreement. Blue dots represent drusen only eyes, and orange dots represent geographic atrophy (GA) eyes.

2.4.4 Discussion and conclusion

There remains an urgent need to identify surrogate endpoints that can predict the high risk of progression to geographic atrophy (GA) in AMD. Pathological changes in the ORL have been recognized associated with AMD progression. However, directly quantifying these pathological changes, such as disruption of ellipsoid zone and external limiting membrane, is challenging due to its inherent complexity, the influences of various shadows (e.g., shadows from vessels and pigments), the limited axial resolution of OCT, and the extremely thin nature of individual layers in the ORL (90–93). As an alternative, outer retinal layer (ORL) thickness may serve as a surrogate marker for assessing ORL alterations. To investigate whether ORL thickness could serve as a biomarker for evaluating AMD, we proposed a deep learning-based algorithm capable of automatically measuring the thickness of the ORL in both SS-OCT and SD-OCT datasets. Our deep learning-based approach demonstrated a high accuracy with a IoU of 0.9698 in the testing dataset in segmenting the ORL, allowing for reliable quantification of disease-related changes, such as loss of RPE, elevation of RPE, and subsidence of OPL. Strong correlation and agreement of ORL thickness measurements between SS-OCT and SD-OCT datasets further validated the robustness and applicability of the algorithm across different OCT modalities (Fig. 2.15 and 2.16). In addition to its application in evaluating AMD, ORL thickness have also been utilized for the detection of brain-related diseases (94,95) and diabetic macular edema(96), highlighting the potential future applications of our algorithm.

3 Chapter 3. Clinical Application of OCT in Ophthalmology

After exploring these innovative methods for OCT imaging, it's crucial to recognize their real-world significance in the field of ophthalmology. Building on the foundation of Chapter 2, this Chapter showcases the remarkable capabilities and potentials of OCT in clinical ophthalmology. Firstly, we investigate the symmetry of interocular choroidal thickness and vascularity index measurements in normal eyes using SS-OCT, finding choroidal differences between normal fellow eyes in adults without obvious pathology. This study aids clinicians and researchers in distinguishing expected asymmetric changes in normal eyes from changes associated with diseases. Secondly, we examine variations in the ORL thickness among different stages of age-related macular degeneration (AMD), revealing significant differences in ORL thickness measurements among various AMD stages, indicating the potential of ORL thickness as an independent biomarker for predicting AMD progression.

3.1 Interocular asymmetry of choroidal thickness and vascularity index measurements in normal eyes

3.1.1 Introduction

Identifying asymmetrical or unilateral features between fellow eyes is important in the investigations of ocular diseases that only affect one eye or are initiated unilaterally but eventually progress bilaterally. It is important to establish a baseline of interocular asymmetry in normal eyes that can be used to assist clinicians and researchers in differentiating pathological differences from physiological asymmetries. Previous studies have demonstrated that some degrees of non-pathologic asymmetry can exist in the retina and choroid between fellow eyes using optical coherence tomography (OCT).

Recent advances in swept-source OCT (SS-OCT) development make it an ideal tool for choroidal imaging because of its deeper penetration depth enabled by longer wavelength, faster imaging speed and negligible sensitivity roll-off (97). When investigating the choroidal symmetry in children (98) and young adults, a number of groups utilized spectral-domain OCT (SD-OCT) with enhanced depth imaging (EDI) (99). However, SD-OCT is limited by its depth of penetration, leading to relatively poor imaging quality in the choroidal layer. While EDI improves the quality of choroidal imaging, it only improves depth imaging within the macula and is difficult to perform a wide field-of-view (FOV) imaging (99). In addition, most of the participants of the above studies were less than 50 years old, which provides limited understanding of the choroidal symmetry within the elderly population. Although SS-OCT has been used to investigate interocular symmetry of the choroidal thickness in adults with normal eyes (100,101), the results were derived by using manual measurements from several selected B-scans, which is time consuming and augments the possibilities of subjective bias.

Recently, attention has been paid to mapping the choroidal thickness and choroidal vascularity index measurements from the entire 12x12 mm scan that encompasses a 40-degree FOV centered on the fovea. In prior work, we have generated a normative age-dependent database of choroidal thickness and choroidal vascularity index measurements using the SS-OCT 12x12 mm datasets (20). However, we did not study the extent of interocular symmetry in these eyes over the entire scanning region.

The purpose of this study is to use widefield SS-OCT imaging to assess whether physiological choroidal asymmetry exists between fellow normal eyes within the entire SS-OCT 12x12 mm scan regions. The extent of physiological choroidal symmetry was assessed by comparing the mean choroidal thickness (MCT) and choroidal vascularity index (CVI) measurements between the two normal eyes.

3.1.2 Methods

3.1.2.1 Study Participants

This was a cross-sectional study of SS-OCT choroidal imaging in normal adults with ages uniformly distributed from 19 to 89 years. This study was approved by the Institutional Review Board (IRB) of Medical Sciences Subcommittee at the University of Miami, Miller School of Medicine and was conducted in compliance with the Declaration of Helsinki (as revised in 2013). All the participants had a normal ocular history in both eyes. Study exclusion criteria included: (i) visual complaints; (ii) retinal, optic nerve or choroidal pathologies detected on examination or with OCT imaging; (iii) diabetes history; (iv) uncontrolled hypertension. The sample size was determined by the number of participants who met our inclusion criteria during the study period. All participants voluntarily gave written informed consents before scans were taken.

3.1.2.2 OCT imaging and axial length measurements

OCT scanning was performed using a commercial SS-OCT instrument (PLEX® Elite 9000, Carl Zeiss Meditec, Dublin, CA). This instrument was equipped with a 100kHz swept laser source with a central wavelength of 1050 nm and a spectral bandwidth of 100 nm, providing an axial resolution of ~5 μm in tissue. Each OCT scan centered on the fovea covered a FOV of 12x12 mm with a lateral resolution of ~20 μm, and a measured depth of 3.0 mm (1536 pixels) in tissue. The OCT angiographic scan pattern consisted of 500 A-lines per 6 mm horizontal B-scan, 500 B-scan positions along the vertical scanning dimension, and two repeated B-scans per B-scan position. A non-contact biometry instrument was used to measure axial length (IOLMaster, Carl Zeiss Meditec). Eyes were excluded from the study if their axial length was more than 26 mm, and OCT scans were excluded from this study if there were noticeable motion artifacts or signal strength was less than 7 (recommended by the manufacturer). All imaging scans and biometric measurements were performed by trained operators at the department of ophthalmology, bascom palmer eye institute, Miami, FL, USA.

3.1.2.3 Choroidal Segmentation

The choroidal slab was acquired by automatically outlining the choroidal boundaries (i.e., Bruch's membrane and choroid-sclera interface) using a validated algorithm (38). The contrast of the choroid-sclera interface (here referred to as the outer border of choroidal vessels (102)) was relatively low in the original OCT images because the intensity of OCT light is exponentially attenuated along its path as the light beam propagates through the highly scattering RPE complex and choroid (Fig 3.1 A, B). To enhance the contrast of the choroid-sclera interface in the OCT image, the algorithm applied an attenuation correction strategy consisting of attenuation compensation and exponentiation to the structural images (36,38) (Fig 3.1 C, D). Optic discs were excluded from the volumetric datasets before choroidal segmentation. The choroidal boundaries were then automatically detected through the graph search method (Fig 3.1 C, D). Even though previous studies have shown excellent agreement between this automatic method and manual segmentation (20,38). we still manually checked the automatic segmentation for accuracy once completed.

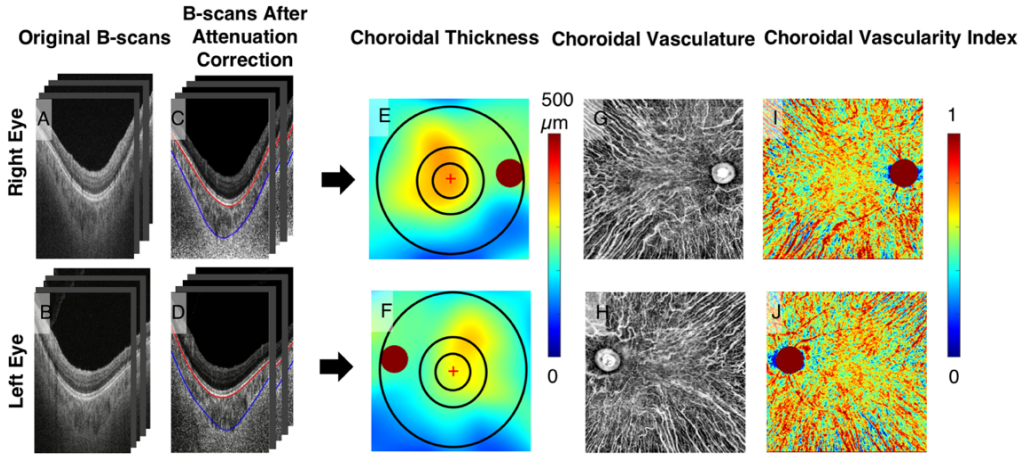

Fig 3.1 Cross-sectional B-scan and en face choroidal images taken of a 63-year-old woman.
(A and B) Original cross-sectional B-scans. (C and D) Cross-sectional B-scans after attenuation correction. Red lines highlight the upper boundary of the choroid (i.e., Bruch's membrane), and blue lines highlight the bottom boundary of the choroid (i.e., choroid-sclera interface). (E and F) Overlay of three concentric circles centered on the fovea on the choroidal thickness maps. These circles divide the 12×12 mm scan into 6 regions for quantification: the 2.5 mm circle, 5 mm circle, 11 mm circle, inner rim (from the 2.5 mm circle to the 5 mm circle), outer rim (from the 5 mm circle to the 11 mm circle), and the entire 12×12 mm scan. +: fovea. Color bar represents a depth range of 0 – 500 μm. (G and H) En face choroidal vasculature maps. (I and J) en face choroidal vascularity index maps. Color bar represents a value range of 0 – 1.

3.1.2.4 Mean Choroidal Thickness (MCT) Measurements

The distance between the Bruch's membrane and choroid-sclera interface was used to generate *en face* choroidal thickness maps (Fig 3.1 E, F), where the color represented a thickness range between 0 — 500 μm. On each *en face* map, three concentric circles centered on the fovea with diameters of 2.5 mm, 5 mm, and 11 mm, respectively, were created to generate 6 regions for quantification: the 2.5 mm circle, 5 mm circle, 11 mm circle, inner rim (from 2.5 mm to 5 mm circle), outer rim (from 5 mm to 11 mm circle), and

the entire 12x12 mm scan (Fig 3.1 E and F). The foveal location was automatically detected through searching the local minimum thickness of the retinal layers in OCT structural images. In this study, we used the MCT (referred to as the average value of the thickness within a region of interest) to represent the regional choroidal thickness (excluding the optic disc).

3.1.2.5 Choroidal Vascularity Index (CVI) Measurements

Fig1.1 C and D show B-scans with dark vascular structures within the choroidal layer. These structures are thought to be choroidal vessels because most of the light is scattered forward by the blood, allowing the large choroidal vessels to appear as dark regions (low backscattered light) with vessel-like shapes in the OCT images (103,104). In addition, the highly backscattering RPE significantly reduced the signal generated by the light that was backscattered by the choroidal vasculature. Therefore, it is difficult for conventional OCT angiography (OCTA) methods (35) to detect the choroidal blood flow signal (103,104). In this study, the choroidal vessels were obtained from the OCT structural images after attenuation correction by segmenting dark regions with the vessel-like shapes in the choroid using Otsu's method (20,38,105). For convenient visualization, we inverted the dark regions to appear bright (Fig 3.1 G, H). The CVI was estimated by dividing the number of pixels in the choroidal vessels by the total number of pixels in the choroidal slab. The *en face* CVI map was generated by mapping the CVI value at each A-line (Fig 3.1 I, J), where the color represents a CVI value range of 0 — 1. For comparison, the 12×12 mm scan of the CVI was also divided by using the concentric circles mentioned above.

3.1.2.6 Interocular Asymmetry Measurements

The interocular asymmetry in the MCT and CVI measurements was quantified by using signed difference and absolute difference. The signed difference was calculated by subtracting the left eye value from the right eye value. To visualize interocular asymmetry, we flipped the right eye *en face* images in the left-right direction, registered the two images at fovea and optic nerve head, and then generated *en face* maps of interocular difference (Fig 3.2).

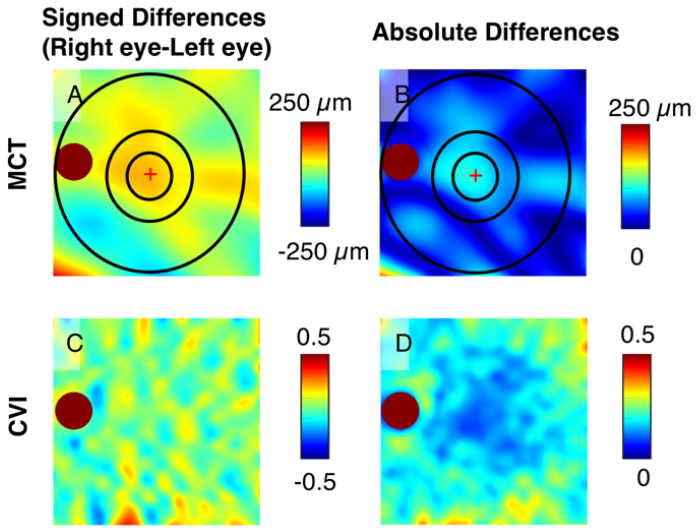

Fig 3.2 En face images of interocular choroidal differences.
(A) Signed interocular differences in mean choroidal thickness (MCT). Color bar represents a depth range of -250 μm – 250 μm. (B) Absolute interocular differences in MCT. Color bar represents a depth range of 0 – 250 μm. (C) Signed interocular differences in the choroidal vascularity index (CVI). Color bar represents a value range of -0.5 – 0.5. (D) Absolute interocular differences in CVI. Color bar represents a value range of 0 – 0.5.

3.1.2.7 Statistical Analysis

The data with normal distributions (e.g., MCT, CVI and signed interocular difference) were presented as the mean and standard deviation (SD), while the data without normal distribution (e.g., absolute interocular difference) were presented as the mean, SD, median and range. The strengths of correlations in corresponding regions of measurements between fellow eyes were analyzed by intraclass correlations (ICCs). ICCs >0.75 can be interpreted as strong or excellent, ICCs <0.3 are weak or poor, while intermediate ICCs are considered fair to good or moderate (106). Paired-sample t-tests were utilized to compare the measurements between fellow eyes.

The relationships between interocular differences in the MCT and CVI measurements were analyzed by using Pearson's correlation. Furthermore, the relationships between the interocular differences in MCT and CVI measurements and each of the variables: (i) participants' age, (ii) interocular differences of axial length, were studied by Pearson's correlation. Statistical analysis was carried out using MATLAB R2020b and IBM SPSS V25 (Armonk, NY), and scatter plots were generated using GraphPad Prism (GraphPad Software, San Diego, CA). Statistical significance is represented at two levels: * $P \leq 0.05$, ** $P \leq 0.01$.

3.1.3 Results

A total of 254 normal eyes from 127 participants ranging from 19 to 89 years of age were enrolled in this study. Five participants were later excluded: two because their axial lengths were greater than 26 mm, one because the entire choroidal layer was beyond the A-scan range, and two because they were uncooperative, could not fixate, and the scans could not be adequately obtained. The final analysis included 122 participants (244 eyes), 49 men and 73 women, with a mean age of 55.14 ± 19.38 years. The demographic characteristics of the participants are shown in Table 3.1. No significant differences were observed when comparing axial length between fellow eyes.

Table 3.1 Demographic characteristics of the participants in this study.

Characteristic	Total	Age Decades						
		19 — 29	30 — 39	40 — 49	50 — 59	60 — 69	70 — 79	80 — 89
Number of patients (Number of eyes)	122(244)	14(28)	19(38)	15(30)	18(36)	22(44)	18(36)	16(32)
Age (mean ± SD, years)	55.14 ± 19.38	24.57 ± 2.79	33.26 ± 2.54	45.13 ± 3.16	55.52 ± 2.81	63.99 ± 2.94	74.11 ± 2.81	83.25 ± 2.70
Gender(male/female)	49/73	7/7	11/8	4/11	2/16	10/12	8/10	7/9
Axial Length (mean ± SD, mm)								
Right Eye	23.84 ± 0.89	24.43 ± 1.07	24.01 ± 0.81	24.13 ± 0.83	23.69 ± 1.04	23.87 ± 0.78	23.39 ± 0.79	23.47 ± 0.63
Left Eye	23.83 ± 0.89	24.35 ± 0.98	23.97 ± 0.84	24.02 ± 0.87	23.73 ± 1.09	23.85 ± 0.77	23.36 ± 0.84	23.60 ± 0.63

Fig 3.1 shows the choroidal thickness, choroidal vascularity, and the choroidal vascularity index maps derived from a 63-year-old participant. On visual inspection, the *en face* choroidal thickness and CVI maps did not appear completely symmetrical. The choroidal thickness in the right eye appeared thicker than that in the left eye in the macular (5 mm circle) region. For CVI maps, a homogeneously distributed mix of red to blue colors can be seen in both eyes; however, subtle differences can also be observed between the two eyes. Fig 3.2 shows the interocular asymmetry maps derived from the same participant represented in Fig 3.1. The uneven appearance of the interocular asymmetry maps confirms the interocular choroidal differences shown in Fig 3.1. This participant demonstrated a thicker choroidal thickness in the 2.5 mm circle region in the right eye compared with that of the left eye (Fig 3.2 A). The MCT absolute difference between fellow eyes in the 2.5 mm circle region is the most obvious difference in the entire scanning region (Fig 3.2 B). Similarly, the CVI interocular asymmetry maps of this participant also showed varied differences across the entire scanned region between fellow eyes (Fig 3.2 C and D).

3.1.3.1 Mean Choroidal Thickness (MCT) and Choroidal Vascularity Index (CVI) Measurements

The values, correlation coefficients, and comparisons of the bilateral measurements in MCT and CVI measurements are summarized in Table 3.2. MCT in the 5-mm circle region measured 261.75 ± 80.67 μm

in right eyes and 251.22 ± 69.11 μm in left eyes. CVI in the 5 mm circle region was 0.618 ± 0.024 in right eyes and 0.625 ± 0.029 in left eyes. In all the regions, there was a strong correlation between fellow eyes in MCT, whereas there was only a moderate correlation between fellow eyes in CVI. MCT was statistically thicker in the right eyes than that in the left eyes in all the quantified regions. In contrast, CVI was statistically lower in the right eyes than that in the left eyes in the 2.5 mm circle, 5 mm circle, and inner rim regions. Fig 3.3 shows the correlation and Bland-Altman agreement analysis on MCT and CVI measurements in the 5 mm circle region between fellow eyes.

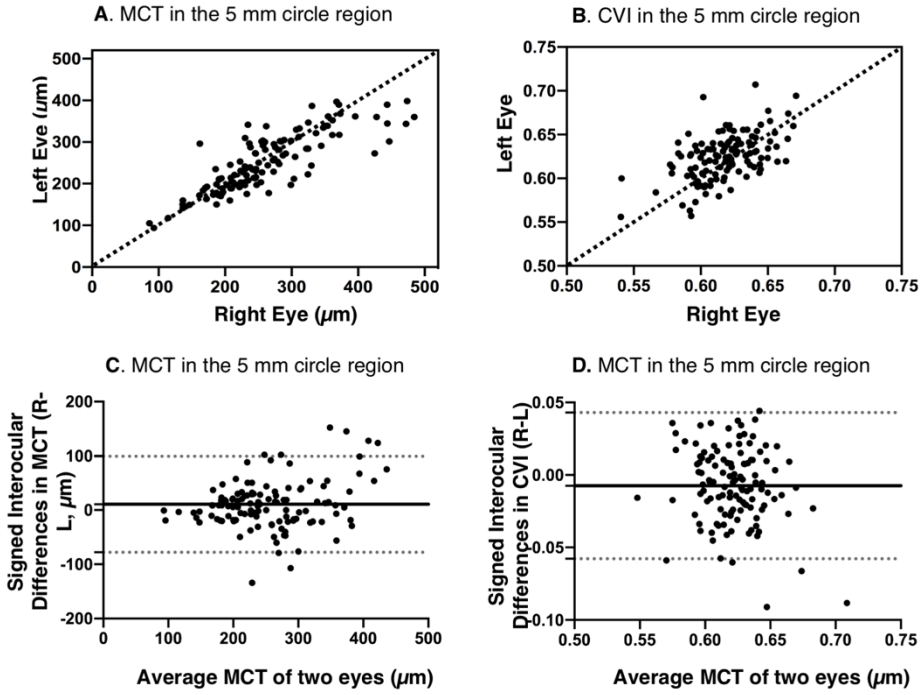

Fig 3.3 Correlation and Bland-Altman agreement analysis on mean choroidal thickness (MCT) and choroidal vascularity index (CVI) measurements in the 5 mm circle (macular) region between fellow eyes.
The slope of the dashed lines in the correlation analysis maps (A and B) is 1. The solid lines in Bland-Altman agreement analyses (C and D) represent the bias, and the perforated lines represent the upper and lower 95% limits of agreement.

Table 3.2 Mean choroidal thickness (MCT) and choroidal vascularity index (CVI) Measurements

Region Quantified	Mean Choroidal Thickness (MCT, n=122)				Choroidal Vascularity Index (CVI, n=122)			
	Right Eye (μm)	Left Eye(μm)	Interocular Intraclass Correlation Coefficient	P-value of paired T-test	Right Eye	Left Eye	Interocular Intraclass Correlation Coefficient	P-value of paired T-test
	Mean (SD)	Mean (SD)			Mean (SD)	Mean (SD)		
2.5 mm circle	274.09 (95.47)	260.03 (74.91)	0.735	**0.013***	0.618(0.037)	0.627(0.041)	0.462	**0.018***
5 mm circle	261.75 (80.67)	251.22 (69.11)	0.812	**0.011***	0.618(0.024)	0.625(0.029)	0.521	**0.002****
Inner rim	257.42 (77.80)	246.99 (67.21)	0.812	**0.010****	0.618(0.024)	0.625(0.029)	0.597	**0.004****
11 mm circle	235.33(60.70)	229.47(59.07)	0.918	**0.007****	0.607(0.020)	0.610(0.025)	0.520	0.079
Outer rim	226.57(54.83)	222.32(56.27)	0.919	**0.035***	0.603(0.021)	0.605(0.025)	0.598	0.311
12 × 12	227.26(54.41)	221.62(53.89)	0.918	**0.004****	0.609(0.019)	0.612(0.024)	0.599	0.091

*, $P < 0.05$; **, $P < 0.01$.

Signed and absolute interocular differences in MCT and CVI measurements are summarized in Tables 3.3 and 3.4. The normal 95% limits of signed differences and absolute differences in MCT and CVI measurements could be used as a reference for physiological asymmetry. For example, if the MCT of the left eye is more than 77.75 um thicker than the MCT of the right eye, or the MCT of the right eye is more than 125.71 um thicker than the MCT of the left eyes in the 5 mm circle region, then this patient's interocular difference is thought to be abnormal. Alternatively, if the absolute interocular MCT difference is greater than 104.25 um in the 5 mm circle region, then this patient's eyes are also considered abnormal. In addition, the box plots of signed interocular differences in MCT and CVI measurements are shown in Fig 3.4 and 3.5, respectively. Fig 3.4 shows trends for right eyes to have thicker MCTs than left eyes in all the regions. Comparatively, Fig 3.5 shows trends for right eyes to have lower CVIs in all the regions. Although a weak inverse relationship between signed interocular differences of MCT and signed interocular differences of CVI was observed in the 2.5-mm circle (Pearson's r = -0.21, $P = 0.020$), the strength of the relationship was too weak to consider noteworthy (Table 3.5). Therefore, neither signed nor absolute interocular differences in MCT were correlated with corresponding CVI interocular differences in all the regions quantified (Table 3.5 and Fig 3.6).

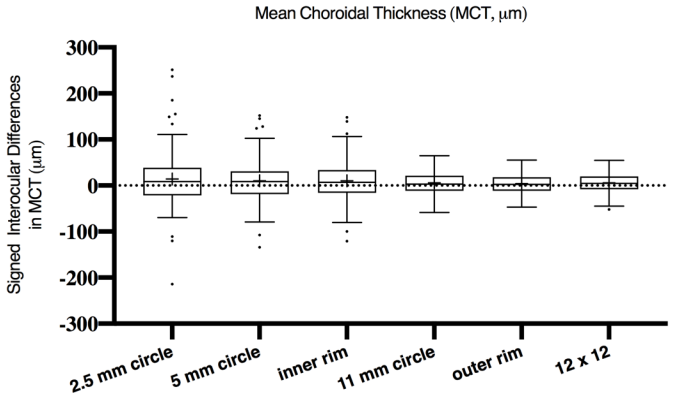

Fig 3.4 Tukey boxplots of the signed interocular difference of MCT from all 122 participants.
Boxplots show the mean as "+". The perforated line indicates the zero. Trends for right eyes have thicker MCTs (the mean value larger than 0) shown in the 2.5 mm circle, 5 mm circle, inner rim, 11 mm circle, outer rim and entire 12x12 mm scan regions.

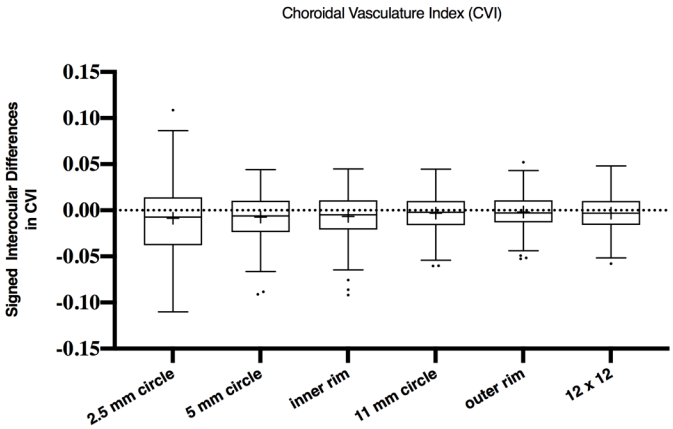

Fig 3.5 Tukey boxplots of the signed interocular difference of CVI from all 122 participants.
Boxplots show the mean as "+". The perforated line indicates the zero. A trend for right eyes to have lower CVIs (the mean value less than 0) shown in the 2.5 mm circle, 5 mm circle, inner rim, 11 mm circle, outer rim and entire 12 ×12 mm scan regions.

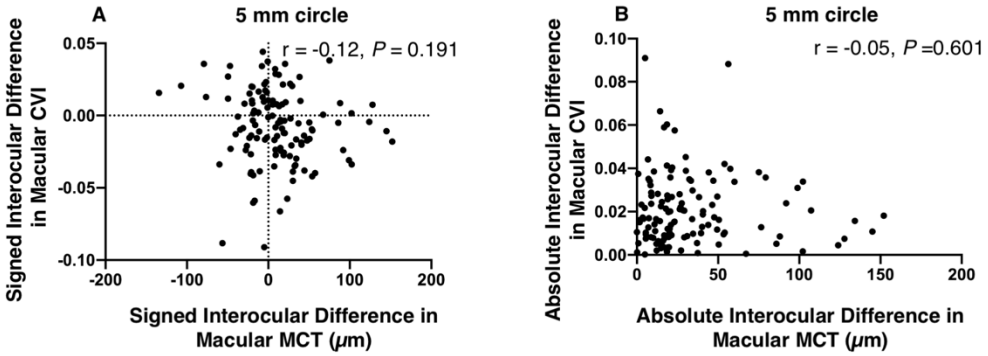

Fig 3.6 Scatter plots showing relationships between interocular differences in MCT and CVI in the 5 mm circle (macular) region.

(**A**) The relationship between signed interocular differences in MCT and CVI in the 5 mm circle region. (**B**) The relationship between absolute interocular differences in MCT and CVI in the 5 mm circle region.

Table 3.3 Signed and absolute interocular differences in mean choroidal thickness (MCT)

Region Quantified	Signed Interocular Differences (Right Eye - Left Eye, μm)		Size of signed interocular differences (the average signed interocular differences as a percentage of the MCT, %)	Absolute Interocular Differences(μm)		
	Mean (SD)	Normal 95% limits (2.5% title — 97.5% title)		Mean (SD)	Median (Min, Max)	Normal 95% limits (95% tile)
2.5 mm circle	14.06 (61.52)	-88.43 — 168.63	5.26	42.81 (46.22)	30.60 (1.55, 251.41)	139.89
5 mm circle	10.53 (45.21)	-77.75 — 125.71	4.11	33.17 (32.34)	20.99 (0.07, 152.04)	104.25
Inner rim	10.42 (43.74)	-77.78 — 109.08	4.13	32.33 (31.13)	19.64 (0.27, 148.08)	102.04
11 mm circle	5.86 (23.63)	-41.07 — 54.54	2.52	18.82 (15.36)	14.43 (0.08, 64.62)	52.33
Outer rim	4.25 (22.00)	-33.90 — 51.94	1.89	17.36 (14.09)	12.03 (0.34, 55.27)	47.65
12 x 12	5.64 (21.31)	-36.02 — 46.38	2.51	17.42 (13.42)	14.69 (0.21, 54.53)	44.48

Table 3.4 Signed and absolute interocular differences in choroidal vascularity index (CVI)

Region Quantified	Relative Interocular Differences (Right Eye - Left Eye)		Size of Signed Interocular Differences (the average signed interocular difference as a percentage of the average CVI, %)	Absolute Interocular Differences		
	Mean (SD)	Normal 95% limits (2.5% title — 97.5% title)		Mean (SD)	Median (Min, Max)	Normal 95% limits (95% tile)
2.5 mm circle	-0.0087(0.040)	-0.088 — 0.071	-1.40	0.0323(0.0249)	0.0315(0.0001.0.1100)	0.074
5 mm circle	-0.0074(0.0257)	-0.063 — 0.037	-1.19	0.0210(0.0166)	0.0168(0.0002,0.0910)	0.050
Inner rim	-0.0067(0.0256)	-0.070 — 0.034	-1.08	0.0199(0.0173)	0.0159(0.0001, 0.0919)	0.051
11 mm circle	-0.0032(0.0201)	-0.046 — 0.035	-0.53	0.0158(0.0128)	0.0141(0.0001.0.0604)	0.038
Outer rim	-0.0019(0.0207)	-0.046 — 0.040	-0.32	0.0162(0.0130)	0.0119(0.0003, 0.0527)	0.042
12 × 12	-0.0030(0.0196)	-0.044 — 0.036	-0.49	0.0155(0.0122)	0.0131(0.0003,0.0579)	0.039

Table 3.5 Correlation coefficients between mean choroidal thickness (MCT) and choroidal vascularity index (CVI) in interocular differences

Region Quantified	Correlation between MCT and CVI in Signed Interocular Differences (Right Eye - Left Eye)		Correlation between MCT and CVI in Absolute Interocular Differences	
	Coefficients	*P* - value	Coefficients	*P* - value
2.5 mm circle	-0.21	0.020	0.01	0.883
5 mm circle	-0.12	0.191	-0.05	0.601
Inner rim	-0.07	0.457	-0.09	0.322
11 mm circle	-0.09	0.349	-0.06	0.531
Outer rim	-0.01	0.878	0.007	0.937
12 × 12	-0.08	0.369	-0.004	0.967

3.1.3.2 Factors influencing interocular differences in MCT and CVI measurements

The relationship between interocular differences and clinical factors such as age and axial length are shown in Tables 3.6 and 3.7 and Fig 3.7 and 3.8. Neither the signed nor absolute interocular differences of MCT were significantly related to age or the respective interocular differences in the axial length. Despite a handful of statistically significant correlations between signed interocular difference of CVI and age, none rose to the level of being clinically significant. Therefore, like MCT, the signed or absolute interocular differences of CVI were not significantly related to age or the interocular differences in the axial length.

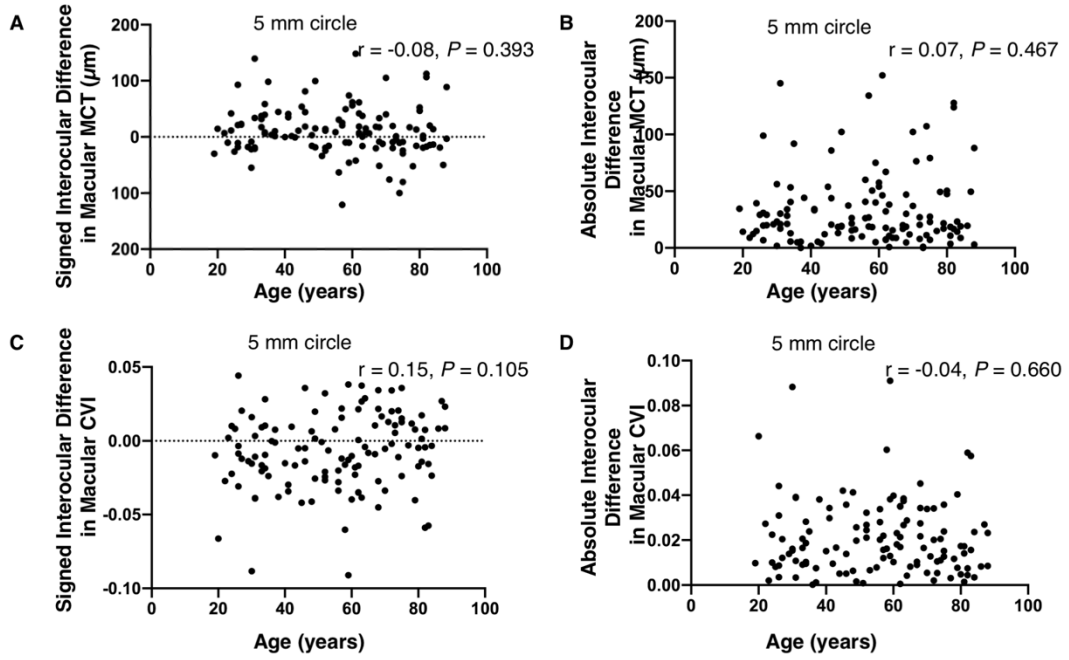

Fig 3.7 Scatterplots showing relationships between interocular difference in the 5 mm circle (macular) region and age. (**A**) The relationship between the signed interocular difference in mean choroidal thickness (MCT) and age. (**B**) The relationship between the absolute interocular difference in MCT and age. (**C**) The relationship between the signed interocular difference in choroidal vascularity index (CVI) measurements and age. (**D**) The relationship between the absolute interocular difference in CVI and age.

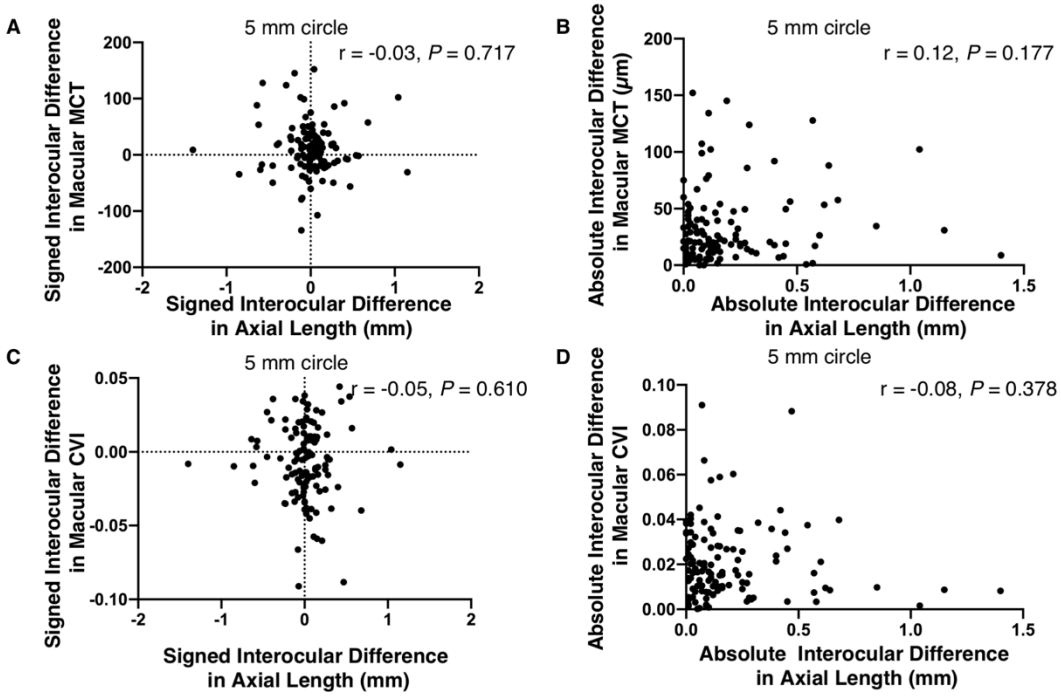

Fig 3.8 Scatterplots showing relationships between interocular difference in the 5 mm circle (macular) region and axial length. (A) The relationship between the signed interocular difference in mean choroidal thickness (MCT) and axial length. (B) The relationship between the absolute interocular difference in MCT and axial length. (C) The relationship between the signed interocular difference in choroidal vascularity index (CVI) measurements and axial length. (D) The relationship between the absolute interocular difference in CVI measurements and axial length.

Table 3.6 Assessment of age influencing interocular differences in mean choroidal thickness (MCT) and choroidal vascularity (CVI) (correlation coefficients, P values)

Measurement	Region Quantified	Signed Differences	Absolute value Differences
Mean Choroidal Thickness (MCT)	**2.5 mm circle**	r = -0.08, *P* = 0.375	r = -0.01, *P* = 0.922
	5 mm circle	r = -0.08, *P* = 0.393	r = 0.07, *P* = 0.467
	Inner rim	r = -0.10, *P* = 0.297	r = 0.07, *P* = 0.472
	11 mm circle	r = 0.01, *P*= 0.945	r = 0.16, *P* = 0.070
	Outer rim	r = 0.07, *P* = 0.428	r = 0.14, *P* = 0.114
	12x12	r = 0.003, *P* = 0.972	**r = 0.18, *P* = 0.046***
Choroidal Vascularity Index (CVI)	**2.5 mm circle**	r = 0.14, *P* = 0.116	r = 0.01, *P* = 0.919
	5 mm circle	r = 0.15, *P* = 0.105	r = -0.04, *P* = 0.660
	Inner rim	r = 0.12, *P* = 0.204	r = -0.04, *P* = 0.648
	11 mm circle	**r = 0.19, *P* = 0.037***	r = -0.10, *P* = 0.252
	Outer rim	**r = 0.20, *P* = 0.030***	r = -0.09, *P* = 0.318
	12x12	**r = 0.19, *P* = 0.035***	r = -0.16, *P* = 0.084

All values with signed interocular differences were calculated by subtracting the left eye values from the right eye values.
*, $P < 0.05$

Table 3.7 Assessment of interocular differences in axial length influencing interocular differences in mean choroidal thickness (MCT) and choroidal vascularity (CVI) (correlation coefficients, P values)

Measurement	Region Quantified	Signed Differences	Absolute value Differences
Mean Choroidal Thickness (MCT)	2.5 mm circle	r = -0.04, *P* = 0.628	r = 0.13, *P* = 0.154
	5 mm circle	r = -0.03, *P* = 0.717	r = 0.12, *P* = 0.177
	Inner rim	r = -0.03, *P* = 0.780	r = 0.11, *P* = 0.234
	11 mm circle	r = 0.02, *P*= 0.791	r = 0.16, *P* = 0.080
	Outer rim	r = 0.05, *P* = 0.595	r = 0.12, *P* = 0.179
	12x12	r = 0.01, *P* = 0.893	r = 0.16, *P* = 0.080
Choroidal Vascularity Index (CVI)	2.5 mm circle	r = -0.04, *P* = 0.633	r = -0.03, *P* = 0.742
	5 mm circle	r = -0.05, *P* = 0.610	r = -0.08, *P* = 0.378
	Inner rim	r = -0.03, *P* = 0.705	r = -0.002, *P* = 0.979
	11 mm circle	r = -0.14, *P* = 0.116	r = -0.0002, *P* = 0.999
	Outer rim	r = -0.15, *P* = 0.091	r = 0.06, *P* = 0.512
	12x12	r = -0.12, *P* = 0.171	r = 0.01, *P* = 0.871

All values with signed interocular differences were calculated by subtracting the left eye values from the right eye values.

3.1.4 Discussion

Choroidal diseases can be unilateral, bilateral, or present unilaterally at first, but then progress bilaterally, such as tumors (107), age-related macular degeneration (AMD) (108,109), and polypoidal choroidal vasculopathy (PCV) (110,111). In eyes that appear normal, the appearance of bilateral differences in choroidal measurements between fellow eyes that exceed the range of physiological asymmetry may be the first clue of an evolving pathological process that warrants further examination and follow-up. Therefore, establishing baseline choroidal asymmetry between fellow eyes in the normal population may be of clinical benefit, especially when monitoring for the onset of diseases that tend to affect both eyes.

As expected, our study demonstrated strong correlation of MCT measurements between the right and left eyes in all the regions in this normal population (Table 3.2 and Fig 3.3), which is consistent with previous studies (99,101,112,113). Despite a strong correlation of the choroidal thickness between fellow eyes, comparison analysis revealed that choroidal thickness in some macular subregions in right eyes tended to be thicker than that in left eyes in normal eyes (98,100,101,113,114). However, two prior studies reported an opposite result, that is, the subfoveal choroidal thickness of the right eyes was thinner compared to the left eyes (99,112). It is worth noting that the results of these prior studies were all derived from manual

measurements of selected B-scans, therefore, the subjective bias of the choroidal thickness measurements might lead to discrepancies among studies. Here we showed a significantly thicker MCT in right eyes than in left eyes in all the regions (Table 3.2 and Fig 3.4). It is suspected that the interocular choroidal asymmetry of MCT might be attributed to asymmetrical choroidal blood flow. One possible explanation of this is the anatomical asymmetry of the aortic arch and common carotid arteries. It is known that the right common carotid originates from the neck from the brachiocephalic trunk, while the left originates in the thorax from the aorta (115), and the choroidal vasculature is supplied by the long and short posterior ciliary and the anterior ciliary arteries (116), all of which are the distal branches of the ophthalmic artery, which arises from the internal carotid artery. The asymmetry of the common carotid arteries, along with variations in vessel curvature, result in hemodynamic differences that may cause observable interocular differences in MCT (115,117). Anatomical asymmetries in non-pathologic choroidal venous drainage (118,119) and autonomic and sensory neural innervation (120) may also precipitate variations in MCT measurements resulting from differences in the choroidal circulation. The vasculature is complicated further by the presence of collateral blood flow from the external carotid arteries (121,122). One future strategy to investigate the asymmetries in choroidal blood flow resulting from interocular variations in anatomic vasculature or neural innervation would be to visualize facial blood flow in relation to asymmetrical choroidal thickness (123). Another possibility is that MCT asymmetry between eyes may be due to eye preference. Previous studies have shown that approximately 70% of the population are right-eye dominant (124,125), and differences linked with eye dominance such as accommodation have been tied to changes in choroidal thickness (126,127). To explore this possibility, we propose that future studies designed to study these interocular choroidal differences will need to document the dominant eye for each subject.

The interocular symmetry in CVI has not been previously studied in detail. We found that unlike a strong interocular correlation in MCT, there was only a moderate interocular correlation in CVI within all corresponding regions (Table 3.2). Our study showed a significantly smaller CVI in the right eyes compared with the left eyes within the central regions (2.5-mm circle, 5-mm circle, 5-mm rim). However, it is worth noting that the size of signed interocular differences in CVI, being only ~ 0.32% to 1.40% (Table 3.4 and Fig 3.5), was very small, therefore, the difference in CVI measurements between fellow eyes is not likely to be clinically significant in normal eyes. In addition, compared with previous methods for measuring CVI on two-dimensional images (i.e., B-scan or *en face* images), our method of calculating CVI was performed on the entire volumetric scan, which is thought to be more relevant and reasonable.

In the correlation analysis (Table 1.5 and Fig 1.6), neither signed nor absolute interocular differences in MCT were correlated with corresponding CVI interocular differences, which suggests that any mechanism

explaining MCT asymmetry may not be what drives the CVI asymmetry. In addition, we did not find any significant correlation between the interocular differences (including both signed and absolute differences) in MCT and CVI measurements and the age of the participants (Table 3.6), indicating that age-specific normal ranges for MCT and CVI symmetry measurements are not necessary. Although Chen *et al* (113) reported a marginally significant trend ($r = -0.20$, $P = 0.048$) for reduced absolute differences in foveal choroidal thickness with the increase of age, the degree of the relationship did not rise to the level of being clinically significant. Signed interocular MCT differences also showed no relationship with signed interocular axial length differences (Fig 3.8), which was inconsistent with the result reported by Kim *et al* (101) in which the interocular choroidal thickness and axial length differences had a significant negative correlation. This may be due to the differences in the measurement methods used and the distribution of participants' age between these two studies, as well as the exclusion of participants with axial lengths greater than 26-mm axial length in our study.

While promising, there were some notable limitations in this study. Firstly, we did not acquire other information (e.g., dominant eye, interocular pressure, visual acuity, and refraction errors) that may influence interocular choroidal symmetry. While we excluded eyes with pathological myopia, myopia has been correlated with increased interocular differences in choroidal thickness with thinning of choroid in the more myopic eye. Characterizing atypical MCT in cases of asymmetric myopia would further refine a clinical baseline for physiologic asymmetries in MCT, as well as pathologies linked to eyes with greater degrees of myopia (128). However, given that our intention was primarily to assess the physiological choroidal asymmetry in MCT and CVI within normal eyes, this limitation was not thought to diminish the validity of this study. Secondly, our study was a cross-sectional study and only involved one time point, which may result in inclusion of participants whose ocular diseases were at a very early stage and did not meet clinical diagnostic criteria. This is a common limitation for all current studies investigating interocular asymmetry of the choroid in normal eyes . Future studies will need to recruit more participants and carry out multiple clinical examinations and SS-OCT imaging sessions to distinguish participants who currently appear "normal" but later develop ocular diseases, such as AMD.

To the best of our knowledge, we are unaware of any report using widefield SS-OCT imaging to investigate choroidal symmetry between fellow normal eyes. Our study has successfully demonstrated subtle differences in MCT and CVI measurements between fellow normal eyes using SS-OCT and established 95% normal limits for these measurements between eyes. This study will be useful clinically in assisting clinicians and researchers in distinguishing pathological eyes from eyes that are within the tolerance limits for physiological asymmetry.

3.2 Assessing Age-related Macular Degeneration (AMD) Progression through Automated Segmentation of the Outer Retinal Layer

3.2.1 Purposes

The aim of this study is to investigate whether the outer retinal layer (ORL) thickness could serve as an independent biomarker for predicting the progression of AMD, we examined the variations in ORL thickness among different groups, including normal, reticular pseudodrusen only (intermediate AMD), soft drusen (intermediate AMD), and geographic atrophy groups (late AMD).

3.2.2 Method

The clinical data utilized in this section were identical to those in Section 2.4.2.

3.2.2.1 Drusen volume and geographic atrophy areas measurements

The measurements of drusen volume were obtained using the Advanced RPE Analysis Algorithm version 0.10, a validated algorithm available on the Advanced Retinal Imaging Network website (Carl Zeiss Meditec, Inc) (130).

The GA areas were measured from the OCT Sub-RPE image obtained from a slab defined by boundaries from 64 to 400 μm under BM. The details of the process have been described in our previous study (57).

Drusen volume and GA areas were specifically measured in the 3-mm and 5-mm circles centered at the fovea.

3.2.2.2 Statistical Analysis

Statistical analysis was carried out using Matlab2021b and GraphPad Prism (GraphPad Software, San Diego, CA). Pearson's correlation was used to compare the ORL thickness measurements from SS-OCT and SD-OCT, and Bland Altman plots were used to analyze the agreement between the ORL thickness measurements from SS-OCT and SD-OCT. One-way analysis of variance (ANOVA) and Tukey–Kramer post-hoc tests were used to compare ORL thickness differences between normal, reticular pseudodrusen, drusen and GA groups. Furthermore, the correlation between ORL thickness and drusen volume in the drusen group and the correlation between ORL thickness and GA areas in the GA group were studied by

Pearson's correlation. Statistical significance is graphically represented at four levels: *P ≤ 0.05, **P ≤ 0.01, ***P ≤ 0.001, and ****P ≤ 0.0001.

3.2.3 Results

To investigate the ORL thickness changes in intermediate and late stages of AMD, a total of 199 eyes were measured and analyzed. Among these 199 eyes, there were 80 normal eyes, 30 reticular pseudodrusen only eyes, 49 drusen only eyes, and 40 GA eyes. The characteristics of these four groups were summarized in Table 3.8. The four groups were age matched (ANOVA P = 0.1087), with the mean age being 72.5 ± 8.0 years in the normal group, 73.6 ± 8.2 years in the reticular pseudodrusen group, 76.0 ± 8.0 years in the soft drusen group, and 74.1 ± 8.7 in the GA group. Fig. 3.9 shows representative examples of each group. Notably, these four eyes were not included in the training dataset. Figs.3.9 A-D show the ORL thickness map and Figs. 3.9 E-H show the corresponding B-scan. A homogeneously distributed colors can be seen in ORL thickness map of the normal eye (Fig. 3.9 A and E). Comparatively, the ORL thickness map of the reticular pseudodrusen shows globally thinner (Fig. 3.9 B and F). For the drusen eye (Fig. 3.9 C and G), the ORL thickness map appears thinner, particularly in the drusen lesion, compared with the normal eye. The ORL thickness map of the GA eye present significantly thinner than other three groups (Fig. 3.9 D and H).

Table 3.8 Characteristics of all the eyes imaged with SS-OCT included in this study.

Characteristics	**Normal (n=80)**	**RPD (n=30)**	**Drusen (n=49)**	**hyperTDs (n=40)**	**P Value**
Age, year, mean (SD)	72.5(8.0)	73.6(8.2)	76.0(8.0)	74.1(8.7)	0.1087
3mm-circle ORL thickness, μm, mean (SD)	178.1(9.4)	167.7(8.6)	156.3(8.9)	141.3(16.3)	<0.0001
5mm-circle ORL thickness, μm, mean (SD)	163.1(8.7)	156.0(7.4)	148.7(5.5)	138.3(11.3)	<0.0001

Abbreviations: SD – standard deviation. ORL – outer retinal layer. RPD – reticular pseudodrusen. hyperTDs – hypertransmission defects.

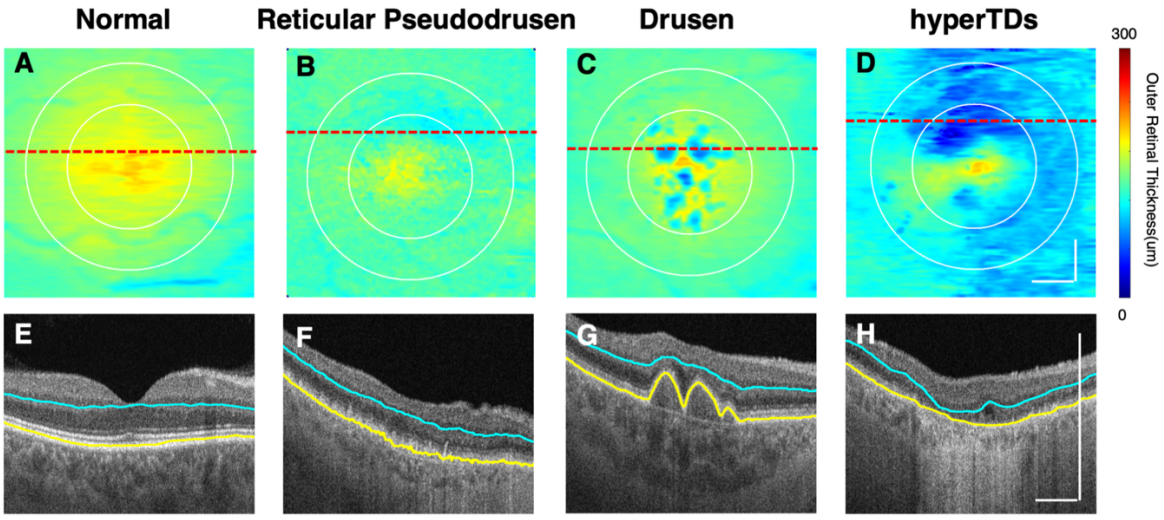

Fig 3.9. Representative segmentation results of outer retinal layer (ORL) taken from a normal eye (A and E), a reticular pseudodrusen eye (B and F), a soft drusen eye (C and G), and a geographic atrophy (GA) eye (D and H). (A-D) ORL thickness maps. (E-H) OCT B-scans with their locations shown as dashed lines in (A-D), with blue lines indicating the inner boundary of OPL and yellow lines indicating the RPE/BM location. Blue lines and yellow lines were derived from the automatic segmentations. White circles indicate 3 mm and 5 mm diameter circles centered on the fovea. Scale bar represents 1mm.

Shown in Fig. 3.9 and Table 3.8 are the quantitative ORL thickness measurements representing all eyes in the 3-mm circle and 5-mm circle centered on the fovea. When comparing the average ORL thickness of each group with the average of every other group, it was observed that the normal group presented the largest mean value, followed by the reticular pseudodrusen group, the drusen group with the third largest mean value, and finally, the GA group with the lowest mean value. These findings highlight significant differences between the groups in terms of ORL thickness (all $P < 0.0001$) in both the 3-mm circle and 5-mm circle centered on the fovea.

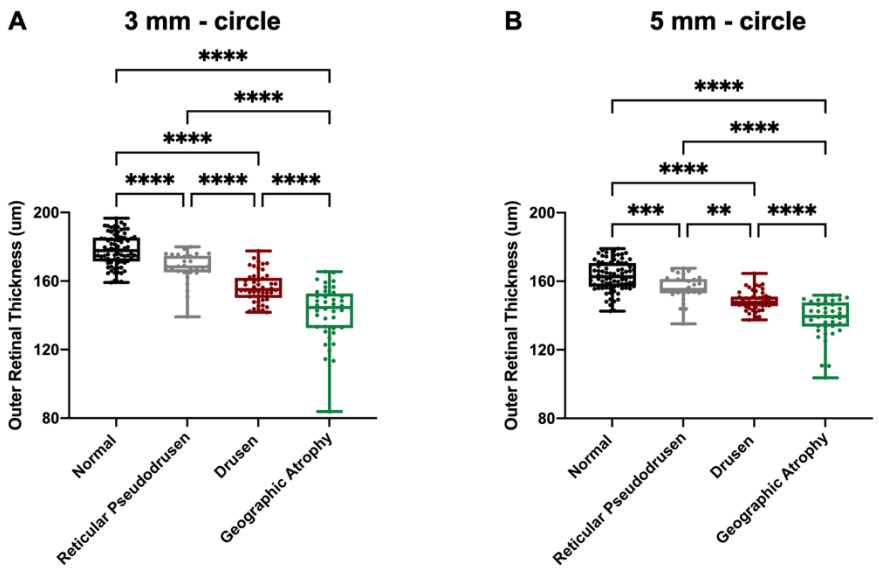

Fig 3.10 Graphic representation of outer retinal layer (ORL) thickness measurements.
Comparison of ORL thickness among the normal, reticular pseudodrusen, drusen, and geographic atrophy on the 3 mm-circle (A) and 5 mm-circle (B) centered on the fovea, respectively. ** represents $P \leq 0.01$, *** represents $P \leq 0.001$, and **** represents $P \leq 0.0001$. Boxplots show interquartile range, whiskers minimum to maximum, and all points.

Figure 3.11 shows the correlation between the thickness of ORL and the volume of drusen in the drusen group. This figure consists of four components: (A) a drusen map displaying color-coded distances between the RPE and BM, (B) a corresponding map showing the thickness of the ORL, and scatter plots of all eyes in the drusen group within the 3 mm-circle (C) and the 5 mm-circle (D) centered on the fovea. In this particular case, most drusen lesions were located within the 3 mm-circle (Fig 3.11 A), and the ORL thickness showed an inverse pattern compared to the drusen map. In other words, areas with thinner ORL thickness appeared to correspond to regions with a thicker RPE-BM distance. Notably, a significant negative correlation between drusen volume and ORL thickness was observed within the 3 mm-circle ($r = -0.4616$, $P = 0.0008$), whereas no significant correlation was found within the 5 mm-circle ($r = -0.1175$, $P = 0.4215$).

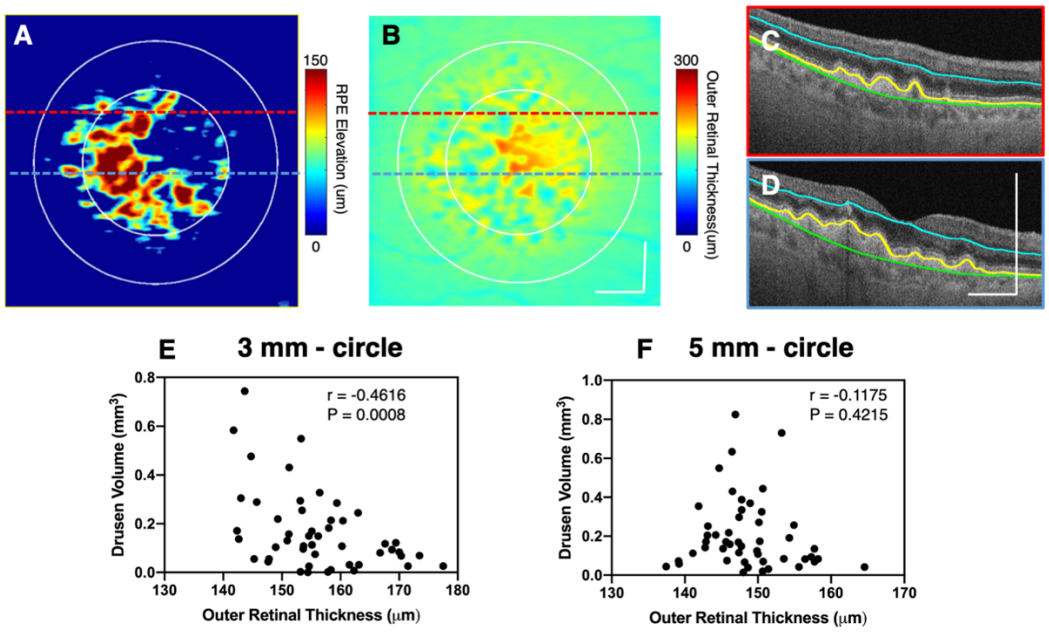

Fig 3.11. A representative example of a drusen eye along with the relationship between drusen volume and ORL thickness measurements in the drusen group:
(A) the drusen map by displaying the distances between yellow lines and green lines shown in (C and D) and (B) corresponding outer retinal layer (ORL) thickness map. (C and D) OCT B-scans with their locations shown as dashed lines in (A and B) where drusen can be identified. Blue outlines indicate the inner boundary of the outer plexiform layer, yellow outlines indicate the retinal pigment epithelium (RPE), and green outlines indicate Bruch's membrane. (E and F) Scatter plots showing the relationship between drusen volume and ORL thickness measurements in the drusen group for the 3 mm-circle and 5 mm-circle centered on the fovea, respectively. White circles indicate 3 mm and 5 mm diameter circles centered on the fovea.

Figure 3.12 shows the correlation between the ORL thickness measurements and the GA area measurements in the GA group. This figure consists of four components: (A) a Sub-RPE image with the yellow outlines highlighting the geographic atrophy (GA) areas, (B) a corresponding map showing the thickness of the ORL, and scatter plots of all eyes in the GA group within the 3 mm-circle (C) and the 5 mm-circle (D) centered on the fovea. It appeared that GA regions had a thinner ORL thickness than surrounding normal regions. A strong negative correlation between GA areas and ORL thickness was observed both within the 3 mm-circle ($r = -0.8333$, $P < 0.0001$) and the 5 mm-circle ($r = -0.7630$, $P < 0.0001$).

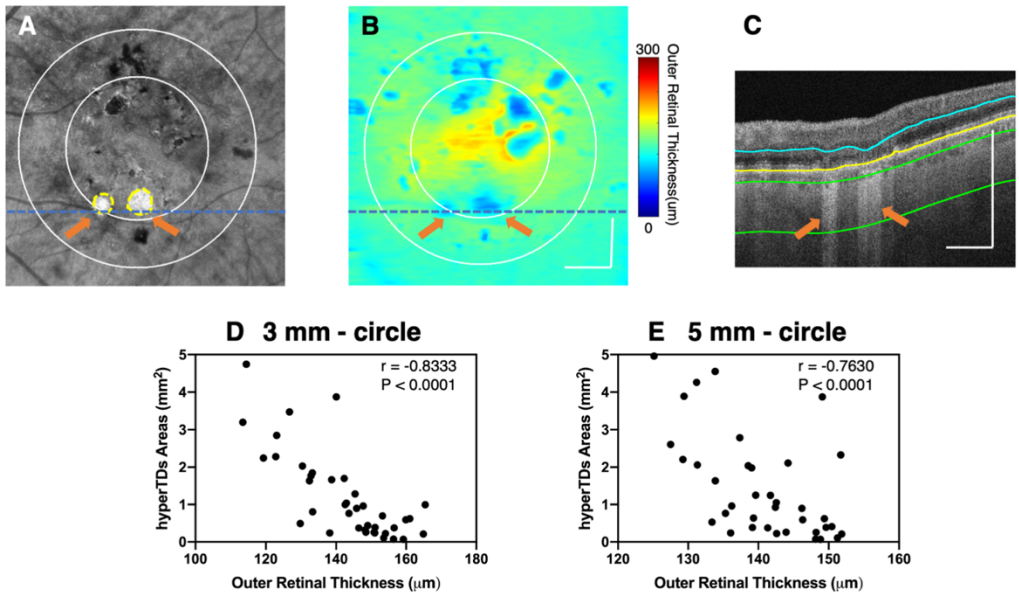

Fig 3.12 A representative example of an eye with persistent choroidal hypertransmission defects (hyperTDs) along with relationship between hyperTD area measurements and ORL thickness measurements in the persistent hyperTD group: (A) OCT En face Sub-RPE image obtained from a slab defined from 64 um to 400 um below the Bruch's membrane (BM) shown with green lines in (C), with the yellow outlines highlighting the GA areas and (B) corresponding outer retinal layer (ORL) thickness map. (C) OCT B-scan with its location shown as the dashed line in (A and B) where hyperTDs can be identified. Orange arrows indicate the hyperTDs that are used clinically to identify atrophic areas. Blue outlines indicate the inner boundary of the outer plexiform layer and yellow outlines indicate the retinal pigment epithelium (RPE) or Bruch's membrane where RPE is absent. (D and E) Scatter plots showing the relationship between hyperTD area measurements and ORL thickness measurements in the persistent hyperTD group in the 3 mm-circle and 5 mm-circle centered on the fovea, respectively. White circles indicate 3 mm and 5 mm diameter fovea-centered circles.

3.2.4 Discussion

The comparative analysis revealed significant differences in ORL thickness among the normal, soft drusen (intermediate AMD), reticular pseudodrusen (intermediate AMD), and geographic atrophy (late AMD) groups (Table 3.8 and Fig. 3.9), consistent with previous studies demonstrating that intermediate AMD had thinner ORL compared to normal controls (131–133). It is worth noting that Ooto Sotaro et al. (134) reported no age -related changes in ORL thickness, while Sruthi Arepalli et al. (135) found an increase in ORL thickness with age in the normal group. These findings suggest that the reduced ORL thickness observed in our study is unlikely to be attributed to aging, especially considering the age matches among each group in our study. Therefore, it is highly likely that the observed reduction in ORL thickness is a result of pathological changes, indicating that ORL thickness could serve as a potential independent biomarker for predicting the progression of AMD. These findings provide valuable insights into the structural alterations associated with different stages of AMD.

Drusen volume, known to be a predictor of diseases progression of late AMD (9,136), showed a negative correlation with ORL thickness in the 3-mm circle centered on the fovea ($r = -0.4616$, $P = 0.0008$, Fig. 3.11). However, there was no significant correlation between drusen volume and ORL thickness in the 5-mm circle. It might be attributed to the influence of drusen volume on the measurements of ORL thickness, particularly considering that the majority of drusen lesions were concentrated in the 3-mm circle in all the 49 drusen cases, as shown in Fig. 3.11A. Moreover, this phenomenon may explain the significant difference in ORL thickness between the drusen and reticular pseudodrusen groups shown in Fig. 3.10. In this study, the mean drusen volume within the fovea-centered 5 mm circle was 0.207 ± 0.185 mm^3 in the soft drusen group, whereas only 0.01 ± 0.02 mm^3 in the reticular pseudodrusen group. Consequently, the ORL thickness in the drusen eyes are affected not only by drusen volume but also by outer retinal atrophy, while reticular pseudodrusen eyes are primarily impacted by outer retinal atrophy (132,133). In conclusion, ORL thickness could serve as a more sensitive biomarker for evaluating the progression of AMD than drusen volume, as it encompasses changes from both drusen volume and the outer retina atrophy.

Strong correlations were observed between GA areas and ORL thickness in both the 3-mm and 5-mm circles ($r = -0.8333$, $P < 0.0001$ in the 3-mm circle; $r = -0.7630$, $P < 0.0001$ in the 5-mm circle; shown in Fig. 3.12). This correlation can be attributed to the significantly thinner ORL thickness in the GA regions compared to the surrounding areas (137), shown in Fig. 3.9 D and H. These findings highlight the potential of ORL thickness as a biomarker for assessing the severity of GA.

Although promising, it should be noted that there are several limitations within our study. First, the training dataset used in this study was obtained from Carl Zeiss, which raises uncertainties regarding the applicability of the algorithm to data from other commercial devices. Nevertheless, although some bias may arise when applying the algorithm to datasets from different device types, we believe our algorithm can still assist in annotating ORL segmentation. Secondly, the lack of follow-up visits for the AMD groups hinders a comprehensive understanding of the impact of ORL thickness on AMD progression. To address this, our future study will incorporate multiple follow-up visits, enabling a comparison of ORL differences between eyes that progress to late AMD and those that do not, thus enhancing our knowledge of the mechanism and evolution of AMD. Lastly, this study did not measure biomarkers associated with AMD, including choroid capillary flow deficit, calcified drusen, and hyperreflective foci. We intend to investigate these biomarkers in the near future to validate the changes in ORL thickness.

The comparative analysis revealed significant differences in ORL thickness among different AMD stages, indicating its potential as an independent biomarker for predicting AMD progression.

4 Chapter 4. Clinical application of OCT in burn-damaged skin

While OCT has proven to be a game-changer in ophthalmology, its capabilities extend beyond eye health. In this Chapter, we discuss the clinical applications of OCT for dermatology. Firstly, we integrate pressure sensors with a handheld probe to facilitate imaging of micro vasculature, addressing the challenge of uncontrollable mechanical stress during contact mode imaging of the skin. This handheld scanning probe with built-in pressure sensors provides real-time feedback to control the mechanical stress, enabling repeatable and reliable OCTA images for a more accurate investigation of skin conditions. Secondly, we employ a clinical-prototype OCT system to image severe burn wounds at multiple scan sites across two time points. Quantitative analysis of vascular area density and surface roughness offers key insights into the pathophysiological mechanisms responsible for wound healing, potentially serving as critical biological indicators in future clinical evaluation and monitoring of wound healing. Lastly, we demonstrate the potential of OCT alongside OCTA to non-invasively image and monitor human skin graft health and integration over time, providing valuable insights for wound healing monitoring after skin graft surgery.

4.1 Integrating pressure sensor with OCT handheld probe to facilitate imaging of microvascular information in skin.

4.1.1 Introduction

OCT and OCTA have now been translated to clinical ophthalmology (3,4), dentistry (138), neuroscience (139), and becomes more and more popular in dermatology (140). Despite its attractiveness, there are several inherent issues in OCT/OCTA skin imaging acquisitions: a) unavoidable tissue motion; b) skin natural curve that leads to a difficulty to keep targeted region of interest within system available ranging distance; c) high scattering or specular reflection from the skin surface that can shadow the tissue information at deeper layers.

Previous studies have shown that a topical application of optical clearing agents (OCA), such as glycerin and ultrasound gel, can efficiently reduce scattering effect, thereby enhancing the light penetration depth and improving the imaging contrast (141,142). Additionally, an OCT adapter cap with a glass window has been used to cover the scanning region during imaging acquisition to reduce the motion relative to the OCT probe, mitigate the skin natural curvature and suppress high backscattering from the skin surface (34,143,144). While this approach demonstrated reasonable successes, the drawback is that the uncontrolled mechanical stress exerted on the skin inevitably impacts the skin optical property and blood perfusion, thereby affecting the OCT/OCTA imaging to a unknown degree (145). Therefore, it is critically important to monitor and control the force or mechanical stress applied on the skin surface during OCT imaging when

a glass window is used in the procedure. To achieve this, we aim to develop a built-in force sensor in an OCT handheld probe. For easy operation of the handheld probe, the built-in force sensor should be thin enough, sufficiently light, and provide real-time response.

Whilst there are many different force sensors available for use, we selected to use force-sensing resistors (FSR) in this study to be built into the OCT probe since they are compact, lightweight, cost-effective, and easily customizable (146). FSRs have been widely incorporated into numerous biomechanical applications (147,148). FSRs are composed of conductive polymers that exhibit a responsive relationship between resistance and mechanical force or pressure that is being applied (149). Using a microcontroller, the change in its resistance can be interpreted within 1ms, allowing the applied pressure to be resolved in real-time.

In this study, we report a handheld scanning probe with built-in force sensors, allowing the operator to assess and monitor the external forces (therefore the pressure) applied on the skin during OCT imaging procedure. To demonstrate the potentials of pressure sensors in OCT imaging acquisition, we investigated how the pressure variations on the skin would have an effect on OCTA imaging as well as the blood flow real-time response to an application and subsequent release of the external force exerted on the skin, i.e., the well-known skin hyperemia experiment.

4.1.2 Method

4.1.2.1 The considerations and design of pressure sensor with the OCT probe

The demand to measure the pressure exerted on the skin surface during OCTA imaging acquisition arises from the need for imaging repeatability and reliability, aiming for quantitative assessment of microvascular responses under either disease or stimulation conditions. Uncontrolled pressure due to the contact of the glass window of the OCT probe with the skin surface can complicate the interpretation of subsurface microvascular information. To measure the force or pressure exerted on the skin surface, the most straightforward approach is to sandwich a force sensor between the skin and the round-glass window, i.e., the sensor in direct contact with skin. This requires the sensor material to be optically transparent and not interfere with the OCT probe beam. However, we did not find such a commercial off-the-shelf sensor that meets this requirement. To avoid the interference of the sensor with the optical beam, we decided to place three small FSRs equidistantly at the periphery of the round-glass window to form a ring shape, leaving the middle region of the glass window transparent for the light transmission. This design would not only solve the concern about OCT light passing, but also could reflect whether the force applied to the skin is uniform based on the distribution of pressures sensed by the three FSRs.

Another consideration is the use of OCAs (e.g., glycerin and ultrasound gel) for the purpose of refractive index matching with the skin. If the sensors are in direct contact with skin, then the index matching gel

would make the sensors prone to contamination. Therefore, we opted for a design where the force sensor is placed between the glass window and the probe, rather than having the sensor in direct contact with the skin. This design is reasonable because the force introduced by the contact of the glass window with the skin surface is approximately equal to the force between the glass window and the probe during imaging. A schematic of such design by taking the considerations above is shown in Fig. 4.1. To improve the flexibility, the design is made detachable and snap-on format so that it is applicable to a variety of different OCT probes. Here, for the detachable attachment used in this study, it was customized to fit the LSM03 objective lens (Thorlabs Inc, USA) employed in the handheld probe of our OCT system.

The OCT system along with the handheld probe specially designed for skin imaging have been described in detail in our previous publications (34). Here, we introduce the detachable attachment in some detail in this section. The customized attachment was used to adjust the distance between the objective lens and the skin surface (144). We integrated the force sensors into this attachment. As shown in Figs. 4.1 A & 1B, the snap-on attachment consists of : 1) a round-glass window (BK7 glass, 20mm diameter, 1mm in thickness, Micro-Store) that is situated at the distal end of the attachment, and its outer face would be in direct contact with the skin surface during imaging; 2) a base holder that is right above the glass window and acts a support for the attachment; 3) three force sensors (FSR 402 with a diameter of 12.7mm, Interlink Electronics Inc.(150)) that are located at the outer face of the base holder and placed equidistantly with a ring shape with a diameter of 42 mm at the periphery region, leaving a clear window in the center (diameter 20 mm) for imaging (Fig.4.1 C); 4) three force concentrators made of a kind elastic rubber ensure that the force loads are concentrated within the sensing area of the FSR and minimize the shear effects from non-normal loads, allowing the contact force to be evenly distributed across the force sensors to optimize sensor linearity and repeatability; and 5) a cap adapter that provides a tight-fit to the scan lens. The base holder and cap adapter were 3D printed to fit the size. Figs. 4.1 B and C show detailed layout of the attachment. Each FSR is connected in series with a reference resistor in the circuit (Fig. 4.1 D) that converts the forces into electrical signals via an Arduino board (Arduino Uno, Arduino Store) that is fed into the proprietary OCT controlling software (in LabView platform) for real-time monitoring and display to aid the operator during imaging. The whole snap-on attachment is lightweight and compact (35 grams) and can be adapted for use in various OCT devices.

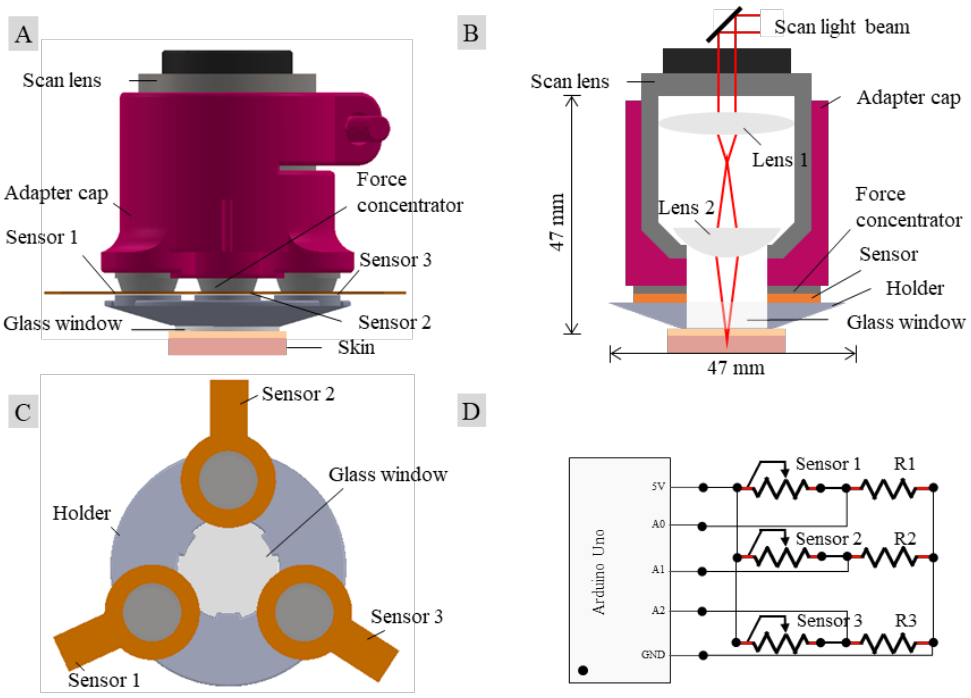

Fig 4.1 The design schematics of the detachable attachment integrated with force sensors.
(**A**) The overall design of the snap-on attachment that fits to the OCT probes. (**B**) The cross-sectional view of the design. (**C**) The perpendicular view at the level of the layout of three sensors, above the glass window, within the attachment. (**D**) Sensor resistance measurement and resistance-pressure conversion circuit, where R1 = R2 = R3 = 3.3kΩ.

4.1.2.2 Sensor calibration

The resistance of the FSR force sensor decreases with the increase of contact force exerted on the active area. Fig. 4.2 A shows an overview of its typical response behavior for the force range between 0 to 10000 grams (150). Considering the actual force applied to the skin which is relatively light, we chose the force range of interest between 100 and 1500 g (highlighted light-yellow in Fig. 4.2 A) for calibration. Over this range, the relationship between the force (in grams) and resistance follows a power law characteristics (150,151) with:

$$F = k \cdot \frac{1}{R^x}, \qquad (1)$$

where R is the measured resistance of force sensor when a force is applied on the active region, F represents the force (in grams), and k and x are calibration parameters that are dependent on the actual sensor characteristics. According to the circuit in Fig 4.2 D, the resistance of the sensor, R, can be obtained following the equation:

$$R = R_i \left(\frac{V_{CC}}{V_{Ai}} - 1\right). \qquad (2)$$

where Ri (i =1, 2, 3) represents the reference resistance, VCC is stimulation voltage, and VAi (i =1, 2, 3) is the measured voltage across the reference resistance.

The part-to-part variability of this type of pressure sensor is up to ± 25%, highlighted by the dark dashed lines in Fig. 4.2 A. To mitigate the variability, each sensor was individually calibrated by fitting the relationship between the sensed resistance and the applied forces using equation (1) to find the parameter k and x. To perform the calibration, we added reference forces, F, to the sensor sequentially and recorded the resistance, R, of the sensor accordingly. For each sensor, three independent measurements were repeated at each reference force, and the average was taken to minimize the noise-induced variations. The parameters k and x were then obtained by fitting the reference forces and corresponding measured resistances under the force to the Eq.1. After this calibration procedure, the sensors are ready to use in the OCT probe to provide real time readings of the pressure applied onto the skin surface.

OCT/OCTA Imaging and participants

After the snap-on attachment was fabricated in the lab and calibrated, we tested its utility in the OCT/OCTA imaging using an in-house-built swept-source OCT (SS-OCT) system. The system employed a 200 kHz swept laser source (SL1310V1-10048, Thorlabs Inc.) with a central wavelength of 1310 nm and a bandwidth of 100 nm, giving an axial resolution of ~7 μm (34). An LSM03 objective lens (Thorlabs Inc, USA) focused the light into a beam spot, giving a lateral resolution of ~25 μm. With the probe beam delivered to the sample at ~5mW, the system had a measured signal to noise ratio at ~100dB. An OCTA imaging protocol was used to obtain OCTA images from the scanned tissue volume, where we acquired four repeated B-frames at each B-frame location to produce one blood flow B-scan using an algorithm termed as optical microangiography (OMAG) (35). Each skin imaging volume covered a region of ~ 8 × 8 × 1.5 mm (~ 800 × 800 × 200 pixels) in the x (fast axis), y (slow axis) and z (penetration into the skin) directions, respectively.

To investigate the likely impacts on OCTA imaging with different levels of mechanical stresses, we acquired 3D OCT/OCTA imaging of skin in human subjects. Before OCT/OCTA imaging, cleaning and disinfection on the imaging area were performed and then a drop of index matching liquid (glycerin) was applied to the skin surface to reduce the specular reflection effect on the final results (142). Then, we sequentially increased the pressure applied to the skin, starting from no pressure to four strength levels (i.e., ~ 11, 17, 32, 69 kPa). When each strength level was stabilized, an OCT/OCTA image was captured. In order to test the repeatability of OCT/OCTA, we performed four sessions. Each session included five imaging points at different pressures (i.e., ~ 0, 11, 17, 32, 69 kPa) and a 15-minutes rest for a complete recovery of skin condition.

After obtaining OCT/OCTA data, we segmented each volume into three depth slabs measured from 245–392, 392–672, and 672–980 μm below the skin surface to compare the vascular response to external force stimulation at different depths. The tail-like artifacts from the strong forward scattering of erythrocytes would make vasculature at deep layers difficult to interpret, therefore, we utilized a previously published strategy to reduce such tailing artifacts (152). For the visualization and quantification purposes, maximum intensity projection (MIP) en face imaging of the OCTA volume was generated from each slab. The OCTA was analyzed by using vessel area density (VAD) (153) extracted from the MIP en face imaging to indicate the repeatability of OCTA using an algorithm clinically validated in numerous ophthalmology studies, e.g. in (154). The repeatability of OCTA imaging among different sessions was analyzed by using the intraclass correlation coefficient (ICC) (155).

Next, we investigated the utility of the proposed integrated probe on the well-known hyperemia experiment in skin. In a previous study on skin hyperemia (145), researchers induced force on the skin by manually adjusting the OCT probe but did not monitor or control the level of forces applied to the skin, resulting in inconsistent pressure being applied and incomplete pressure release, thereby increasing experiment bias and inevitable variations in the final results. This issue can be solved by using our proposed snap-on attachment that can provide the real-time information about the exact external force applied to the skin. While 3D OCTA scans can directly show the distribution of skin blood flow under different pressures, there remains an issue. That is, each 3D volume takes about 8 seconds, which would make it difficult to capture the peak hyperemia perfusion and recovery process after the release of mechanical stress. To mitigate this problem, we decided to use a repeated B-scan strategy, i.e. BM scan mode, instead of a 3D scan to demonstrate the reactive hyperemia features with pressure stimulation. To achieve that, with the OCT system running at 285 frames per second, 30,000 repeated B-frames were continuously collected at the same location over a period of ~105 seconds. Over this period, the pressure was applied to start at the 8th second and gradually up to 70kPa over ~10 seconds, then stayed relatively stable for ~20 seconds, and finally released at the 38th second. Like 3D OCTA data processing, four consecutive OCT B-frames were collapsed into one OCTA B-frames using the OMAG algorithm. In effect, each temporal dataset consisted of 7,500 OCTA B-frames with each B-frame consisting of 500 A-lines (covering ~8mm), allowing an OCTA imaging rate up to 71.25 frames per second. This imaging speed provides sufficient temporal resolution to observe blood volume response to applied pressure changes.

Three volunteers were participated in this study for OCT imaging. The use of OCT laboratory equipment on human subjects was approved by the Institutional Review Board (IRB) of University of Washington. This study followed the tenets of the Declaration of Helsinki and was conducted in compliance with the

Health Insurance Portability and Accountability Act. And written consent for imaging was obtained from each participant.

4.1.3 Results

4.1.3.1 Sensor Performance

The force sensors were calibrated individually according to the description in section 2.2 prior to assembling the attachment. Fig. 4.2 B shows the calibration results, where the dash lines show the fitting results for the FSRs resistance responses under the reference forces from 100 g to 1500 g using Eq. (1), with the three colors representing the three sensors used. The symbols on the dashed lines (circles, squares and asterisks) are the actual measured values (average from three trials) for the individual sensors. Such fitting gave the calibration parameters k and x for each sensor, which were then used in the Eq.(1) to provide real time measurement of the force applied onto each sensor. After this calibration procedure, we tested the sensor readouts with a set of applied known forces. The results are given by the straight lines in Fig. 2B, showing a linear relationship between the sensed results and the applied forces, where again the symbols of circles, squares and asterisks are the actual sensor readout values for each sensor. The regression for all the sensors indicated ($r = 0.99$ and $p \sim 0.0$), demonstrating an excellent linear relationship between the measured and the applied forces. The measurement error was also assessed less than 5% for each sensor, as shown in the bottom graph of Fig. 4.2 B.

After the calibration and assembly, the final pressure applied to the skin is obtained through dividing the sum of the forces detected from the three FSRs by the contact area of the glass window with the skin (i.e., 3.14 cm^2), and displayed on the computer screen in real time to guide the operators during imaging procedure. The process was faster (<1ms) than the acquisition time of a B frame image, which would meet the requirement of pressure analysis in most contact mode imaging applications.

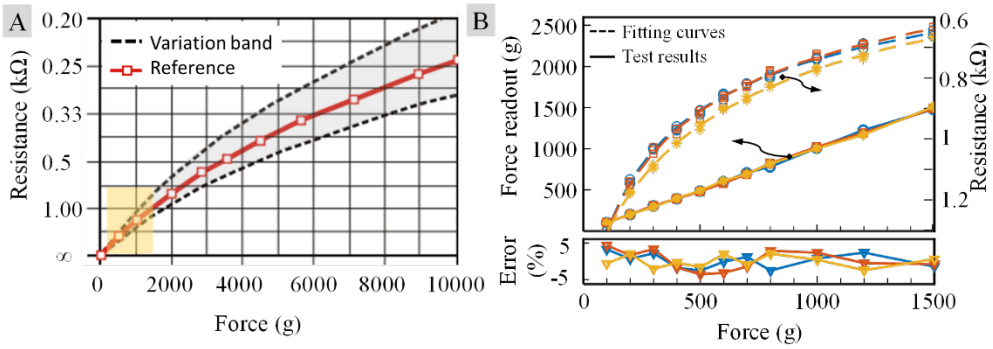

Fig 4.2. Sensor calibration.

(A) The force-resistance characteristics for the FSR sensor (150). The shaded yellow square highlights the calibrated force range in this study. **(B)** Fitting curves from the calibration (dashed lines) to Eq.(1) to obtain the calibration parameters of k and x; and the measured forces from the sensor versus the applied known forces after the sensors are calibrated (solid lines). The triangles in the bottom graphs indicate the measurement errors after calibration.

4.1.3.2 OCTA imaging changes with mechanical stress variations

Figure 4.3 shows a series of in vivo OCTA en face images (Figs. 4.3 A-E) acquired from the palm skin site in a 31-year-old participant with a range of controlled pressures from 0kPa to 69kPa exerted on the skin surface, respectively. Because of 3D OCT/OCTA in nature, we also separated the microvascular information at the selected depths: 245-392μm (Figs.4.3 F-J), 392-672μm (Figs. 4.3K-O) and 672-980μm (Figs.3 P-T), respectively, measured from the skin surface using maximum intensity projection. In addition, to indicate the slab positions that were referenced for extracting the depth resolved vascular information, the selected OCTA B-frame images are given in Figs. 4.3 U-Y for information. Visually, capillary morphology without pressure (Figs. 4.3A and U) and with mild pressure at 11kPa (Figs. 4. 3B and V) is similar and homogenous, suggesting that there is no apparent effect on the vasculature (at least for OCTA imaging) when the applied pressure is up to a level of 11 kPa in this subject. The change of VAD calculated from the MIP of the whole OCTA volume was below 0.13 %, indicating that stable and consistent OCTA images can be obtained with the pressure values less than 11 kPa. However, with the increase of pressure, the vascular density starts to diminish from a pressure level of 17 kPa (Figs. 4. 3 C and W), progressively to 32 kPa (Figs. 4.3 D and X) and eventually the blood flow is almost ceased (within a tissue depth of ~1mm) at the level of 69 kPa (Figs. 4.3 E and Y).

From the depth resolved OCTA images, the response trend of the blood vessels in each layer to the applied pressure is similar to that of the whole layer (i.e., 245 – 980 μm from the surface). The top layer of the dermis (Figs. 4.3 F-J) appeared to undergo more obvious changes after external force stimulation than the other two layers (Figs. 4.3 K-O, and Figs. 4.3 P-T). This may be due to small capillaries being more sensitive to external pressure changes. Fig. 4.4 shows the quantitative comparisons of VAD under different pressures, corresponding to the appearance of OCTA images shown in Fig. 4.3. In addition, the repeatability study showed that all ICCs of the VAD derived from the OCTA imaging were greater than 0.90 (Table 4.1), indicating an excellent repeatability of OCTA imaging (155).

As expected, our study demonstrated a strong correlation between the applied stress and OCTA imaging appearance (Fig. 4.3) and quantification (Fig. 4.4). In general, the compression of skin results in the reduction of skin blood flow, interstitial fluids, skin thickness and closer packing of tissue components (156), which leads to an alteration in the tissue optical property (157). Here, for OCTA imaging, blood

flow reduction is more dominant than other effects on imaging quality. Previous studies extracted the optical property of the skin, such as optical attenuation coefficient (OAC) and tissue birefringent information, to assess wound healing and skin tension lines (158) by using polarization sensitive OCT, however the results were interpretated without the consideration of the potential impact of the compression on the skin. We expect that with the help of pressure sensors during imaging, these measurements would be more reliable and repeatable, giving rise to more accurate interpretation of the final results.

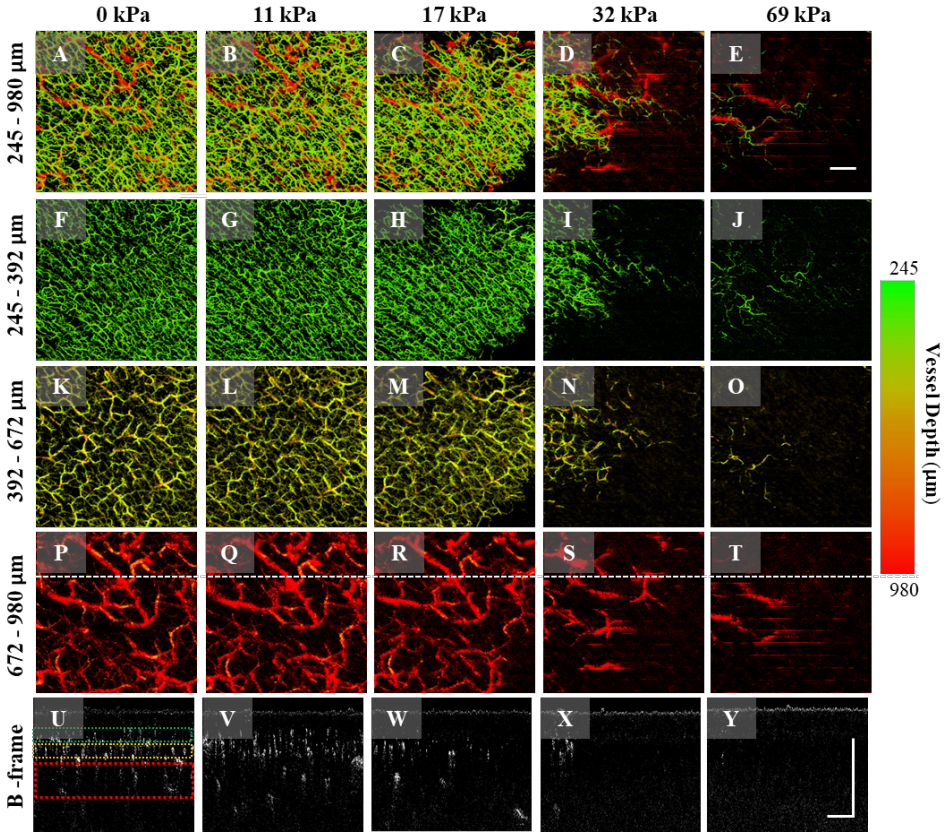

Fig 4.3. The changes in OCTA imaging upon the applied pressures on the skin surface.
(**A-E**) the en face OCTA maps of the whole skin depth from 245-980μm under the pressure of 0, 11, 17, 32, 69, respectively, as shown. **(F-J)** the same as in (A-E) but the selected slab depth of 245–392 µm. **(K-O)** the same as in (A-E) but the selected slab depth of 392–672 µm. (**P-T**) the same as in (A-E) but the selected slab depth of 672-980µm. (**U-Y**) representative OCTA B-scans at the position marked as dashed white line in (P-T), where the green square indicates the depth of 245–392 µm below the surface; the yellow square indicates the depth of 392-672 µm below the surface; and the red square indicates the depth of 672-980 µm below the surface. All en face vascular maps were produced by maximum intensity projection. Color bar represents vessel depth. Scale bar represents 1 mm.

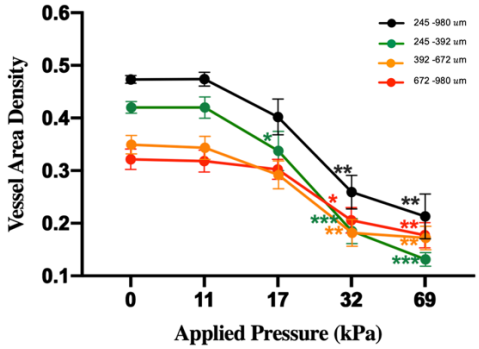

Fig 4.4 The alteration in vessel area density (VAD) upon the applied pressures.
The curves shown are from the whole skin depth (245 - 980μm), and the slab depths of 245-392 μm, 392-672 μm and 672-980 μm, respectively. Error bar represents standard deviation from four sessions. *, P value < 0.05; **, P value < 0.01; ***, P value < 0.001.

Table 4.1 Intraclass correlation coefficient (ICC) among the four tested sessions.

Depth (μm)	245-980	245-392	392-672	672-980
Intraclass Correlation Coefficient (ICC)	0.946	0.971	0.933	0.908

4.1.3.3 Application of pressure sensors in the hyperemia experiment

Figure 4.5 shows the changes in the blood flow in the palm skin after the application of external force (up to ~ 70kPa) and subsequent release. Fig. 4.5A is an en face OCTA image that was used to guide the repeated scanning protocol, where the dashed line indicates the location to acquire temporal OCT (Fig. 4.5B) and OCTA B-scans (Fig. 4.5C). From the temporal OCTA B-scans, the blood flow was assessed from a slab region of interest that was segmented from 245 to 980 μm measured from the surface as marked by dashed box in Fig. 4.5C. Fig. 4.5D is resulted from the MIP projection of this selected slab to indicate the temporal blood flow response at the B-scan cross-section to the applied pressure and then release. To facilitate the visualization, we summed the OCTA blood flow signals within the slab region of interest at each B-scan (to indicate the blood volume), and then plot after the normalization against the time (Fig. 4.5E), where the pressure measured by the sensors is also plotted alongside for comparison. Both the results (Figs. 4.5D and E) demonstrate that the blood volume first decreased due to the external pressure, then produced reactive hyperemic perfusion after the subsequent release of external force at the 38th second, and finally returned to the baseline level. In addition, we observed that besides the variations, the blood flow seemed to fluctuate periodically, likely due to the pulsatile nature of the blood. To confirm, we performed a Fourier transformation on Fig. 4.5E. Fig. 4.5D is the calculated frequency spectrum, showing a characteristic frequency peak at ~1.1 Hz (highlighted by the red asterisk) matched well with the heart rate of the subject (measured separately by a heart rate monitor), confirming that such fluctuations in blood volume is caused

by pulsatile blood movement within the vascular tree. Fig. 4.5G is the magnified view of a selected time window of ~ 3s in Fig. 4.5E, where the periodic pattern with minor local fluctuations is evident that resembles the pulsatile waveform. Meanwhile, the shape of the periodic pattern is also observed to slightly vary under different pressures (Fig 4.5E).

The reason for the reactive hyperemia is that localized pressure applied to the skin activates a large number of cutaneous receptors, leading to vasodilation that gives rise to an increase of skin blood flow. This response can protect skin from ischemia during pressure stimulation (159). However, some conditions, such as diabetes (160), hypertension (161), aging (162) and atherosclerosis (163), can impair this protective mechanism of the microvasculature. Therefore, reactive hyperemia may be utilized as a biological indicator with respect to peripheral microvascular function (164). Wang-Evers et al. (145) reported that OCT imaging had the ability to provide functional information of the microvasculature related to age and blood pressure that might help assess overall vascular health. However, uncontrolled pressure applied to the skin during the experiment may add the burden to the already traumatized skin microvasculature and lead to inaccurate experimental results. Moreover, Xie et al. (123) and Gong et al.(143) reported that OCTA can be used to detect microvascular pulsatility in the peripheral circulation in human skin, in which waveforms are similar to Fig. 4.5E. These two prior studies did not mention the influence of external pressures on the pulsatile waveforms. However, we did observe that such waveform shapes varied under different external pressures. It could be argued that when performing the hyperemia and pulsatile experiment, pressure sensors may be required to help control the external pressure during OCT imaging acquisition. While the observations of blood responses to the applied pressure are sufficiently interesting and may be explored to further our understanding of reactive hyperemia in normal and diseased conditions, the investigation of their physiological meaning or clinical relevance is beyond the scope of the current study. Here, we focused on introducing an augmented pressure sensor during imaging so that the applied level of pressure onto the skin surface can be precisely controlled and monitored.

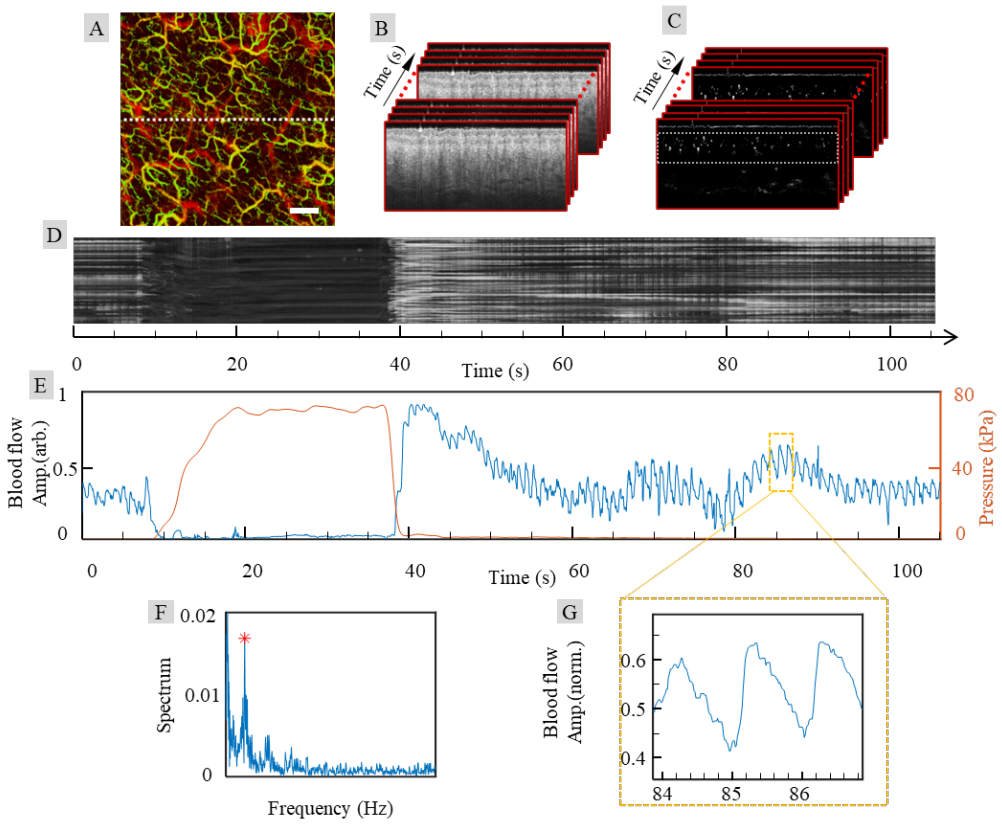

Fig 4.5 The blood flow response to the application and subsequent release of external force to simulate the reactive hyperemia experiments.
(**A**) The en face OCTA map under no pressure that was used to guide the repeated B-scans to generate temporal blood flow signals, where the dashed line indicates the location of the time series of repeated B-scans. The scale bar represents 1 mm. (**B**) the illustration of collected time series of OCT B-scans and **(C)** corresponding temporal OCTA B-scans where the selected slab region of interested is marked by white dashed box. **(D)** Maximum intensity OCTA projection from the region of interest shown in (C) over 105-second repeated B-scans. **(E)** the blue trace indicates the time series of blood flow signals that was obtained by summing the OCTA signals within the region of interest at each B-scan shown in (C). The measured pressures (light red color) during the entire experiment are plotted alongside with the blood flow signal for easy comparison. (**F**) The frequency power of the time series of blood flow signals in (E). The red asterisk indicates the pulsatile component that is measured at 1.1Hz. **(G)** Magnified image of the selected time window of ~3s highlighted in the dashed rectangles shown in (E).

4.1.4 Discussion and conclusions

In the field of OCT/OCTA imaging acquisition, the incorporation of a glass window in direct contact with the skin has evolved into a widely endorsed practice. This strategic approach is geared towards securing consistent and high-quality images, thereby facilitating quantification purpose. Its efficacy lies in the reduction of tissue motion in relation to the OCT probe and the reduction of specular reflections from the skin surface. While undeniably efficient, this method introduces an inherent challenge—a potential imposition of uncontrollable mechanical stress on the skin surface. This stress can induce alterations in the optical properties of the skin, thereby impacting the measurement and imaging of microvascular flows within skin tissue beds. Such effects, in turn, complicate the interpretation of OCT/OCTA results.

Despite this challenge, numerous research groups have harnessed the power of OCT in conjunction with this strategy to scrutinize phenomena such as reactive hyperemia (145), pulsatile waveforms (123,143), and blood glucose levels (156). However, the mechanical pressure exerted on the skin during these studies was often overlooked and not systematically monitored. Therefore, there arises an evident necessity for the monitoring and control of applied pressure during OCT/OCTA imaging acquisition. To the best of the authors' knowledge, the work presented in this study demonstrates for the very first time the ability of pressure sensors to aid in acquiring reliable OCT/OCTA images. A handheld OCT probe combined with built-in force sensors was developed and its potential for skin imaging was demonstrated. With the pressure values provided by the force sensors in real time, an operator can easily determine whether the pressure applied to the skin is within an acceptable range that would not affect OCTA imaging of microvascular information and help to obtain repeatable OCTA images for later quantification purpose. Moreover, when performing reactive hyperemia experiments, the real time monitoring of the applied pressure on the skin would provide a key maneuver information to guide the operator for properly conducting a successful experiment.

Although the current development of an augmented snap-on attachment to the OCT probe is useful in providing the operators with controlled pressure on the skin surface, it should be noted that there are several limitations in our study. Firstly, the FSR integrated in the OCT probe has lower accuracy than other types of force sensors, such as load cells or strain gauges (165). However, these other types of sensors are not as compact as FSRs. It is also worth noting that the precise assessment of the pressure applied on the skin is not the goal of the built-in force sensors. Our current development is merely aimed to provide the operator with a controlled level of skin pressure so as to obtain consistent and reliable OCT/OCTA imaging that can provide meaningful quantification results of microvascular information within skin tissue beds. We believe that the precisions of the chosen FSR sensors are sufficient to monitor noticeable changes in microvascular information upon the application of the external forces on the skin surface. Secondly, we only investigated the effect of pressure on OCTA imaging. To further demonstrate the potentials of pressure sensors in future studies, some other optical properties based on OCT imaging, such as optical attenuation coefficients and birefringent property of the interrogated tissue, could also be analyzed and compared at different pressures under the guidance of the pressure sensor, so that more accurate results can be obtained by removing the possible complications of the contact effect from the interpretation of results. Thirdly, the experiments in this study were only performed on the palm skin, therefore, results are not representative of the skin reaction at other body sites. Based on our previous experiences, facial skin is more sensitive to external pressure compared to the palm skin, while the abdomen skin does seem to be less sensitive to external pressures.

However, the goal of study is aimed at showing the usefulness of real time monitoring of the pressure exerted on the skin surface in order to obtain reproducible and reliable OCT/OCTA skin images.
In summary, we have successfully developed built-in pressure sensors in an OCT handheld probe and demonstrated the application of the pressure sensor in the skin OCTA research. Continued investigations using the technology discussed within will aid researchers/clinicians in betterment of OCT/OCTA data acquisition in the future.

4.2 OCT-Based Angiography and Surface Topography in Burn-Damaged Skin

4.2.1 Introduction

OCTA, as a functional extension of OCT, can provide information regarding functional blood vessels without the need for injecting any contrast agents (35). This is an especially valuable trait for observing burn-damaged skin as contrast agents could cause confounding results due to potential leakage from highly permeable blood vessels (burn damage leads to high vascular permeability (166)). With improvements in resolution, sensitivity, and scanning speeds, OCT is quickly becoming a more routine tool used in dermatologic research (167,168). In addition to the assessment of various pathologies (167), OCT have also been used previously to explore the structural features of burn wounds (169). Building on such work to include the assessment of both structural and vascular features, Lindert *et al*. (170) used dynamic OCT (D-OCT) to investigate the morphologic characteristics of burn injuries in children, highlighting a loss of the epidermal layer, surface irregularities, loss of the dermal papillary pattern, and changes in the microvascular architecture. Taking another direction to demonstrate the highly applicable nature of OCT, a number of studies have combined OCT with other imaging modalities to synergistically ascertain more novel information concerning burn wounds. Further advancing the use of OCT for burn research, our lab recently published work utilizing OCT-based angiography (OCTA) to measure and correlate a number of vascular and structural features of burn wounds (171).

Whilst each study has been successful in its own right for elucidating important findings concerning burn wounds, each is also not without particular shortfalls. For example, to our knowledge, none have classified burn wound zones, defined as specific regions radiating from the wound epicenter immediately following trauma. According to Jackson's Thermal Wound Theory, a typical fresh burn is classified using three zones: zone of coagulation, zone of stasis, and zone of hyperemia (172). The zone of coagulation is the epicenter of the burn, has irreversible tissue loss, and appears white or even charred in color; the zone of stasis surrounds the zone of coagulation and contains cells that would die within 24-48 hours following trauma if they are not managed properly; and the zone of hyperemia, which is the outermost zone surrounding the

zone of stasis that usually appears red and is most likely to recover completely (172,173). In short, the skin in each zone will vary in terms of wound healing potential and process. Therefore, it is crucial to take such zones into account when analyzing a burn wound. With that, the first time point (imaging session #1) used for each of the participants in this study was designed to purposefully delay for at least 72 hours following trauma to allow for the zone of stasis to either progress to become a zone of coagulation or regress to become a zone of hyperemia. This allowed for each zone being imaged to be either white (zone of coagulation) or red (zone of hyperemia). In some cases, we also chose to image mixed sites, which included both red and white coloration.

In this study, we aimed to demonstrate the potential of OCT in assessing burn wound healing and to explore the potential physiological bases of human wound healing. To do this, we built a custom, handheld probe and OCT imaging system, and scanned numerous burn sites on several burn wound victims over multiple time points. We then applied specifically developed algorithms to quantify vascular and structural parameters, such as vascular area density and surface roughness.

4.2.2 Methods

Study Participants

All the scans used in this study were acquired at the Harborview Medical Center, Division of Trauma, Burn, and Critical Care Surgery, Seattle, WA. All the participants met the following criteria: 1) age ≥ 18 years; 2) burn size ≥ 1% total body surface area (TBSA). Study exclusions included: 1) age < 18 years; 2) pregnancy; 3) diabetes mellitus 4) peripheral vascular disease 5) previous vascular surgery on extremity 6) multiple trauma 7) chemical injury; and 8) no discharge follow-up. In total, seven thermal burn patients were included, and all participants voluntarily gave written informed consent. All the participants were scanned at two time points (referred to as imaging sessions), one within 3 – 6 days and the other within 8 – 14 days following injury. Several burn sites, 2 – 4, were scanned from each participant according to the attending surgeon's evaluation. Scan sites were classified into red, white, or mixed (including both red and white) sites based on the color of the wound during imaging session #1. For comparative purpose, five of the seven participants also had scans taken of adjacent healthy skin. The use of OCT was approved by the Institutional Review Board (IRB) of the University of Washington.

Optical Coherence Tomography Imaging System

We used an in-house-built, clinical prototype, OCT system to capture OCT information throughout this study. The OCT system has been explained in detail in our previous publications. In brief, the system used

a 1310 nm swept laser source (SL1310V1- 10048, Thorlabs Inc.) with a spectral bandwidth of 100 nm for a depth resolution of ~ 8μm in tissue (~ 11 μm in air). The custom, handheld probe was equipped with a 6.5", 1080p display monitor, a 5X objective lens, a paired X-Y galvo scanner, sample spacer, and disposable contact unit. The 5X objective lens focused the probing light onto the skin with an incident power of 5 mW, while the paired X-Y galvo scanner generated raster sampling patterns composed of fast (x-axis) and slow (y-axis) axes. The disposable contact unit was designed to be changed quickly and easily between scans or when scanning different participants. A camera was also built into the probe and a ring of light-emitting diodes (LED) was also positioned between the objective lens and contact unit to illuminate the imaging site, allowing for scans to be taken at a specific location.

Data Acquisition

Immediately prior to OCT scanning, sterile glycerin was added to the skin to act as a refractive index matching medium. Each OCT scan then comprised a field-of-view (FOV) of 9 × 9 mm, a lateral resolution of ~10 μm, and a penetration depth of ~1.5 mm. To accommodate this, OCT data were acquired using 800 A-lines per B-frame, 800 B-frame locations per C-scan, and 4 repeated B-frames per B-frame location. The 4 repeated B-frames were then registered into one using a specifically-designed algorithm, optical microangiography (OMAG). This algorithm identifies the locations of functional blood vessels to create vascular maps by extracting specific OCT information derived from the motion contrast of flowing red blood cells (RBCs) in functional blood vessels within surrounding static tissue; hence, OCT-based angiography (OCTA). The image acquisition time for a 3D scan was approximately 6 seconds and for one imaging session, including preparation time and all the scans, was approximately 30 minutes.

Quantification of Vascular Area Density

Prior to the quantification of the vascular area density, acquired 3D OCTA data were first segmented into a ~700 μm-thick slab (measured from the skin surface). Maximum intensity projection (MIP) images were then produced of the segmented slabs by mapping the maximal value in each A-line on to a 2D map, termed an *en face* map. The *en face* maps were depth-color coded to show a vessel depth ranging from 0 – 700 μm.

From these *en face* vascular maps, we then measured vascular area density using algorithms published in previous studies (153). Vascular area density refers to the percentage of functional vascular area per image. In brief, the OCTA-derived *en face* vascular map was firstly processed into a binary image after applying a global threshold, a hessian filter and adaptive threshold. Vascular area and vascular area density were then acquired from the binary image by calculating the number of pixels with non-zero values and the ratio of the number of pixels with non-zero values to the total number of pixels, respectively. For mixed sites

(sites comprising both red and white skin), vascular area density was calculated in red and white sites separately.

Quantification of Skin Surface Roughness

To quantify skin surface roughness, we first detected the skin surface. During the image processing step for segmentation, we obtained the position of the skin surface. To ensure the natural curvature of the skin and the scan angle did not produce any miscalculations for skin roughness due to an increase in the amount of deviations from the average line of the skin surface, we estimated the smooth skin surface position by applying a gaussian filter and a median filter based on the original position of the skin surface. We then obtained relative surface positions by subtracting the processed smooth surface from the original surface. The relative surface was used to quantify skin surface roughness. For convenient visualization, we also generated surface topography maps where a color code was applied to display the relative changes in the height of the skin surface.

Whilst there are many different roughness parameters in use, the arithmetic mean roughness (*S*a) is by far the most common parameter. In this study, we used *S*a to represent skin surface roughness as well as International Organization for Standardization (ISO) 25178 standard definitions for *S*a, i.e., the arithmetic mean of absolute values of heights within a 3D volume (174). *S*a can be expressed as:

$$Sa = \frac{1}{N_x \times N_y} \sum_{i=1}^{N_x} \sum_{j=1}^{N_y} \left| I(\mathrm{x}_{i,} y_j) \right|$$

Where Nx and Ny respectively represent the number of array pixels for the field-of-view (9 × 9 mm), i.e., NxNy indicates the total pixel number in the field-of-view, and I (xi,yj) indicates the vertical distances from the pixel point to the mean height.

Statistical Analysis

Statistical analysis was carried out using GraphPad Prism. One-way analysis of variance (ANOVA) and Tukey-Kramer post-hoc tests were used to compare vascular and structural parameters between imaging sites. Two-sample t tests were performed to compare vascular and structural parameters between imaging sessions. Statistical significance is graphically represented at 4 levels: * $p \leq 0.05$, ** $p \leq 0.01$, *** $p \leq 0.001$, and **** $p \leq 0.0001$.

4.2.3 Results

The anatomical location of each burn injury, the time point of each imaging session in days following injury, the number of control sites scanned, and the number of scans carried out per site category are outlined in Table 5.1 for each participant included in this study. Wound locations included the arm, the buttock, and the chest. The average time point of imaging session #1 was 4.29 days (± 1.38 days) following injury, and the average time point of imaging session #2 was 11.14 days (± 2.48 days) following injury. Five of the seven participants had healthy control scans taken. A total of 3 scans during imaging session #1 and 5 scans during imaging session #2 were categorized as red sites. A total of 16 scans during imaging session #1 and 13 scans during imaging session #2 were categorized as white sites. A total of 4 scans during imaging session #1 and 5 scans during imaging session #2 were categorized as mixed sites. Mixed sites provided vascular measurements for both red and white sites. Mixed sites were excluded from surface roughness measurements; therefore, only those scans categorized as red or white sites were used for surface roughness measurements.

Table.4.2 General characteristics of all participants involved.

Case	Wound Location	Time of Imaging Session (day)		# Scans at Healthy Control Sites	# Scans at Red Sites		# Scans at White Sites		# Scans at Mixed Sites	
		Session #1	Session #2		Session #1	Session #2	Session #1	Session #2	Session #1	Session #2
S-01	Arm	3	14	1	2	3	2	0	0	1
S-02	Arm	5	9	1	0	0	1	2	1	0
S-03	Buttock	6	13	1	0	0	2	2	1	1
S-04	Arm	3	10	1	1	2	2	1	0	0
S-05	Chest	3	10	0	0	0	1	0	2	3
S-06	Chest	6	14	1	0	0	4	4	0	0
S-07	Arm	4	8	0	0	0	4	4	0	0
Mean ± SD		4.29 ± 1.38	11.14 ± 2.48							
Total				5	3	5	16	13	4	5

Vascular Analysis

Shown in Figs 4.6 and 4.7 are the qualitative vascular maps derived from OCTA analysis of one study participant (S-01) during imaging session #1 and #2, respectively. The photograph (Fig 4.6 A) demonstrates a burn wound during imaging session #1 at 3-days post-injury with variable mottled colorization from white to red. Scan sites are highlighted with black boxes and labelled with "W" to indicate a white site and "R" to indicate a red site. The healthy control site is not visible in Fig 4.6 A. Fig 4.6 D and G show the healthy control vascular map and magnified inset, respectively. Visible is a homogenous vascular morphology, density, and distribution. Fig 4.6 B, E and H show the white site vascular maps and magnified inset, respectively. Visible is a comparatively heterogenous vascular morphology and distribution, and a diminished vascular density. Fig 4.6 C, F and I show the red site vascular maps and magnified inset, respectively. Visible, again, is a comparatively heterogenous vascular morphology and distribution, but with an augmented vascular density.

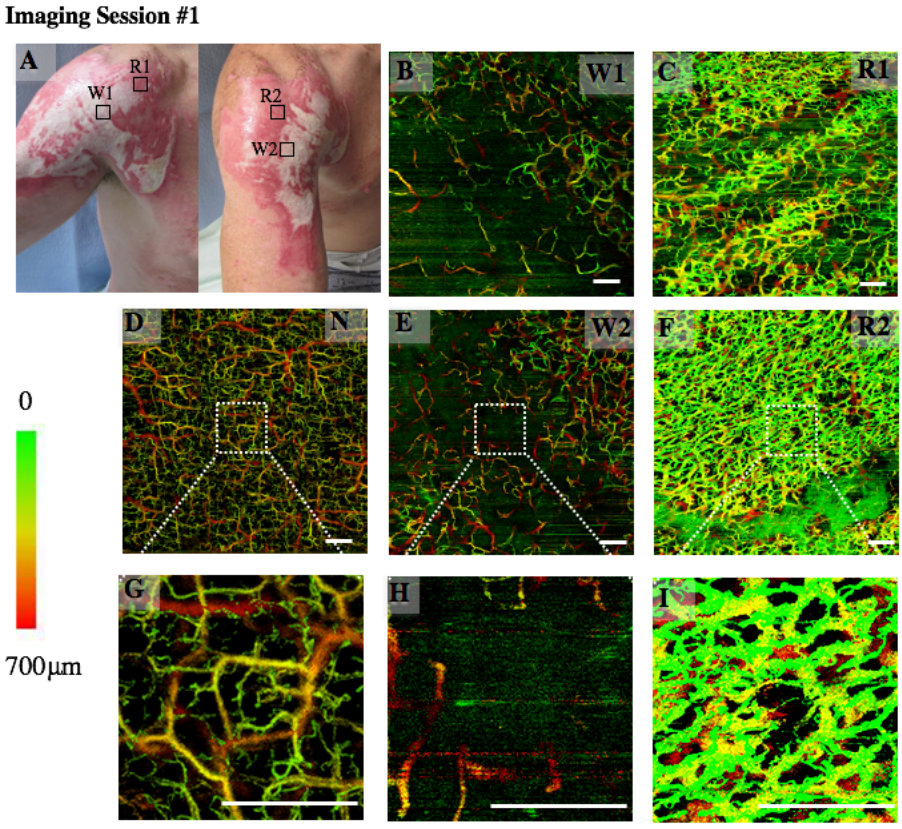

Fig 4.6 En face vascular maps of a burn wound at Day 3 post-injury and a comparative healthy control (S-01). (**A**) Photographs of the burned arm at Day 3 post-injury (imaging session #1). Highlighted are approximate scan sites labeled with R1, R2, W1, and W2. R1 and R2 refer to two red sites, and W1 and W2 refer to two white sites. (**B** and **E**) Vascular maps of the white sites. Shown are scan sites W1 and W2, respectively. (**C** and **F**) Vascular maps of the red sites at Day 3 post-injury. Shown are scan sites R1 and R2, respectively. (**D**) Vascular map of a healthy control. (**G**, **H**, and **I**) Magnified vascular maps derived from the regions highlighted by the white perforated boxes shown in D, E, and F, respectively. All en face vascular maps are projected by maximum intensity. Color bar represents vessel depth. Scale bar represents 1 mm.

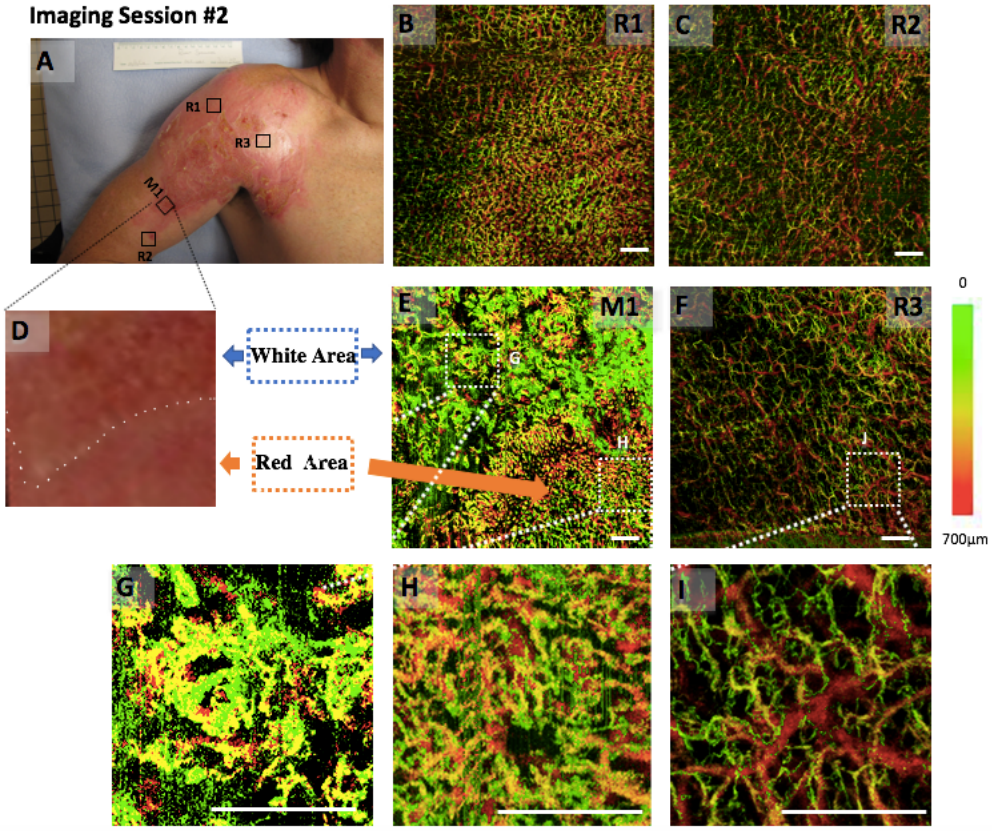

Fig 4.7 En face vascular maps of a burn wound at Day 14 post-injury (S-01).
(**A**) Photograph of the burned arm at Day 14 post-injury (imaging session #2). Highlighted are approximate scan sites labeled with R1, R2, R3, and M1. R1–R3 refer to three red sites and M1 refers to a mixed site. (**B**, **C**, and **F**) Vascular maps of the red sites. Shown are R1, R2, and R3, respectively. (**D**) Magnified photograph of scan site M1. The white perforated line highlights the boundary between the red and white sites. (**E**) Vascular map corresponding to D. (**G**, **H**, and **I**) Magnified vascular maps derived from the regions highlighted by the white perforated boxes shown in E and F, respectively. All en face vascular maps are projected by maximum intensity. Color bar represents vessel depth. Scale bar represents 1 mm.

The photograph (Fig 4.7 A) demonstrates the same burn wound displayed in Fig 4.6 during imaging session #2 at 14-days post-injury. The wound now appears to be predominantly red in color. Scan sites are highlighted and labelled as in Fig 5.1, with "R" indicating a red site and "M" indicating a mixed site. Fig 4.7 D is a magnification of scan site M1 (Fig 4.7A). The boundary between the white and red sites is highlighted with a white perforated line. Fig 4.7 B, C, F, and I show the red site vascular maps and magnified inset, respectively. Visible, still, is a heterogenous vascular morphology and distribution with an augmented vascular density, but such features are no longer as pronounced as in imaging session #1 and appear to be normalizing to more resemble the features of the healthy control (Fig 4.6 D and G). Fig 4.7 E shows contrasting features in the mixed site. Fig 4.7 E and G show a comparatively higher vascular density compared to the white sites imaged during imaging session #1 with a vascular morphology that the blood vessels grow around hair follicles. Fig 4.7 E and H show vascular features more similar to those described in the red sites of Fig 4.7 B, C, F and I.

Shown in Fig 4.8 are the qualitative vascular and structural maps of another study participant (S-07) during both imaging sessions. Fig 4.8 A and F show the photographs of the burn wound during imaging session #1 and #2 at day 4 and 8 post-injury, respectively. Mottled colorization from white to red are visible with regions of brown discoloration also. Scan sites are highlighted with black boxes and labelled with "W" to indicate a white site. Fig. 4.8 B – E show a very diminished vascular density during imaging session #1 making other features difficult to determine. Fig 4.8 G – J shows an improved vascular density during imaging session #2 compared to imaging session #1, but vascular morphology and distribution remains compromised compared to the healthy control (Fig 4.6 D and G). Fig 4.8 K – N are structural maps at the sites corresponding to the vascular maps of Fig 4.8 G – J. The dark regions shown are thought to represent hair follicles. Fig 4.8 O – R demonstrate merged vascular and structural maps. This is thought to confirm that the vascular morphology seen in Fig 4.8 G – J represents a vascular morphology surrounding highly active hair follicles.

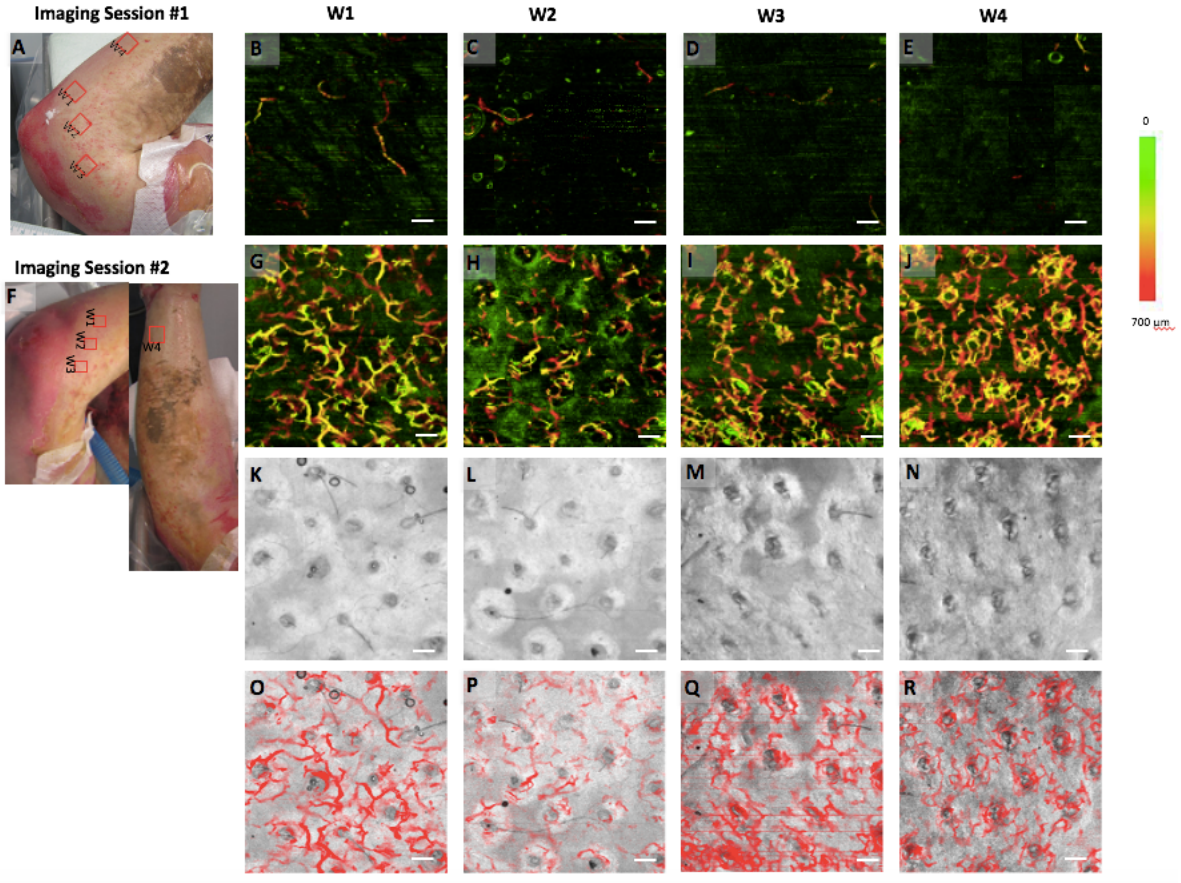

Fig 4.8 En face vascular and structural maps from a burn patient with all-white sites spanning two imaging sessions (S-07). (**A** and **F**) Photographs of the burned arm at Days 4 and 8 post-injuries, respectively. Highlighted are approximate scan sites labeled W1, W2, W3, and W4. W1–W4 refer to four white sites. (**B**–**E**) Vascular maps of the white sites on day 4 post-injury. Shown are W1, W2, W3, and W4, respectively. (**G**–**J**) Vascular maps of the white sites at Day 8 post-injury. Shown is W1, W2, W3, and W4, respectively. (**K**–**N**) Structural maps corresponding to G–J, respectively. (**O**–**R**) Vascular maps corresponding to G–J, respectively,

overlaid onto structural maps corresponding to K–N, respectively. All en face vascular and structural maps are projected by maximum intensity. Color bar represents vessel depth. Scale bar represents 1 mm.

Shown in Fig 4.9 are the quantitative vascular area density measurements representing all participants over both imaging sessions. Fig 4.9 A shows that during imaging session #1, vascular area density in the red sites averaged a significantly higher value compared to that of the healthy controls ($p = 0.0130$), while the vascular area density in the white sites averaged a significantly lower value compared to that of the healthy controls ($p < 0.0001$). Fig 4.9 B shows that during imaging session #2, vascular area density had normalized in the red sites, but remained significantly lower in the white sites compared to that of the healthy controls ($p < 0.0001$). Additionally, when we compare the red sites alone over both imaging sessions (Fig 4.9 C), vascular area density at imaging session #2 was significantly reduced compared to imaging session #1 ($p = 0.0215$). The opposite is true when we compare the white sites alone over both imaging sessions (Fig 4.9 D), ($p < 0.0001$).

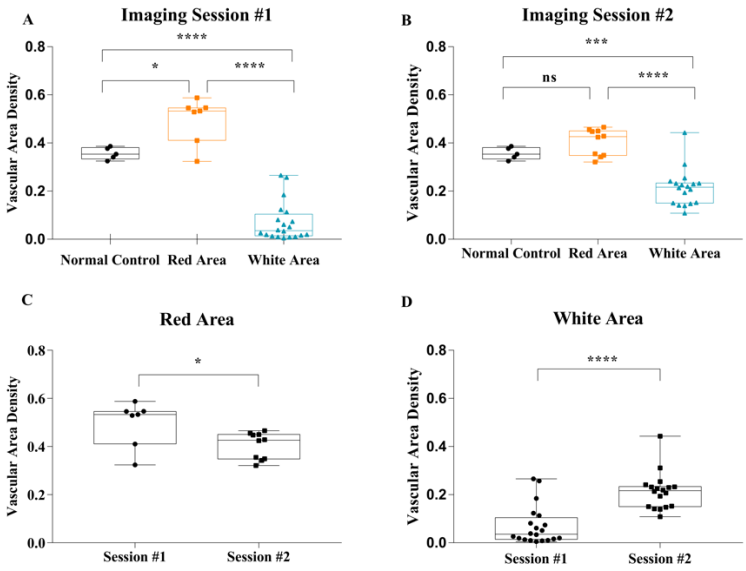

Fig 4.9 Graphic representation of vascular area density measurements.
(**A** and **B**) Comparison of vascular area density among the healthy control, and the red and white sites during imaging session #1 and #2, respectively. (**C** and **D**) Comparison of vascular area density between both imaging sessions at the red sites and white sites, respectively. ns, not statistically significant. *P ≤ 0.05, ***P ≤ 0.001, and ****P ≤ 0.0001. Boxplots show interquartile range, whiskers minimum to maximum.

Surface Roughness Analysis

Shown in Fig 4.10 are the qualitative topography maps derived from the same participant represented in Fig 4.6 and 4.7 (S-01). Here, a blue color represents the lowest surface with a height of 0µm, and a red color represents the highest surface within a scan with a height of 120µm or more. Fig 4.10 A and B show the topography map and corresponding B-frame, respectively, of healthy control skin. A homogenously

distributed mix of red to blue colors can be seen. Comparatively, Fig 4.10 C – J show the skin surface of both white and red sites during imaging session #1. In both white and red sites, the skin appears smoother with a more uniform color scheme. During imaging session #2, the skin surface roughness does not appear to have changed significantly in two of the three scans (Fig 4.10 K, L, N and O); however, the third scan appears more similar to that of healthy skin (Fig 4.10 M and P).

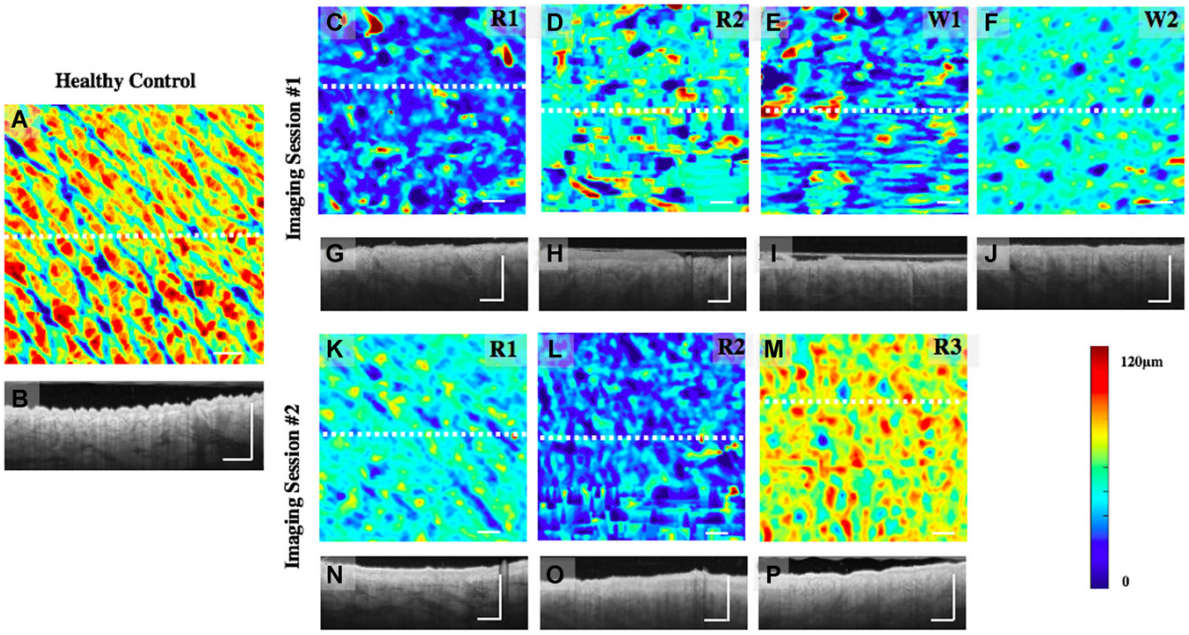

Fig 4.10 Topography maps of a burn wound spanning two imaging sessions (S-01).
(**A** and **B**) Topography map of a healthy control and corresponding cross-sectional B-frame, respectively. The B-frame is derived from the location highlighted with a perforated white line in A. (**C**, **D**, **E**, and **F**) Topography maps of a burn at Day 3 post-injury. Shown are scan sites R1, R2, W1, and W2 from Fig 3.1 A, respectively. (**G**, **H**, **I**, and **J**) Cross-sectional OCT B-frames corresponding to the locations highlighted with perforated white lines in C, D, E, and F, respectively. (**K**, **L**, and **M**) Topography maps of a burn at Day 14 post-injury. Shown are scan sites R1, R2, and R3 from Fig 3.2A, respectively. (**N**, **O**, and **P**) Cross-sectional OCT B-frames corresponding to the locations highlighted with perforated white lines in K, L, and M, respectively. Color bar represents variations in surface height. Scale bar represents 1 mm.

Shown in Fig 4.11 are the qualitative topography maps derived from the same participant represented in Fig 4.8 (S-07). During imaging session #1, the skin again appears smoother with a more uniform color scheme compared to the healthy control (Fig 4.11 A – H). During imaging session #2, the skin still appears smooth compared to the healthy control, but raised areas are visible that correspond with hair follicles (Fig 4.11 I – P).

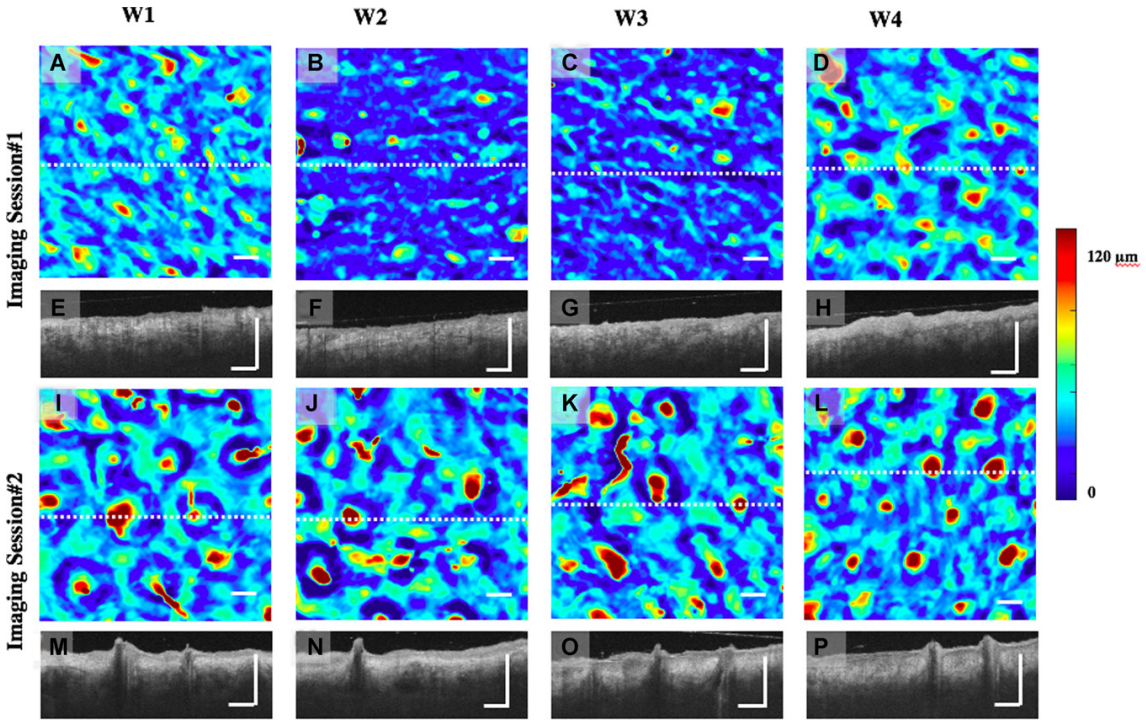

Fig 4.11 Topography maps of a burn wound spanning two imaging sessions (S-07).
(**A**, **B**, **C**, and **D**) Topography maps of a burn at Day 4 post-injury. Shown are scan sites W1, W2, W3, and W4 from Fig 3.3A, respectively. (**E**, **F**, **G**, and **H**) Cross-sectional optical coherence tomography (OCT) B-frames corresponding to the locations highlighted with perforated white lines in A, B, C, and D, respectively. (**I**, **J**, **K**, and **L**) Topography maps of a burn at Day 8 post-injury. Shown are scan sites W1, W2, W3, and W4 from Fig 3.3 F, respectively. (**M**, **N**, **O**, and **P**) Cross-sectional OCT B-frames corresponding to the locations highlighted with perforated white lines in I, J, K, and M, respectively. Color bar represents variations in surface height. Scale bar represents 1 mm.

Quantification analysis of surface roughness is shown in Fig 4.12. During imaging session #2, white sites appeared significantly rougher compared to the red sites ($p = 0.0174$) (Fig 4.12 B). Surface roughness also appeared to significantly increase in the white sites from imaging session #1 to #2 ($p < 0.0001$) (Fig 4.12 D).

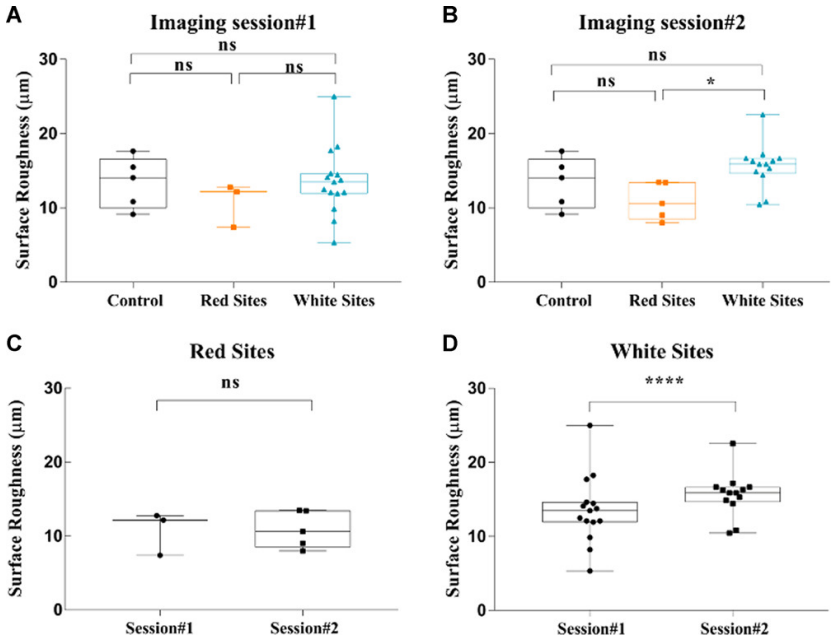

Fig 4.12 Graphic representation of surface roughness measurements.
(**A** and **B**) Comparison of surface roughness among the healthy control, and the red and white sites during imaging session #1 and #2, respectively. (**C** and **D**) Comparison of the surface roughness between both imaging sessions at the red sites and white sites, respectively. *P ≤ 0.05, and ****P ≤ 0.0001. Boxplots show interquartile range, whiskers minimum to maximum.

4.2.4 Discussion

In this study, we have demonstrated the capability of OCT/OCTA to image and monitor burn wound healing. To the best of our knowledge, this is also the first time such an OCT study has classified burn wounds into zones based on Jackson's Thermal Wound Theory, i.e. zones of coagulation (white sites) and zones of hyperemia (red sites) (172). For comparative purposes, we have also assessed mixed zones (mixed sites containing both white and red sites) and healthy controls.

Clinically, blood perfusion analysis for burn wound assessment is not uncommon and is most frequently observed by prolonged blanching of the skin following compression. Like all similar assessment methods, however, this is subjective and often unreliable. OCT/OCTA, on the other hand, is capable of providing a more precise burn wound assessment by directly imaging and indirectly quantifying numerous vascular and structural parameters. Here, we have observed that, compared to healthy skin, vascular area density was decreased in white sites but increased in red sites in the days immediately following burn injury (Figs. 4.6, 4.8 and 4.9). These findings support Jackson's Thermal Wound Theory where zones of coagulation, white sites in this case, have severely compromised perfusion and zones of hyperemia, red sites in this case, have significantly increased perfusion (172). Previous OCT studies that assessed vasculature have reported both

the increased and decreased vascular densities, but none have correlated such with burn wound zones (170,175).

When reassessing vascular features during the second imaging session (imaging session #2), we noted that the vascular area density measured within the white sites had significantly increased compared to imaging session #1 (Fig 4.9 D), and the vascular area density within the red sites had significantly decreased compared to imaging session #1 (Fig 4.9 C). The red sites were now showing vascular area density similar to those found in healthy skin (Fig 4.6 and 4.9 B). These findings are again consistent with Jackson's Thermal Wound Theory, which states that zones of coagulation, white sites in this case, might recover over time due to angiogenesis, and zones of hyperemia, red sites in this case, will invariably normalize over time.

Interestingly, however, the vascular area density measured here in the white sites during imaging session #2 were still significantly lower than comparable measures of healthy skin (Fig 4.9 B) meaning the white sites had not yet recovered, as the red sites had. This is thought to be due to the time following injury in which imaging session #2 was carried out, i.e. 8- to 14-days post-injury. This is important as deep superficial thickness burn wounds (all participants here had deep superficial thickness or full thickness burn wounds) typically require more than 21 days to recover (176). Therefore, the significantly lower vascular area density values noted within the white sites during imaging session #2 are likely attributed to incomplete wound healing. Moreover, we observed that the recovering blood vessels tended to grow around hair follicles (Fig 4.6 and 4.8). This is expected to be because nascent blood vessels in the skin are derived from nestin-expressing hair-follicle cells (177). With that, the recovering blood vessels imaged here by OCTA could indicate a higher metabolic requirement within the skin due to re-epithelialization originating from the hair follicles (178), and so it could be argued that such is a biological marker that could be used to indicate wound healing.

Qualitatively, we found that the burn-damaged skin assessed here had a different surface topography compared to a healthy control (Fig 4.10 and 4.11). Whilst a loss of skin surface texture in burned skin has been reported elsewhere (170), we did not find a significant difference in surface roughness between the burn wounds (either white sites or red sites) and healthy skin in the days immediately following injury (Fig 4.12 A). It is suspected that the relatively smoothening of the skin surface roughness may be due to removal of the epidermal layer followed by local edema, both common features of severe acute burn injury (179). The reason for a lack of quantifiable changes, however, remains unclear, but is potentially due to systemic edema in the days following injury reducing the surface roughness of control skin and re-epithelialization increasing the surface roughness of burn wound sites. Combined, these medical traits might explain why

the visual surface topography differed, but the quantifiable surface roughness did not. During reassessment (imaging session #2), red sites appeared to be, visually, more comparable to that of healthy skin. Although these apparent observations were not quantifiable, similarly normalizing vascular features are thought to synergistically indicate appropriate healing. Additionally, the skin surface of the white sites was visually raised over the hair follicles during imaging session #2 (Fig 4.12 I – P). This phenomenon might be due to a suppression of edema. As swelling decreases, follicles might become more apparent as they are the largest structures in the skin. It is also possible that increased blood vessels around the follicles result in the follicles "remaining swollen" as the rest of the tissue reduces in size. In all, loss of skin texture and changes in surface roughness might be important indicators to evaluate burn wound conditions, but these are typically not easily distinguishable using normal clinical evaluation methods. OCT could be used to provide information regarding surface topography and roughness to assist clinicians or surgeons in closely monitoring burn wound.

Although promising, it should be noted that there are a number of limitations within our study. First, the field-of-view used here was only 9 × 9 mm, meaning information could be lost if the burn wound was to cover an area of skin of several inches or larger. To overcome this and to include as much information as possible about the burn wound, we chose 2 – 4 scan sites per participant, including the zone of coagulation and zone of hyperemia, as directed by the attending surgeon's evaluation. Another plausible method to overcome such a limitation would be to combine OCT with another imaging modality with a larger field-of-view and subsequently lower resolution, such as laser Doppler imaging, thermography, or hyperspectral imaging, to highlight areas of interest prior to imaging with OCT/OCTA. This would help to limit the shortfalls of each modality and augment their applicability and ability to provide clinically valuable information (167). Second, the small sample size used here has likely limited the significance of the data found due to potentially larger standard deviations between participants, such as the difference in surface roughness between the burned skin and the healthy skin. Third, our study only involved two follow-up time points, which may have negatively impacted the comprehensiveness of our understanding of burn wounds. As OCT, and OCTA in particular, is a relative newcomer to the field of dermatology (having been initially developed for ophthalmology), it is comparatively unknown to those we are attempting to assess with it, making it challenging to follow-up with burn patients. This is unfortunately a common feature for now with OCT and burn assessment studies (171,175,180). Our future studies will recruit more burn participants to perform multiple OCT/OCTA imaging sessions to help us further understand the healing process of burn wounds.

To conclude, our study has successfully demonstrated the feasibility of OCT/OCTA to image and monitor vascular and surface roughness progression during human burn wound healing. Continued investigations using the technology and parameters discussed within will help us to understand the underlying pathophysiological mechanism of wound healing, which could be good biological indicators to monitor clinical wound healing in the future clinical practice.

4.3 Imaging human skin autograft integration with optical coherence tomography

4.3.1 Introduction

Skin autografting is a form of reconstructive surgery that involves the transfer of skin from a healthy donor site to a recipient site in a need of repair on the same person. It has been widely used as a treatment strategy to improve the quality of life for patients suffering from burn damage, trauma, or cancer (181). Skin autografts can be harvested as split-thickness or full-thickness grafts, of which split-thickness skin grafts are more frequently used for tissue coverage. A split-thickness skin graft includes epidermis and varying amounts of dermis, with a thickness ranging between 125 μm and 750 μm (182). With that, any visualization of a skin graft integrating into the recipient tissue beneath would require an imaging technique capable of providing cellular-level resolution and an imaging depth of at least 1 mm. Initially, a skin graft does not have its own blood supply and must therefore rely on the wound bed for nutrients (183). Such a process ensures that the viability of a skin graft during the early stages of incorporation is entirely determined by its integration with the blood supply of the recipient tissue beneath. Any buildup of fluid between the skin graft and wound bed caused by hematoma, seroma or infection could impact the ability of the recipient tissue's blood supply to connect with the graft resulting in an incomplete graft take or even failure. Therefore, a technique to reliably assess the structure and vascular perfusion of individual layers, i.e., the graft itself and the intermediate layer between the graft and recipient tissue, referred to here as the integration layer, over time would greatly facilitate our ability to identify complications early and monitor the integration process of the skin graft.

Whilst numerous studies have been carried out to evaluate and optimize both surgical and post-operative practices regarding skin transplantation (184–192), little research has been conducted to develop appropriate techniques to objectively and accurately evaluate skin graft health post-surgery. The studies that have assessed graft healing were typically invasive or employed the use of animal models (186,189,192), or measured superficial parameters, such as graft contraction (190), and re-epithelialization (191). Notwithstanding the considerable improvements in the availability and applicability of modern non-

invasive imaging technologies (167), the authors are unaware of any studies carried out to apply these technologies to human skin graft subsurface imaging and assessment.

In a clinical setting, graft health is typically assessed via visual inspection by health providers (193). In the event of graft failure or incomplete integration, the extraction of biopsies is currently thought to be the only accurate method available to determine the cause of failure. This is not ideal, however, as biopsies cause further tissue damage, can be time consuming, increase the risk of infection, and may introduce inaccurate results if the wrong site is chosen for assessment. Moreover, repeated biopsies could result in a complication of scarring. The need for a non-invasive imaging modality that could aid in monitoring graft health is ever-present. For that reason, we have employed here the use of a non-invasive imaging modality capably of assessing both vascular and structural features of the skin to monitor graft health over time.

OCTA distinguishes blood vessels from the surrounding static tissue by measuring OCT signal differences at the same location over multiple time points in quick succession. Blood vessels become distinct because the OCT signal derived from blood flow varies over time, while the OCT signal backscattered from the surrounding static tissue remains almost unchanged (35). Additionally, advances in the development of algorithms, such as attenuation correction, segmentation, *en face* mapping, thickness measurement, and vascular measurement, allow for the imaging and analyzing of structural and vascular features in individual layers both qualitatively and quantitatively.

In this study, we aimed to explore the potential of applying OCT/OCTA to visualize and monitor the healing and integration of skin autografts. To do this, we used a prototype OCT imaging system capable of extracting OCTA information to visualize and analyze the vascular (via OCTA-derived blood vessel mapping) and structural (via OCT-derived attenuation correction mapping) features of the graft itself and the corresponding integration layer beneath.

4.3.2 Methods

Subject Volunteers

Two patients (denoted as patient #1 and patient #2) who underwent split-thickness skin graft surgery following severe burn damage to the skin were recruited, consented, and scanned at two separate time points post-operatively. Both patients had 250 μm-thick autologous grafts excised from the upper thigh and transplanted to the dorsum (patient #1) or ventrum (patient #2) of the right forearm. Both patients received sheet grafts (not meshed). Patient #1 was scanned at 7- and 16-days post-surgery, and patient #2 was

scanned at 6- and 14-days post-surgery. Multiple scan sites, i.e., 3 – 4, were chosen for each patient. For comparative purposes, patient #1 had adjacent burn site and control site scans (contralesional forearm) carried out in addition to three graft site scans. Patient #2 had only three graft scans carried out. The use of OCT laboratory equipment on human subjects was reviewed and approved by the Institutional Review Board of the University of Washington.

OCT Imaging System

The system setup was the same as section 4.2.2.

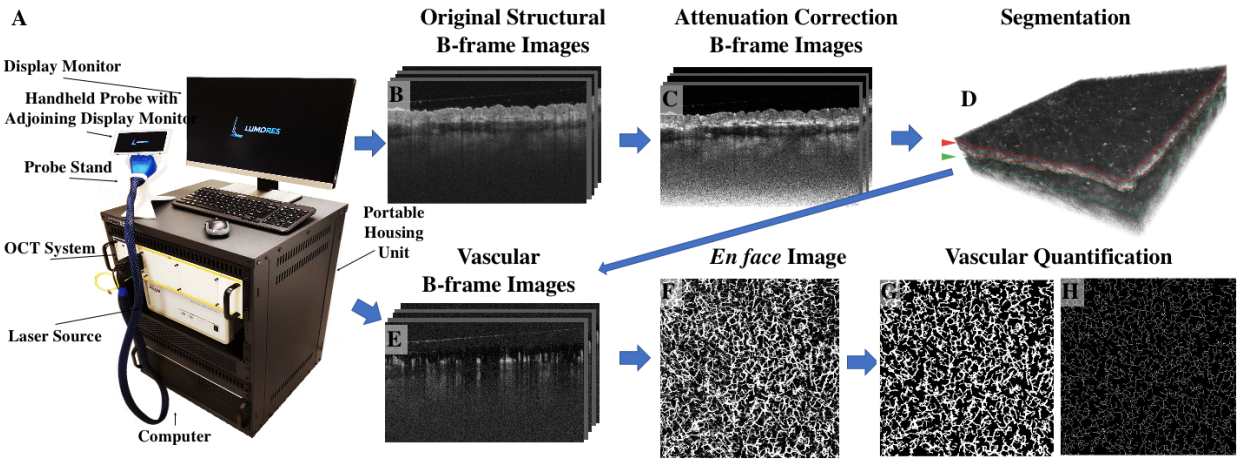

Fig 4.13 Images showing the prototype OCT system alongside a schematic of data processing.
(A) The prototype OCT system capable of OCTA data acquisition. (B) Original structural cross-section B-frame images. (C) Attenuation correction cross-section B-frame images. (D) 3D structure image. Red lines highlight graft layer boundaries (graft layer further highlighted with a red arrow) and green lines highlight integration layer boundaries (integration layer further highlighted with a green arrow). Layer segmentation was carried out using these lines. (E) Vascular cross-section B-frame images. (F) Original en face projection of 3D blood vessels. (G) Binarized vascular image used for the quantification of vascular area density. (H) Skeletonized vascular image used for the quantification of vascular diameter.

Imaging Protocol

Briefly, 3D OCT scans were acquired with a field of view of 9 × 9 mm, a penetration depth of ~1.5 mm and lateral resolution of ~10 μm using 800 A-lines to produce a single B-frame, and 800 B-frame locations with 4 repeated B-frames in each, to produce a single volumetric C-scan. Each of the 4 repeated, single-location B-frames were then registered into one using optical microangiography (OMAG) to extrapolate OCTA information, i.e., blood flow information. OCT and OCTA provided structural and vascular information, respectively (Figs 4.13 B, E).

Attenuation Correction Mapping

The contrast between the graft and integration layer is low in the OCT images because the intensity of OCT light is exponentially attenuated along its path as the light beam propagates through the skin due to the scattering and absorption of said light. To enhance the contrast between the graft layer and integration layer in the OCT image, so as to facilitate the segmentation algorithm for accurately separating adjacent layers, we applied an attenuation correction algorithm to the structural images. According to Vermeer *et al*. (36), the OCT signals compensated with attenuation correction at each pixel, $\mu(i)$ can be expressed as:

$$\mu[i] \approx \frac{I[i]}{2\Delta \sum_{i+1}^{\mathrm{N}} I[i]}$$

Where $I(i)$ refers to the OCT signal at the i -th pixel along the depth, Δ is the pixel size, and N is the last pixel of the A-line. It is assumed that most light is already completely attenuated at the end of each A-line.

In order to further improve the contrast of the image, we applied exponentiation before attenuation compensation, and each pixel intensity is converted as:

$$U_{Attn-corr}[i] = \frac{I^2[i]}{2 \sum_{i+1}^{\mathrm{N}} I^2[i]}$$

Where $U_{Attn-corr}$ is the signal corrected by exponentiation and attenuation compensation (38). This approach improves the ability to detect the boundaries between adjacent layers (Fig 4.13 C), which aids us in segmentation.

Image Segmentation

As mentioned above, assessing the structure and vasculature of the graft and integration layers independently plays a critical role in identifying complications early and evaluating the integration of said skin graft. To visualize the individual layer's features independently, we segmented the 3D attenuation correction images into separate graft and integration layers. Each layer was acquired by semi-automatically outlining the layer boundaries within the attenuation correction B-frame images of each volumetric C-scan (Fig 4.13 D). The same segmentation information was then applied to vascular imaging volumes; that is, the vascular imaging volumes were also segmented at these depths (Fig 4.13 E).

***En face* Mapping of Layer Thickness and Vessel Measures**

For convenient visualization and further quantification, *en face* images were generated based on segmented volumes. An *en face* thickness map was obtained by calculating the depth separation between the upper and lower boundaries of each layer (i.e. graft layer and integration layer) at each A-line. A color-code was subsequently applied to represent a thickness range of 0 – 500 μm. The processed OCTA volumetric data was collapsed into a two-dimensional (2D) map with a maximum intensity projection (MIP), where the highest intensity along the depth was chosen for each A-line, allowing for the generation of a 2D map, termed as *en face* map (Fig 4.13 F). Where applicable, color codes were applied to *en face*-projected vasculature to represent a vessel depth ranging from 0 – 1 mm.

Quantification of Layer Thickness, and Vascular Area Density and Diameter

To demonstrate the potential of OCT to assess post-operative recovery of skin grafting objectively, we measured multiple layer thicknesses, as well as vascular area density and diameter values from both the graft and corresponding integration layer of both patients at both time points. Mean thickness measurements were taken from each layer (i.e., graft layer and integration layer) based on the segmentation information. Measurements of vascular area density and vascular diameter were performed on each layer using *en face* images with a procedure developed in previous studies(153,194), where vascular area density refers to the percentage of vascular area in OCTA images. To calculate vascular area density, the *en face* vascular map was processed into a binary image (Fig 4.13 G) by carrying out global thresholding and applying a hessian filter and adaptive thresholding. A skeletonized vascular image (Fig 4.13 H) was then generated from the binary image, in which each blood vessel, ignoring its diameter, was shown as a single-pixel line. The length of the blood vessels was then extracted from the skeletonized image, which allowed us to calculate the average vascular diameter by dividing total vascular area by total vascular length.

Statistical Analysis

Three measurements of each layer thickness, vascular area density and diameter were averaged and presented as mean ± standard deviation. Two imaging sessions were compared using two sample t-tests. Statistical significance is represented at two levels: * $P \leq 0.05$, and ** $P \leq 0.01$.

4.3.3 Results

Presented here are the OCT- and OCTA-derived features observed over time as the grafted autologous skin tissue integrated with the severely burn-damaged skin tissue beneath. Fig 4.14 shows the vascular (through *en face* vessel maps) changes that occurred within and immediately below the graft over the dorsum of the

right forearm of patient #1. Fig 4.14 A and F shows the grafted forearm at 7- and 16- days post-surgery, respectively, with approximate scan locations and dividing graft borderline highlighted. For comparative purposes, multiple OCT scans were taken of the graft, adjacent burn and equivalent healthy sites (contralesional forearm). Fig 4.14 D alongside a magnified inset, Fig 4.14 E, shows that the control site has a homogenous vascular morphology, density, and distribution. Comparatively, Fig 4.14 I and J (a burn site adjacent to the graft) show that the burn-damaged skin has extremely high vascular area density, even at 23-days post-burn, making it difficult to identify individual vessel morphology. Comparatively again, Fig 4.14 B and C show that the vasculature of the graft just 7-days post-surgery already with a morphology and distribution more akin to that of the normal control (Fig 4.14 D and E), albeit with fewer superficial blood vessels (shown as green vessels in Fig 4.14). Fig 4.14 G alongside a magnified inset, Fig 4.14 H, shows the vasculature of the graft 16-days post-surgery, where the vasculature appears even more reminiscent of the normal control compared to the first imaging session.

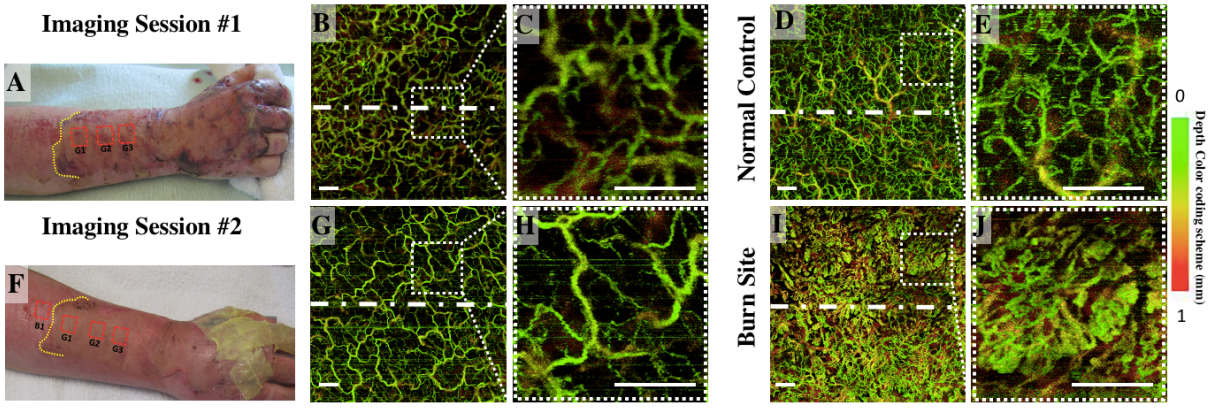

Fig 4.14 En face OCTA imaging of patient #1.
(A, F) showing photographs of the grafted forearm 7-days and 16-days post-surgery, respectively. Highlighted are approximate scan sites (red perforated boxes) labeled G1, G2, G3 and B1. G1 – G3 refer to three graft sites, and B1 refers to a burn site adjacent to the graft. The graft boundary is also highlighted (yellow perforated line). (B, C) demonstrating the graft vasculature 7-days post-surgery from scan site G2. (D, E) showing the vasculature of the normal skin (contralesional forearm) on the same patient. (G, H) showing the graft vasculature 16-days post-surgery from scan site G2. (I, J) showing the vasculature of a burn site adjacent to the graft 23-days after the initially burn injury from scan site B1. (C, E, H, J) Magnified images of the regions highlighted in the dashed rectangles shown in (B, D, G, I). All en face images are maximum intensity projected. Color bar represents vessel depth. Scale bar represents 1 mm.

Fig 4.15 shows the representative cross-sectional B-frames of the tissue structure (after attenuation correction processing) at the position indicated by the white dashed lines in Fig 4.14 In these images, the epidermal–dermal junction and adjacent layer boundaries are clearly observed. The yellow dashed line highlights the epidermal–dermal junction. The red dashed line highlights the lower boundary of the graft layer and the upper boundary of the integration layer. The green dashed line highlights the lower boundary

of the integration layer and the upper boundary of the recipient tissue. Fig 4.15 B shows the normal control with a smooth and consistent structure. In contrast, Fig 4.15 D shows the burn-damaged skin structure with a rough epidermis. Fig 4.15 A demonstrates that the epidermis of the graft tissue is significantly thicker than that of the normal control site with the integration layer also being clearly visible beneath. Fig 4.15 C shows that over time, the epidermal thickness returned to a level closer to that of the normal control, as evidenced when comparing the second imaging session to the first. Additionally, the integration layer in the second imaging session is also thinner and less pronounced compared to the first imaging session.

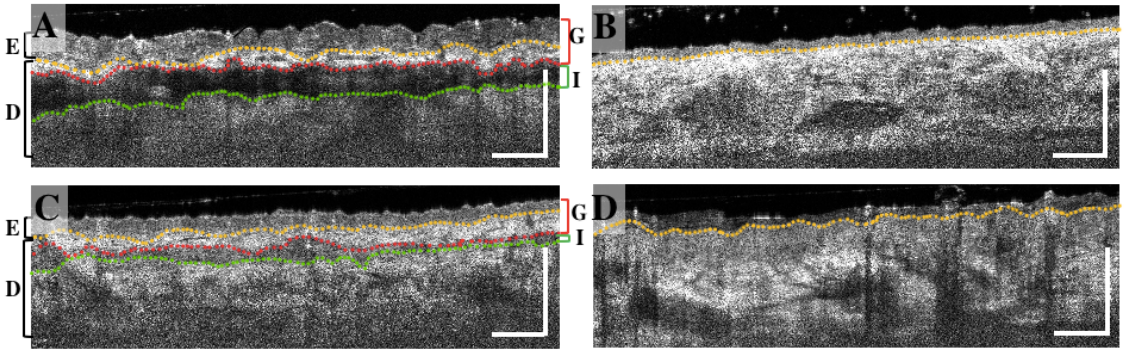

Fig 4.15 Representative cross-sectional B-frames of OCT structure (after attenuation correction processing).
Shown are the B-frames acquired at the site indicated by the white dashed lines in Fig 4.2 (A, C, E, G). (A) shows the graft 7-days post-surgery. (B) shows the normal skin (contralesional forearm) on the same patient. (C) shows the graft 16-days post-surgery. (D) shows a burn site adjacent to the graft 23-days after the initial burn injury. Yellow dashed lines highlight the epidermal–dermal junction. Red dashed lines highlight the boundary between graft layer and the integration layer. Green dashed lines highlight the boundary between the integration layer and the recipient tissue. Scale bar represents 1 mm. E, epidermis; D, dermis; G, graft layer; and I, integration layer.

Shown in Fig 4.16 are the same graft scans presented in Fig 4.14 and Fig 4.15 only segmented into two distinct layers, i.e. the graft layer and integration layer, to separately demonstrate the vasculature and thickness maps of each layer. For patient #1, it appears that the vascular distributions in both the graft and integration layer were more homogeneous in the second imaging session compared to the first. Additionally, the graft and integration layers both seemed to have thinned between the first and second imaging session.

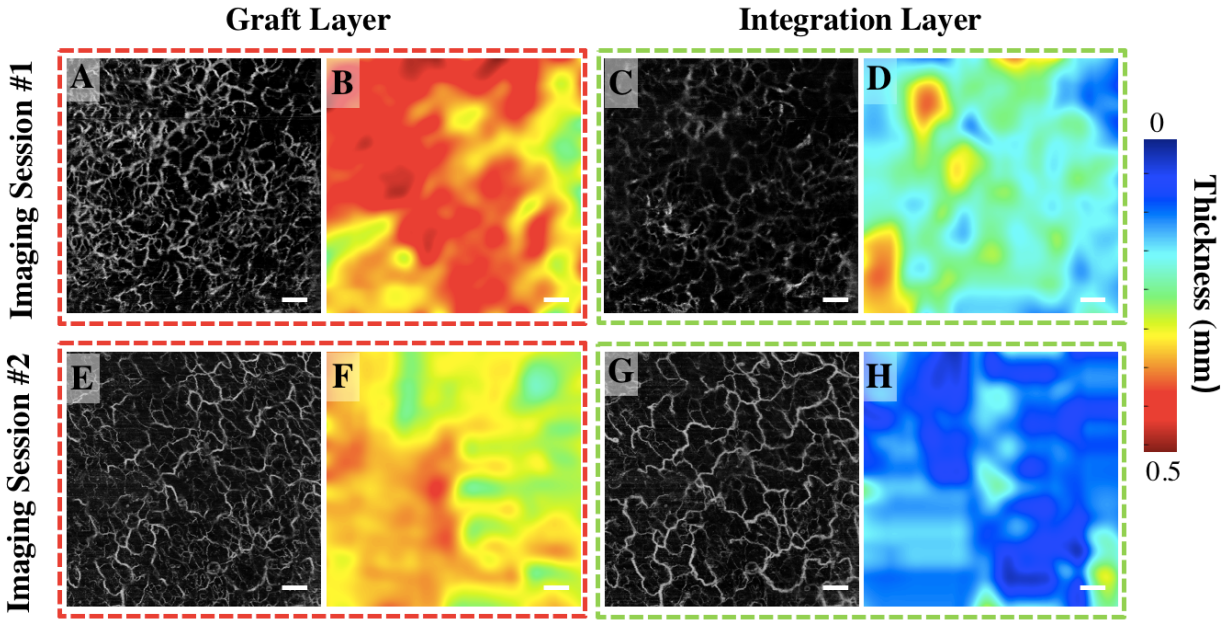

Fig 4.16 En face projected blood vessel and layer thickness maps from patient #1 spanning two imaging sessions. (A, C, E, G) En face projected vasculature maps derived from the graft and integration layers, respectively. (B, D, F, H) Thickness maps derived from the graft and integration layers, respectively. All en face blood vessel images are maximum intensity projected. Color bar presents a depth range of 0 – 0.5 mm. Scale bar represents 1 mm.

Fig 4.17 shows the vascular (through *en face* vessel maps) and structural (through representative cross-sectional B-frames of attenuation correction maps) changes that occurred within and immediately below the graft over the ventrum of the right forearm of patient #2. Fig 4.17 A and E shows the grafted forearm at 6- and 14-days post-surgery, respectively, with approximate scan locations highlighted. Fig 4.17 B alongside a magnified inset, Fig 4.17 C, shows the grafted skin 6-days post-surgery with a sparse density of blood vessels. Clearly visible is a gap between the graft tissue and recipient tissue in the cross-sectional B-frames (Fig 4.17 D). Fig 4.17 F and G shows that the distribution of blood flow 14-days post-surgery is more homogenous compared to the blood flow of 6-days post-surgery. Fig 4.17 H shows that the integration layer is now significantly less obvious in the second imaging session compared to the first. Moreover, Fig 4.17 F presents dark vessel-like structures which are highlighted by the yellow arrow.

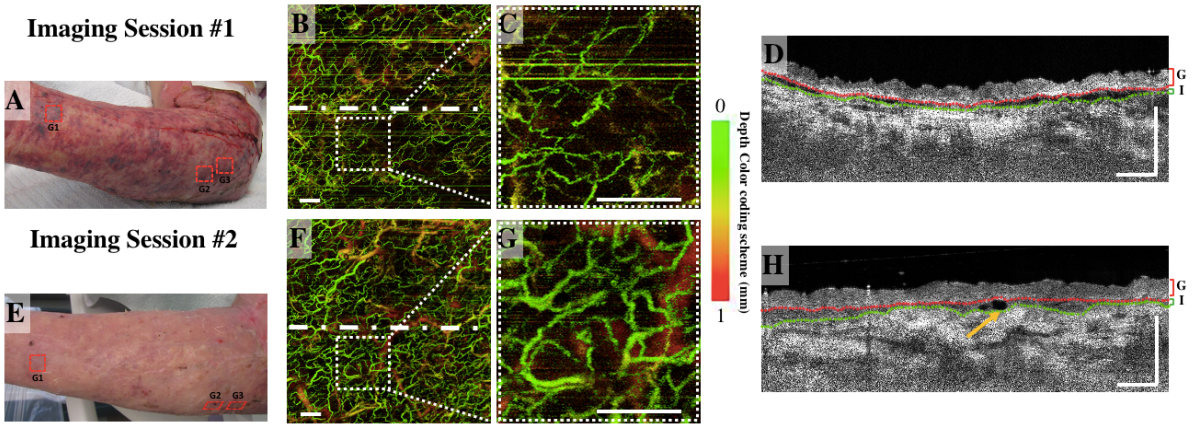

Fig 4.17 En face OCTA images and structural (after attenuation correction processing) cross-sectional B-frames from patient #2. (A, E) showing photographs of the grafted forearm 6-days and 14-days post-surgery, respectively. Highlighted are three scan sites (red perforated boxes) labeled G1, G2, G3. G1 – G3 refer to three graft sites. (B, C, D) showing the graft 6-days post-surgery from scan site G2. (F, G, H) showing the graft 14-days post-surgery from scan site G2. (B, C, F, G) En face projected blood vessel maps with color coded vessel depth. (C, G) Magnified images of the regions highlighted in the dashed rectangles in (B, F). (D, H) Representative cross-sectional B-frames of OCT structure corresponding to the white dashed line in (B, F). All en face images are maximum intensity projected. Color bar represents vessel depth. Scale bar represents 1 mm.

Shown in Fig 4.18 are the same graft scans presented in Fig 4.17 segmented into two layers, i.e. the graft and integration layers, to separately demonstrate the vasculature and thickness maps of each layer. For patient #2, blood vessels were denser in the second imaging session compared to the first for both the graft and integration layers. However, neither the graft nor the integration layer appeared to have changed significantly in terms of thickness between the first and second imaging sessions.

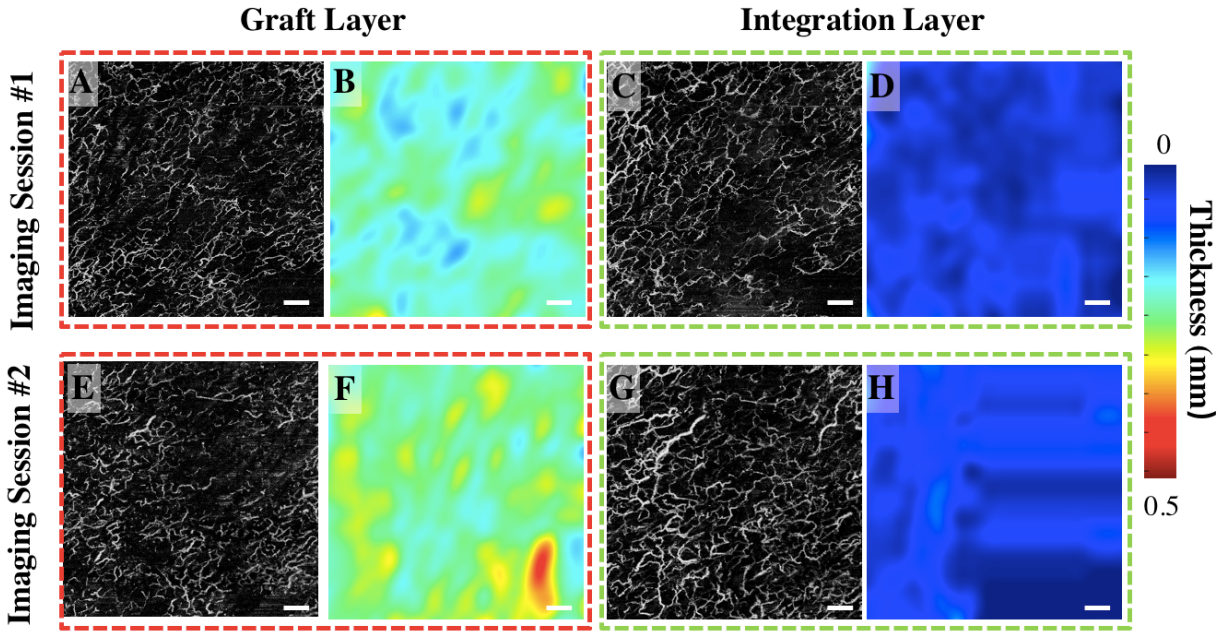

Fig 4.18 En face projected blood vessel and layer thickness maps of patient #2 spanning two imaging sessions. (A, C, E, G) En face projected blood vessel maps derived from the graft and integration layers, respectively. (B, D, F, H) Thickness maps are derived from the graft and integration layers, respectively. All en face blood vessel images are maximum intensity projected. Color bar presents a depth range of 0 – 0.5 mm. Scale bar represents 1 mm.

Table 4.3 shows the detailed quantification results of layer thickness measurements, and vascular area density and diameter measurements from both patients at both time points. Integration layer thickness at the second time point was significantly less than that of the first time point with patient #1 ($P = 0.0047$). Significant growth can be seen for both graft vascular area density ($P = 0.042$) as well as integration layer vascular area density ($P= 0.0052$) between both imaging sessions for patient #2. Vascular diameter within the integration layer of patient #2 also increased significantly between the first and second imaging sessions ($P = 0.042$).

Table 4.3 Quantitative analysis of layer thickness and vascular parameter measurements.

Groups		Session #1 (N=3) Mean ± SD	Session #2 (N=3) Mean ± SD	*P* value
Patient #1	Graft Layer Thickness(μm)	364.5 ± 38.6	335.0 ± 42.5	0.64
	Integration Layer Thickness(μm)	235.5 ± 17.9	114.8 ± 11.4	0.0047**
	Graft Layer Vessel Area Density	0.36 ± 0.017	0.37 ± 0.027	0.79
	Integration Layer Vessel Area Density	0.29 ± 0.0054	0.35± 0.044	0.29
	Graft Layer Vascular Diameter(μm)	37.0 ± 2.5	37.3 ± 1.3	0.94
	Integration Layer Vascular Diameter(μm)	35.4 ± 1.6	39.7± 2.1	0.20
Patient #2	Graft Layer Thickness(μm)	285.1 ± 41.2	311.3 ± 20.4	0.61
	Integration Layer Thickness(μm)	72.5 ± 13.9	104.4 ± 19.1	0.25
	Graft Layer Vessel Area Density	0.30 ± 0.011	0.35 ± 0.011	0.042*
	Integration Layer Vessel Area Density	0.28 ± 0.0079	0.35 ± 0.0078	0.0052**
	Graft Layer Vascular Diameter(μm)	31.4 ± 1.9	36.1 ± 1.3	0.11
	Integration Layer Vascular Diameter(μm)	30.5 ± 2.6	39.1 ± 1.3	0.042*

P values were obtained by two sample t-tests

4.3.4 Discussion and conclusions

Skin autografting has been clinically used worldwide as a treatment strategy for numerous conditions including burns, soft tissue wounds, and cancer. However, there is still a failure rate of 10-30% (195). Few studies have been conducted to monitor the wound healing, integration and maturation process of a skin graft. Therefore, the need for an accurate, non-invasive imaging tool to evaluate graft health and integration remains. To the best of our knowledge, the work presented in this study demonstrates for the very first time the ability of OCT and OCTA to image and monitor the health and integration of autologous human skin

grafts following split thickness skin graft surgery. Two patients were imaged separately post-surgery at two time points. Alterations to the graft tissue itself and the tissue immediately beneath the graft tissue, referred to here as the integration layer, were monitored through the vascular (via blood vessel mapping) and structural (via attenuation correction mapping) features of both tissue layers.

The importance of graft revascularization for graft survival has been noted previously (196); accordingly, we aimed to utilize a non-invasive imaging modality capable of assessing skin features for evaluating graft health. As mentioned above, OCTA detects functional blood vessels by identifying differences between moving particles in the blood, i.e., red blood cells, and the surrounding static tissue. That is, OCTA would not detect the flow if there were no blood flow in the blood vessels or the blood flow is too slow that is below its detection limit (typically less than ~ 10 μm/s). A skin graft initially does not have its own blood supply; therefore, theoretically we should not observe any blood flow immediately after surgery. Blood flow was observed in the graft and integration layers from both patients at the first imaging session, which indicates that patient #1 and patient #2 had realized revascularization 7- and 6-days post-surgery, respectively. This is consistent with the theory that revascularization takes 3 – 7 days after surgery. This also proves the ability of OCT/OCTA to evaluate revascularization of a skin graft. There are two main hypotheses regarding the processes of the revascularization: 1) that graft vessels link to the existing wound tissue bed directly; and 2) that new vessels grow into the graft from the wound bed beneath, i.e. angiogenesis (197). With the exact mechanism behind skin graft revascularization not yet being fully understood, OCT/OCTA could become an important tool to explore the mechanisms and dynamics of early vessel transformation. In addition, significant growth was observed both in graft vascular area density ($P = 0.042$) and integration layer vascular area density ($P= 0.0052$) between the two imaging points from patient #2, indicating further revascularization of skin grafts over time. Visually, epidermal thickening, a common feature of a graft with edema (198), was evident in patient #1 as seen in the graft cross-sectional B-frame images (Fig 4.15 A), which partially subsided later (Fig 4.15 C). The edema is thought to result from lymphatic dysfunction (199) and inflammation. Lymphangiogenesis later contributes to the edema reduction (196). Dark vessel-like structures were visualized during the second imaging session for patient #2 (Fig 4.17 H). Patient #1 too showed dark-vessel structures in both the graft layer and integration layer during the second imaging session, but for patient #1, these structures were not as evident as patient #2. These structures are thought to be lymphatic vessels, because lymph fluid is almost transparent, allowing lymphatic vessels to appear as dark regions (low scattering intensity) with vessel-like shapes in the OCT images. In this way, OCT may be used to provide evidence of lymphangiogenesis in terms of direct structural images and edema reduction.

Whilst both patients imaged offered an informative glimpse into the vascular and structural features of integrating graft tissue that could potentially allow a clinician or researcher to monitor the various stages of healing, an additional observation is unveiled when we compared data derived from patient #1 with those derived from patient #2. Taking both time points into account, patient #1 had thicker epidermis that lead authors to believe that edema was still present 7-days post-surgery, which then partially subsided 16-days post-surgery. Epidermal thickness for patient #2, however, was notably more stable 6-days post-surgery, as evidenced by the similar measures taken 14-days post-surgery. For patient #1, the thickness of the integration layer was significantly (~50%) reduced in the second imaging session compared to the first (P=0.0047), whilst patient #2 did not due to an already thinned integration layer during first time imaging session. This may be due to several complications that arose in the days initially following surgery for patient #1, which may mean additional blebbing was required: thus, maintaining patient #1 in an inflamed condition for longer than patient #2. This additional observation highlights the advantages of using non-invasive imaging technology over other invasive modalities; in that, repeated measures can be conducted more easily over time without interfering with the healing process. This allows for a more in-depth assessment of healing.

Overall, these data, although limited, do offer an insight into the vascular and structural features observable via OCT and OCTA that may be useful to a clinician in establishing the integration and maturation progress of grafted skin in the days and weeks following surgery. Additionally, from a clinical standpoint, the potential applications for OCT and OCTA in graft imaging are vast. OCTA, for example, could not only be used to monitor graft integration but to also evaluate donor site vascularity prior to excision and aid with predicting graft survivability. OCTA also shows its potential in evaluating wound healing in burn site. For example, we suspect the vessels shown in Fig 4.17 J are fenestrated vessels surrounding a hair follicle providing the necessary nutrients to accommodate re-epithelialization. This could be argued as a marker for skin healing if identified early enough as this would be a subsurface feature that would predate visible surface healing. The limited number of other non-invasive methods described in the literature (191) are restricted to assessing specific features of the graft alone and cannot assess donor site, integration layer, wound bed tissue, or incomplete graft take. Even from a pre-clinical standpoint, OCT and OCTA can be employed for the assessment of grafting practices and engineered skin tissue substitutes – a growing area of research. Polarization-sensitive OCT (PS-OCT), which is sensitive enough to detect different dermal layers as well as anisotropic biological structures, e.g., collagen -- an important dermis component, and its restoration during wound healing process, would further enhance the use of OCT in skin autograft studies.

Several limitations in this study need to be acknowledged. Firstly, the field of view in this study is limited to 9 × 9 mm, which results in the loss of information outside the field of view. To minimize this bias, we scanned three typical graft sites of each patient instead of a single random graft site. To further address this issue in future studies, some wide field of view technologies, such as laser speckle contrast imaging, could be carried out to guide OCT imaging of the graft sites of interest. Note that the increased scanning speed will provide a larger field of view for the future OCT imaging. Secondly, our study is limited by small samples. It is worthwhile to mention that this study aims to explore the potential of applying OCT/OCTA to visualize and monitor the healing and integration of skin autografts, rather than to prove novel medical discoveries. Certainly, to fully understand skin graft in OCT imaging, large-scale clinical research needs to be conducted in the future.

In summary, OCT/OCTA in this study has shown its potential to image and measure numerous features of human skin graft health and integration in the days and weeks following split-thickness surgery. For the first time, we demonstrate the applicability of non-invasive OCT/OCTA imaging technology for novel clinical uses that could aid in the betterment of surgical practices and clinical outcomes in the future.

5 Summary And Future Work

In this dissertation, I explored the diverse clinical applications of OCT in both ophthalmology and dermatology. This dissertation also included novel algorithms and methods aimed at effectively segmenting epidermal thickness, calcified drusen, and outer retinal layers on OCT imaging.

The opening chapter serves as an introduction to OCT technology, laying the foundation for the ensuing chapters. In Chapter 2, a comprehensive exploration into novel algorithms and methods developed for OCT imaging takes center stage. Initially, we presented a straightforward yet highly effective approach for estimating the optical attenuation coefficient (OAC) from OCT images. OAC not only enhanced OCT imaging contrast but also works as a valuable physical parameter for assessing tissue characteristics since alterations in tissue morphology and content can impact OAC. Building on this, we leveraged the OAC to enhance OCT imaging contrast, leading to the development of algorithms for the more precise and efficient segmentation of epidermal thickness, retinal pigment epithelium (RPE), and calcified drusen. Ultimately, we introduce TransUnet, an innovative deep learning-based method developed to accurately segment the outer retinal layer. Through this progressive exploration of OCT technology and advanced algorithms, our research significantly improved imaging segmentation and analysis in OCT applications. In this chapter,

Building on this foundation, Chapter 3 showcased the remarkable capabilities and potentials of OCT in clinical ophthalmology. Firstly, we investigated the symmetry of interocular choroidal thickness and vascularity index measurements in normal eyes using SS-OCT and found that choroidal differences existed between normal fellow eyes in adults in the absence of obvious pathology. This study is useful in assisting clinicians and researchers in distinguishing asymmetric changes that are to be expected in normal eyes versus changes that could be associated with diseases. Secondly, to investigate whether the outer retinal layer (ORL) thickness could serve as a useful biomarker for predicting the progression of AMD, we examined variations in ORL thickness among different stages of AMD, including 80 normal eyes, 30 eyes with intermediate AMD displaying reticular pseudodrusen only, 49 eyes with intermediate AMD displaying soft drusen only, and 40 eyes with late AMD accompanied by geographic atrophy (GA). Significant differences in ORL thickness measurements were found among different AMD stages, indicating the potential of ORL thickness as an independent biomarker for predicting AMD progression.

Lastly, in Chapter 4, I discussed the clinical applications of OCT for dermatology. Firstly, we integrated pressure sensors with handheld probe to facilitate imaging of micro vasculature. OCT and OCTA have been increasingly applied in skin imaging applications in dermatology, where the imaging is often performed with the OCT probe in contact with the skin surface. However, this contact mode imaging can introduce uncontrollable mechanical stress applied to the skin, inevitably complicating the interpretation of OCT/OCTA imaging results. There remains a need for a strategy for assessing local pressure applied on the skin during imaging acquisition. This study reports a handheld scanning probe integrated with built-in pressure sensors, allowing the operator to control the mechanical stress applied to the skin in real-time. With real time feedback information, the operator can easily determine whether the pressure applied to the skin would affect the imaging quality so as to obtain repeatable and reliable OCTA images for a more accurate investigation of skin conditions. Secondly, we imaged seven patients with severe burn wounds using an in-house-built, clinical-prototype OCT system. *En face* vascular and surface topography maps demonstrated numerous morphological changes over both imaging sessions associated with burn injury, such as altered blood flow and loss of regular texture. Variations in vascular area density and roughness measurements within the burn wounds revealed by OCT offer some key insights into the underlying pathophysiological mechanisms responsible for wound healing, which may become critical biological indicators in future clinical evaluation and monitoring of wound healing. Thirdly, to demonstrate the potential of OCT alongside OCTA to non-invasively image and monitor human skin graft health and integration over time, two patients (patient #1 and #2) who underwent split-thickness skin graft surgery following severe burn damage to the skin were enrolled for this preliminary study. Vascular and structural features were successfully imaged and measured in the graft tissue and integration layer immediately

beneath at different time points. Revascularization, healing, and integration were monitored with patient-specific details. This preliminary study shows that OCT/OCTA has clinical potential to image and measure numerous features of human skin graft health and integration in the days and weeks following split-thickness surgery.

A portion of this dissertation has been featured in the selected journal papers listed below, with detailed contributions summarized at the conclusion of each respective paper.

*: Equally Contributed Authors.

[1] Assessing Age-related Macular Degeneration (AMD) Progression through Automated Segmentation of the Outer Retinal Layer using Deep Learning (Under review)
Jie Lu, Jinpeng Liao, Yuxuan Cheng, Farhan E. Hiya, Mengxi Shen, Gissel Herrera, Qinqin Zhang, Giovanni Gregori, Philip J. Rosenfeld, Ruikang K. Wang
Jie Lu's contribution: *Research Design, Data Analysis and Interpretation, Writing and Editing*

[2] Automated segmentation and quantification of calcified drusen in 3D swept source OCT imaging
Jie Lu, Yuxuan Cheng, Jianqing Li, Ziyu Liu, Mengxi Shen, Qinqin Zhang, Jeremy Liu, Gissel Herrera, Farhan E Hiya, Rosalyn Morin, Joan Joseph, Giovanni Gregori, Philip J Rosenfeld, Ruikang K Wang in Biomedical Optics Express, Feb 2023.
Jie Lu's contribution: *Research Design, Data Analysis and Interpretation, Writing and Editing*

[3] The DERMIS Study: Evaluation of Insulin Pump Infusion Sites in Type 1 Diabetes
Andrea Kalus, Michi M Shinohara, Ruikang Wang, Jesica D Baran, Xiaofu Dong, Dori Khakpour, **Jie Lu**, Irl B Hirsch, in Available at SSRN 4345818, Feb 2023.
Jie Lu's contribution: *Data collection, Analysis and Interpretation*

[4] Integrating a pressure sensor with an OCT handheld probe to facilitate imaging of microvascular information in skin tissue beds.
Yaping Shi*, **Jie Lu***, Nhan Le, and Ruikang Wang in Biomedical Optics Express, Nov 2022.
Jie Lu's contribution: *Research Design, Data Analysis and Interpretation, Writing and Editing*

[5] Semisupervised representative learning for measuring epidermal thickness in human subjects in optical coherence tomography by leveraging datasets from rodent models

Yubo Ji, Shufan Yang, Kanheng Zhou, **Jie Lu**, Ruikang Wang, Holly R Rocliffe, Antonella Pellicoro, Jenna L Cash, Chunhui Li, Zhihong Huang in Journal of Biomedical
Optics, Aug 2022.
Jie Lu's contribution: *Data Collection*

[6] Local axis orientation mapped by polarization sensitive optical coherence tomography provides a unique contrast to identify caries lesions in enamel
Peijun Tang, Nhan Le, **Jie Lu**, Kwok-Hung Chung, Hrebesh Subhash, LaTonya Kilpatrick Liverman, and Ruikang K. Wang, in Biomedical Optics Express, Jul 2022.
Jie Lu's contribution: *Data Collection and analysis*

[7] A novel deep learning method for choroidal-scleral junction segmentation
Homayoun Bagherinia, Lars Omlor, Luis De Sisternes, Hao Zhou, **Jie Lu**, Yingying Shi, Philip J Rosenfeld, Ruikang K Wang, in Investigative Ophthalmology and Visual
Science, Jun 2022.
Jie Lu's contribution: *Data annotation*

[8] Mitigating the effects of choroidal hyper-and hypo-transmission defects on choroidal vascularity index assessments using optical coherence tomography
Hao Zhou, **Jie Lu**, Kelly Chen, Yingying Shi, Giovanni Gregori, Philip J Rosenfeld, Ruikang K Wang, in Quantitative imaging in medicine and surgery, May 2022.
Jie Lu's contribution: *Data Analysis and Interpretation*

[9] Intraoral optical coherence tomography and angiography combined with autofluorescence for dental assessment
Nhan Le*, **Jie Lu*,** Peijun Tang, Kwok-Hung Chung, Hrebesh Subhash, LaTonya Kilpatrick- Liverman, Ruikang K Wang, in Biomedical Optics Express, May 2022.
Jie Lu's contribution: *Research Design, Writing and Editing*

[10] Interocular asymmetry of choroidal thickness and vascularity index measurements in normal eyes assessed by swept-source optical coherence tomography
Jie Lu, Hao Zhou, Yingying Shi, James Choe, Mengxi Shen, Liang Wang, Kelly Chen, Qinqin Zhang, William J Feuer, Giovanni Gregori, Philip J Rosenfeld, Ruikang K Wang, in Quantitative imaging in medicine and surgery, Jan 2022.

Jie Lu's contribution: *Research Design, Data Analysis and Interpretation, Writing and Editing*

[11] Analyzing automated OCT choroid thickness measurements
Luis De Sisternes, Homayoun Bagherinia, Hao Zhou, **Jie Lu**, Warren Lewis, Sophie Kubach, Yingying Shi, Philip J Rosenfeld, Ruikang Wang, Mary Kathryn Durbin in Investigative ophthalmology and visual science, Aug 2021.
Jie Lu's contribution: *Data annotation*

[12] Accurate measurement of choroidal vascularity index in eyes with hyper/hypo transmission defects using SS-OCT
Luis De Sisternes, Homayoun Bagherinia, Hao Zhou, **Jie Lu**, Warren Lewis, Sophie Kubach, Yingying Shi, Philip J Rosenfeld, Ruikang Wang, Mary Kathryn Durbin in Investigative Ophthalmology and Visual Science, Aug 2021.
Jie Lu's contribution: *Data analysis*

[13] OCT-Based Angiography and Surface Topography in Burn-Damaged Skin
Jie Lu, Anthony J Deegan, Yuxuan Cheng, Samuel P Mandell, Ruikang K Wang, in Lasers in Surgery and Medicine, Aug 2021.
Jie Lu's contribution: *Research Design, Data Analysis and Interpretation, Writing and Editing*

[14] Accurate measurement of choroidal vascularity index in eyes with hyper/hypo transmission defects using SS-OCT
Hao Zhou, **Jie Lu**, Kelly Chen, Yingying Shi, Giovanni Gregori, Philip J Rosenfeld, Ruikang Wang, in Investigative Ophthalmology and Visual Science, Aug 2021.
Jie Lu's contribution: *Data Analysis*

[15] Application of OCT-Derived Attenuation Coefficient in Acute Burn-Damaged Skin (Editor's Choice)
Jie Lu, Anthony J Deegan, Yuxuan Cheng, Teng Liu, Yujiao Zheng, Samuel P Mandell, Ruikang K Wang in Lasers in Surgery and Medicine, May 2021.
Jie Lu's contribution: *Research Design, Data Analysis and Interpretation, Writing and Editing*

[16] Imaging human skin autograft integration with optical coherence tomography

Anthony J Deegan*, **Jie Lu***, Rajendra Sharma, Samuel P Mandell, Ruikang K Wang in Quantitative Imaging in Medicine and Surgery, Feb 2021.
Jie Lu's contribution: *Research Design, Data Analysis and Interpretation, Writing and Editing*

The above studies have significantly demonstrated the capability of OCT in ophthalmology and burn wound healing. Several further improvements are worth exploring. First, the initial study focused on integrating a pressure sensor with an OCT handheld probe to investigate its impact solely on OCTA imaging. It is widely acknowledged that compressing a sample lead to increased scattering, attributed to the gradient of the refractive index shrinking between scatters along the axial dimensions. The OCT signal effectively captures the pressure-enhanced scattering, consequently affecting the measurements of OAC. By employing the pressure sensor's guidance, OAC can be analyzed and compared at various pressure levels, thereby enabling the elimination of potential complications arising from the contact effect during result interpretation. Consequently, this approach enhances the accuracy of the OAC results obtained. Second, the study focusing on ORL thickness did not encompass the measurement of other important biomarkers associated with AMD, such as choroid capillary flow deficit, calcified drusen, and hyperreflective foci. In future research, exploring these additional biomarkers alongside changes in ORL thickness would be intriguing. Such investigation would allow us to ascertain the predictive capabilities of these risk factors in anticipating AMD progression, whether utilizing combined biomarkers or individual ones. Establishing these relationships could lead to valuable insights into the early detection and management of AMD. Third, for calcified drusen segmentation, the current development was based on SS-OCT imaging, and it is unknown if the proposed method can be applied to SD-OCT datasets since SD-OCT has a worse sensitivity roll-off along the depth and higher optical scattering property of the RPE complex compared with SS-OCT. In this case, the use of the hypoTD information in the sub-choroid slab, even in the subRPE slab, could be problematic. For the development of an algorithm that would also be applicable to the SD-OCT imaging, we plan to combine traditional computer vison with deep learning methods in the future effort.

6 Bibliography

1. Huang D, Swanson EA, Lin CP, Schuman JS, Stinson WG, Chang W, et al. Optical coherence tomography. Science. 1991 Nov 22;254(5035):1178–81.
2. Tomlins PH, Wang RK. Theory, developments and applications of optical coherence tomography. J Phys D: Appl Phys. 2005 Jul;38(15):2519–35.

3. Kashani AH, Chen CL, Gahm JK, Zheng F, Richter GM, Rosenfeld PJ, et al. Optical coherence tomography angiography: A comprehensive review of current methods and clinical applications. Progress in Retinal and Eye Research. 2017 Sep 1;60:66–100.

4. Adhi M, Duker JS. Optical coherence tomography – current and future applications. Curr Opin Ophthalmol. 2013 May;24(3):213–21.

5. Wong WL, Su X, Li X, Cheung CMG, Klein R, Cheng CY, et al. Global prevalence of age-related macular degeneration and disease burden projection for 2020 and 2040: a systematic review and meta-analysis. Lancet Glob Health. 2014 Feb;2(2): e106-116.

6. Fleckenstein M, Keenan TDL, Guymer RH, Chakravarthy U, Schmitz-Valckenberg S, Klaver CC, et al. Age-related macular degeneration. Nat Rev Dis Primers. 2021 May 6;7(1):31.

7. About SYFOVRETM (pegcetacoplan injection) [Internet]. [cited 2023 May 22]. Available from: https://syfovre.com/about-syfovre/what-is-syfovre

8. Stahl A. The Diagnosis and Treatment of Age-Related Macular Degeneration. Dtsch Arztebl Int. 2020 Jul;117(29–30):513–20.

9. Abdelfattah NS, Zhang H, Boyer DS, Rosenfeld PJ, Feuer WJ, Gregori G, et al. Drusen Volume as a Predictor of Disease Progression in Patients With Late Age-Related Macular Degeneration in the Fellow Eye. Investigative Ophthalmology & Visual Science. 2016 Apr 15;57(4):1839–46.

10. Chu Z, Shi Y, Zhou X, Wang L, Zhou H, Laiginhas R, et al. Optical Coherence Tomography Measurements of the Retinal Pigment Epithelium to Bruch Membrane Thickness Around Geographic Atrophy Correlate With Growth. American Journal of Ophthalmology. 2022 Apr 1;236:249–60.

11. Liu J, Shen M, Laiginhas R, Herrera G, Li J, Shi Y, et al. Onset and Progression of Persistent Choroidal Hypertransmission Defects in Intermediate Age-Related Macular Degeneration: A Novel Clinical Trial Endpoint. Am J Ophthalmol. 2023 Mar 22;254:11–22.

12. Rivail A, Vogl WD, Riedl S, Grechenig C, Coulibaly LM, Reiter GS, et al. Deep survival modeling of longitudinal retinal OCT volumes for predicting the onset of atrophy in patients with intermediate AMD. Biomed Opt Express, BOE. 2023 Jun 1;14(6):2449–64.

13. Liu J, Laiginhas R, Shen M, Shi Y, Li J, Trivizki O, et al. Multimodal Imaging and En Face OCT Detection of Calcified Drusen in Eyes with Age-Related Macular Degeneration. Ophthalmology Science [Internet]. 2022 Jun 1 [cited 2022 May 26];2(2). Available from: https://www.ophthalmologyscience.org/article/S2666-9145(22)00051-3/fulltext

14. Tan ACS, Pilgrim MG, Fearn S, Bertazzo S, Tsolaki E, Morrell AP, et al. Calcified nodules in retinal drusen are associated with disease progression in age-related macular degeneration. Sci Transl Med. 2018 Nov 7;10(466): eaat4544.

15. Hirabayashi K, Yu HJ, Wakatsuki Y, Marion KM, Wykoff CC, Sadda SR. OCT Risk Factors for Development of Atrophy in Eyes with Intermediate Age-Related Macular Degeneration. Ophthalmology Retina [Internet]. 2022 Oct 6 [cited 2022 Dec 7]; Available from: https://www.sciencedirect.com/science/article/pii/S2468653022004869

16. Zhou H, Liu J, Laiginhas R, Zhang Q, Cheng Y, Zhang Y, et al. Depth-resolved visualization and automated quantification of hyperreflective foci on OCT scans using optical attenuation coefficients. Biomed Opt Express. 2022 Aug 1;13(8):4175.

17. Nassisi M, Lei J, Abdelfattah NS, Karamat A, Balasubramanian S, Fan W, et al. OCT Risk Factors for Development of Late Age-Related Macular Degeneration in the Fellow Eyes of Patients Enrolled in the HARBOR Study. Ophthalmology. 2019 Dec 1;126(12):1667–74.

18. Kong M, Kim S, Ham DI. INCIDENCE OF LATE AGE-RELATED MACULAR DEGENERATION IN EYES WITH RETICULAR PSEUDODRUSEN. RETINA. 2019 Oct;39(10):1945.

19. Jaffe GJ, Chakravarthy U, Freund KB, Guymer RH, Holz FG, Liakopoulos S, et al. Imaging Features Associated with Progression to Geographic Atrophy in Age-Related Macular Degeneration: Classification of Atrophy Meeting Report 5. Ophthalmology Retina. 2021 Sep 1;5(9):855–67.

20. Zhou H, Dai Y, Shi Y, Russell JF, Lyu C, Noorikolouri J, et al. Age-related changes in choroidal thickness and the volume of vessels and stroma using swept-source OCT and fully automated algorithms. Ophthalmol Retina. 2020 Feb;4(2):204–15.

21. Li M, Huisingh C, Messinger J, Dolz-Marco R, Ferrara D, Freund KB, et al. HISTOLOGY OF GEOGRAPHIC ATROPHY SECONDARY TO AGE-RELATED MACULAR DEGENERATION: A Multilayer Approach. RETINA. 2018 Oct;38(10):1937.

22. Dolz-Marco R, Balaratnasingam C, Messinger JD, Li M, Ferrara D, Freund KB, et al. The Border of Macular Atrophy in Age-Related Macular Degeneration: A Clinicopathologic Correlation. Am J Ophthalmol. 2018 Sep;193:166–77.

23. Burns [Internet]. [cited 2023 Jul 13]. Available from: https://www.who.int/news-room/fact-sheets/detail/burns

24. Monstrey S, Hoeksema H, Verbelen J, Pirayesh A, Blondeel P. Assessment of burn depth and burn wound healing potential. Burns. 2008 Sep;34(6):761–9.

25. Kloppenberg FW, Beerthuizen GI, ten Duis HJ. Perfusion of burn wounds assessed by laser doppler imaging is related to burn depth and healing time. Burns. 2001 Jun;27(4):359–63.

26. Hoeksema H, Van de Sijpe K, Tondu T, Hamdi M, Van Landuyt K, Blondeel P, et al. Accuracy of early burn depth assessment by laser Doppler imaging on different days post burn. Burns. 2009 Feb;35(1):36–45.

27. Gill P. The critical evaluation of laser Doppler imaging in determining burn depth. Int J Burns Trauma. 2013;3(2):72–7.

28. Drexler W, Morgner U, Kärtner FX, Pitris C, Boppart SA, Li XD, et al. In vivo ultrahigh-resolution optical coherence tomography. Opt Lett, OL. 1999 Sep 1;24(17):1221–3.

29. Wojtkowski M, Srinivasan V, Ko T, Fujimoto J, Kowalczyk A, Duker J. Ultrahigh-resolution, high-speed, Fourier domain optical coherence tomography and methods for dispersion compensation. Opt Express. 2004 May 31;12(11):2404–22.

30. Leitgeb R, Hitzenberger CK, Fercher AF. Performance of fourier domain vs. time domain optical coherence tomography. Opt Express, OE. 2003 Apr 21;11(8):889–94.

31. Choma M, Sarunic M, Yang C, Izatt J. Sensitivity advantage of swept source and Fourier domain optical coherence tomography. Opt Express. 2003 Sep 8;11(18):2183–9.

32. Swanson EA, Fujimoto JG. The ecosystem that powered the translation of OCT from fundamental research to clinical and commercial impact [Invited]. Biomed Opt Express. 2017 Feb 21;8(3):1638–64.

33. Ronald Bracewell. The Fourier Transform And Its Applications Bracewell [Internet]. 2000 [cited 2023 Jul 6]. Available from: http://archive.org/details/TheFourierTransformAndItsApplicationsBracewell

34. Xu J, Song S, Men S, Wang RK. Long ranging swept-source optical coherence tomography-based angiography outperforms its spectral-domain counterpart in imaging human skin microcirculations. JBO. 2017 Nov;22(11):116007.

35. Chen CL, Wang RK. Optical coherence tomography based angiography [Invited]. Biomed Opt Express, BOE. 2017 Feb 1;8(2):1056–82.

36. Vermeer KA, Mo J, Weda JJA, Lemij HG, Boer JF de. Depth-resolved model-based reconstruction of attenuation coefficients in optical coherence tomography. Biomed Opt Express, BOE. 2014 Jan 1;5(1):322–37.

37. Baran U, Zhu W, Choi WJ, Omori M, Zhang W, Alkayed NJ, et al. Automated segmentation and enhancement of optical coherence tomography-acquired images of rodent brain. Journal of Neuroscience Methods. 2016 Sep 1;270:132–7.

38. Zhou H, Chu Z, Zhang Q, Dai Y, Gregori G, Rosenfeld PJ, et al. Attenuation correction assisted automatic segmentation for assessing choroidal thickness and vasculature with swept-source OCT. Biomed Opt Express, BOE. 2018 Dec 1;9(12):6067–80.

39. Lister T, Wright PA, Chappell PH. Optical properties of human skin. JBO. 2012 Sep;17(9):090901.

40. McGrath JA, Uitto J. Anatomy and Organization of Human Skin. In: Rook's Textbook of Dermatology [Internet]. John Wiley & Sons, Ltd; 2010 [cited 2021 Feb 18]. p. 1–53. Available from: https://onlinelibrary.wiley.com/doi/abs/10.1002/9781444317633.ch3

41. Faber DJ, Meer FJ van der, Aalders MCG, Leeuwen TG van. Quantitative measurement of attenuation coefficients of weakly scattering media using optical coherence tomography. Opt Express, OE. 2004 Sep 20;12(19):4353–65.

42. Eming SA, Martin P, Tomic-Canic M. Wound repair and regeneration: Mechanisms, signaling, and translation. Sci Transl Med. 2014 Dec 3;6(265):265sr6.

43. Diegelmann RF, Evans MC. Wound healing: an overview of acute, fibrotic and delayed healing. Front Biosci. 2004 Jan 1;9:283–9.

44. Lindert J, Tafazzoli-Lari K, Tüshaus L, Larsen B, Bacia A, Bouteleux M, et al. Optical coherence tomography provides an optical biopsy of burn wounds in children—a pilot study. JBO. 2018 Oct;23(10):106005.

45. Kim KH, Pierce MC, Maguluri GN, Park BH, Yoon SJ, Lydon M, et al. In vivo imaging of human burn injuries with polarization-sensitive optical coherence tomography. JBO. 2012 Jun;17(6):066012.

46. Evans ND, Oreffo ROC, Healy E, Thurner PJ, Man YH. Epithelial mechanobiology, skin wound healing, and the stem cell niche. Journal of the Mechanical Behavior of Biomedical Materials. 2013 Dec 1;28:397–409.

47. Weissman J, Hancewicz T, Kaplan P. Optical coherence tomography of skin for measurement of epidermal thickness by shapelet-based image analysis. Opt Express, OE. 2004 Nov 15;12(23):5760–9.

48. Neerken S, Lucassen GW, Bisschop MA, Lenderink E, Nuijs TAM. Characterization of age-related effects in human skin: A comparative study that applies confocal laser scanning microscopy and optical coherence tomography. JBO. 2004 Mar;9(2):274–81.

49. Hori Y, Yasuno Y, Sakai S, Matsumoto M, Sugawara T, Madjarova VD, et al. Automatic characterization and segmentation of human skin using three-dimensional optical coherence tomography. Opt Express, OE. 2006 Mar 6;14(5):1862–77.

50. Josse G, George J, Black D. Automatic measurement of epidermal thickness from optical coherence tomography images using a new algorithm. Skin Res Technol. 2011 Aug;17(3):314–9.

51. Li A, Cheng J, Yow AP, Wall C, Wong DWK, Tey HL, et al. Epidermal segmentation in high-definition optical coherence tomography. In: 2015 37th Annual International Conference of the IEEE Engineering in Medicine and Biology Society (EMBC). 2015. p. 3045–8.

52. Gong P, Almasian M, Soest G van, Bruin DM de, Leeuwen TG van, Sampson DD, et al. Parametric imaging of attenuation by optical coherence tomography: review of models, methods, and clinical translation. JBO. 2020 Apr;25(4):040901.

53. Roshangar L, Soleimani Rad J, Kheirjou R, Reza Ranjkesh M, Ferdowsi Khosroshahi A. Skin Burns: Review of Molecular Mechanisms and Therapeutic Approaches. Wounds. 2019 Dec;31(12):308–15.

54. Gregori G, Wang F, Rosenfeld PJ, Yehoshua Z, Gregori NZ, Lujan BJ, et al. Spectral Domain Optical Coherence Tomography Imaging of Drusen in Nonexudative Age-Related Macular Degeneration. Ophthalmology. 2011 Jul 1;118(7):1373–9.

55. Suzuki M, Curcio CA, Mullins RF, Spaide RF. Refractile drusen: Clinical Imaging and Candidate Histology. Retina. 2015 May;35(5):859–65.

56. Laiginhas R, Liu J, Shen M, Shi Y, Trivizki O, Waheed NK, et al. Multimodal Imaging, OCT B-Scan Localization, and En Face OCT Detection of Macular Hyperpigmentation in Eyes with Intermediate Age-Related Macular Degeneration. Ophthalmology Science [Internet]. 2022 Jun 1 [cited 2022 May 26];2(2). Available from: https://www.ophthalmologyscience.org/article/S2666-9145(22)00005-7/fulltext

57. Chu Z, Wang L, Zhou X, Shi Y, Cheng Y, Laiginhas R, et al. Automatic geographic atrophy segmentation using optical attenuation in OCT scans with deep learning. Biomed Opt Express. 2022 Mar 1;13(3):1328–43.

58. Laiginhas R, Liu J, Shen M, Shi Y, Trivizki O, Waheed NK, et al. Multimodal Imaging, OCT B-Scan Localization, and En face OCT Detection of Macular Hyperpigmentation in Eyes with Intermediate AMD. Investigative Ophthalmology & Visual Science. 2022 Jun 1;63(7):2318.

59. Okuwobi IP, Ji Z, Fan W, Yuan S, Bekalo L, Chen Q. Automated Quantification of Hyperreflective Foci in SD-OCT With Diabetic Retinopathy. IEEE Journal of Biomedical and Health Informatics. 2020 Apr;24(4):1125–36.

60. Niu S, de Sisternes L, Chen Q, Leng T, Rubin DL. Automated geographic atrophy segmentation for SD-OCT images using region-based C-V model via local similarity factor. Biomed Opt Express. 2016 Jan 20;7(2):581–600.

61. Ramsey DJ, Sunness JS, Malviya P, Applegate C, Hager GD, Handa JT. Automated image alignment and segmentation to follow progression of geographic atrophy in age-related macular degeneration. Retina. 2014 Jul;34(7):1296–307.

62. Ji Z, Chen Q, Niu S, Leng T, Rubin DL. Beyond Retinal Layers: A Deep Voting Model for Automated Geographic Atrophy Segmentation in SD-OCT Images. Translational Vision Science & Technology. 2018 Jan 2;7(1):1.

63. Xu R, Niu S, Chen Q, Ji Z, Rubin D, Chen Y. Automated geographic atrophy segmentation for SD-OCT images based on two-stage learning model. Computers in Biology and Medicine. 2019 Feb 1;105:102–11.

64. Keenan TD, Dharssi S, Peng Y, Chen Q, Agrón E, Wong WT, et al. A Deep Learning Approach for Automated Detection of Geographic Atrophy from Color Fundus Photographs. Ophthalmology. 2019 Nov;126(11):1533–40.

65. Hu Z, Wang Z, Sadda SR. Automated segmentation of geographic atrophy using deep convolutional neural networks. In: Medical Imaging 2018: Computer-Aided Diagnosis [Internet]. SPIE; 2018 [cited 2022 Oct 5]. p. 229–37. Available from: https://www.spiedigitallibrary.org/conference-proceedings-of-spie/10575/1057511/Automated-segmentation-of-geographic-atrophy-using-deep-convolutional-neural-networks/10.1117/12.2287001.full

66. Wu M, Cai X, Chen Q, Ji Z, Niu S, Leng T, et al. Geographic atrophy segmentation in SD-OCT images using synthesized fundus autofluorescence imaging. Comput Methods Programs Biomed. 2019 Dec;182:105101.

67. Varga L, Kovács A, Grósz T, Thury G, Hadarits F, Dégi R, et al. Automatic segmentation of hyperreflective foci in OCT images. Comput Methods Programs Biomed. 2019 Sep;178:91–103.

68. Mukherjee S, De Silva T, Grisso P, Wiley H, Tiarnan DLK, Thavikulwat AT, et al. Retinal layer segmentation in optical coherence tomography (OCT) using a 3D deep-convolutional regression network for patients with age-related macular degeneration. Biomed Opt Express. 2022 May 5;13(6):3195–210.

69. Gijbels I, Prosdocimi I. Loess. WIREs Computational Statistics. 2010;2(5):590–9.

70. Zhou H, Dai Y, Gregori G, Rosenfeld PR, Duncan JL, Schwartz DM, et al. Automated morphometric measurement of the retinal pigment epithelium complex and choriocapillaris using swept source OCT. Biomed Opt Express. 2020 Mar 6;11(4):1834–50.

71. Ouyang Y, Heussen FM, Hariri A, Keane PA, Sadda SR. Optical coherence tomography-based observation of the natural history of drusenoid lesion in eyes with dry age-related macular degeneration. Ophthalmology. 2013 Dec;120(12):2656–65.

72. Byon I, Ji Y, Alagorie AR, Tiosano L, Sadda SR. Topographic assessment of choriocapillaris flow deficits in the intermediate age-related macular degeneration eyes with hyporeflective cores inside drusen. Retina. 2021 Feb 1;41(2):393–401.

73. Zhang Q, Shi Y, Shen M, Cheng Y, Zhou H, Feuer W, et al. Does the Outer Retinal Thickness Around Geographic Atrophy Represent Another Clinical Biomarker for Predicting Growth? American Journal of Ophthalmology. 2022 Dec 1;244:79–87.

74. Gawish A, Fieguth P, Marschall S, Bizheva K. Undecimated hierarchical active contours for oct image segmentation. In: 2014 IEEE International Conference on Image Processing (ICIP). 2014. p. 882–6.

75. Hussain MdA, Bhuiyan A, Ramamohanarao K. Disc segmentation and BMO-MRW measurement from SD-OCT image using graph search and tracing of three bench mark reference layers of retina. In: 2015 IEEE International Conference on Image Processing (ICIP). 2015. p. 4087–91.

76. Chiu SJ, Izatt JA, O'Connell RV, Winter KP, Toth CA, Farsiu S. Validated Automatic Segmentation of AMD Pathology Including Drusen and Geographic Atrophy in SD-OCT Images. Investigative Ophthalmology & Visual Science. 2012 Jan 5;53(1):53–61.

77. Stankiewicz A, Marciniak T, Dąbrowski A, Stopa M, Rakowicz P, Marciniak E. Improving Segmentation of 3D Retina Layers Based on Graph Theory Approach for Low Quality OCT Images. Metrology and Measurement Systems [Internet]. 2016 [cited 2023 Jun 5];Vol. 23(nr 2). Available from: http://yadda.icm.edu.pl/baztech/element/bwmeta1.element.baztech-551b9f3e-6602-4005-8f3b-1535e9ddfaa6

78. Mishra Z, Ganegoda A, Selicha J, Wang Z, Sadda SR, Hu Z. Automated Retinal Layer Segmentation Using Graph-based Algorithm Incorporating Deep-learning-derived Information. Sci Rep. 2020 Jun 12;10:9541.

79. Gopinath K, Rangrej SB, Sivaswamy J. A Deep Learning Framework for Segmentation of Retinal Layers from OCT Images. In: 2017 4th IAPR Asian Conference on Pattern Recognition (ACPR). 2017. p. 888–93.

80. He Y, Carass A, Liu Y, Jedynak BM, Solomon SD, Saidha S, et al. Structured layer surface segmentation for retina OCT using fully convolutional regression networks. Med Image Anal. 2021 Feb;68:101856.

81. Matovinovic IZ, Loncaric S, Lo J, Heisler M, Sarunic M. Transfer Learning with U-Net type model for Automatic Segmentation of Three Retinal Layers In Optical Coherence Tomography Images. In: 2019 11th International Symposium on Image and Signal Processing and Analysis (ISPA). 2019. p. 49–53.

82. Asgari R, Waldstein S, Schlanitz F, Baratsits M, Schmidt-Erfurth U, Bogunović H. U-Net with Spatial Pyramid Pooling for Drusen Segmentation in Optical Coherence Tomography. In: Fu H, Garvin MK, MacGillivray T, Xu Y, Zheng Y, editors. Ophthalmic Medical Image Analysis. Cham: Springer International Publishing; 2019. p. 77–85. (Lecture Notes in Computer Science).

83. Viedma IA, Alonso-Caneiro D, Read SA, Collins MJ, Hoseini-Yazdi H. A deep learning multi-capture segmentation modality for retinal OCT imaging. In: 2022 International Conference on Digital Image Computing: Techniques and Applications (DICTA). 2022. p. 1–8.

84. Zhang Y, Li Z, Nan N, Wang X. TranSegNet: Hybrid CNN-Vision Transformers Encoder for Retina Segmentation of Optical Coherence Tomography. Life (Basel). 2023 Apr 10;13(4):976.

85. Shah A, Zhou L, Abrámoff MD, Wu X. Multiple surface segmentation using convolution neural nets: application to retinal layer segmentation in OCT images. Biomed Opt Express. 2018 Aug 29;9(9):4509–26.

86. Long J, Shelhamer E, Darrell T. Fully Convolutional Networks for Semantic Segmentation [Internet]. arXiv; 2015 [cited 2023 Jun 19]. Available from: http://arxiv.org/abs/1411.4038

87. Ronneberger O, Fischer P, Brox T. U-Net: Convolutional Networks for Biomedical Image Segmentation [Internet]. arXiv; 2015 [cited 2023 Jun 19]. Available from: http://arxiv.org/abs/1505.04597

88. Dosovitskiy A, Beyer L, Kolesnikov A, Weissenborn D, Zhai X, Unterthiner T, et al. An Image is Worth 16x16 Words: Transformers for Image Recognition at Scale [Internet]. arXiv; 2021 [cited 2023 Jun 19]. Available from: http://arxiv.org/abs/2010.11929

89. Chen J, Lu Y, Yu Q, Luo X, Adeli E, Wang Y, et al. TransUNet: Transformers Make Strong Encoders for Medical Image Segmentation [Internet]. arXiv; 2021 [cited 2023 Jun 19]. Available from: http://arxiv.org/abs/2102.04306

90. Ehlers JP, Zahid R, Kaiser PK, Heier JS, Brown DM, Meng X, et al. Longitudinal Assessment of Ellipsoid Zone Integrity, Subretinal Hyperreflective Material, and Subretinal Pigment Epithelium Disease in Neovascular Age-Related Macular Degeneration. Ophthalmology Retina. 2021 Dec 1;5(12):1204–13.

91. Mai J, Riedl S, Reiter GS, Lachinov D, Vogl WD, Bogunovic H, et al. Comparison of Fundus Autofluorescence Versus Optical Coherence Tomography–based Evaluation of the Therapeutic Response to Pegcetacoplan in Geographic Atrophy. American Journal of Ophthalmology. 2022 Dec 1;244:175–82.

92. Orlando JI, Gerendas BS, Riedl S, Grechenig C, Breger A, Ehler M, et al. Automated Quantification of Photoreceptor alteration in macular disease using Optical Coherence Tomography and Deep Learning. Sci Rep. 2020 Mar 27;10(1):5619.

93. Gin TJ, Wu Z, Chew SKH, Guymer RH, Luu CD. Quantitative Analysis of the Ellipsoid Zone Intensity in Phenotypic Variations of Intermediate Age-Related Macular Degeneration. Invest Ophthalmol Vis Sci. 2017 Apr 1;58(4):2079–86.

94. Zhao Y, Zhao J, Gu Y, Chen B, Guo J, Xie J, et al. Outer Retinal Layer Thickness Changes in White Matter Hyperintensity and Parkinson's Disease. Frontiers in Neuroscience [Internet]. 2021 [cited 2023 Jun 5];15. Available from: https://www.frontiersin.org/articles/10.3389/fnins.2021.741651

95. Kim BJ, Irwin DJ, Song D, Daniel E, Leveque JD, Raquib AR, et al. Optical coherence tomography identifies outer retina thinning in frontotemporal degeneration. Neurology. 2017 Oct 10;89(15):1604–11.

96. Eliwa TF, Hussein MA, Zaki MA, Raslan OA. OUTER RETINAL LAYER THICKNESS AS GOOD VISUAL PREDICTOR IN PATIENTS WITH DIABETIC MACULAR EDEMA. RETINA. 2018 Apr;38(4):805.

97. Yasin Alibhai A, Or C, Witkin AJ. Swept source optical coherence tomography: a review. Curr Ophthalmol Rep. 2018 Mar 1;6(1):7–16.

98. Al-Haddad C, El Chaar L, Antonios R, El-Dairi M, Noureddin B. Interocular symmetry in macular choroidal thickness in children. Lai TY, editor. Journal of Ophthalmology. 2014 Nov 24;2014:472391.

99. Spaide RF, Koizumi H, Pozzoni MC, Pozonni MC. Enhanced depth imaging spectral-domain optical coherence tomography. Am J Ophthalmol. 2008 Oct;146(4):496–500.

100. Ruiz-Medrano J, Flores-Moreno I, Peña-García P, Montero JA, Duker JS, Ruiz-Moreno JM. Asymmetry in macular choroidal thickness profile between both between both eyes in a healthy population measured by swept-source optical coherence tomography. Retina. 2015 Oct;35(10):2067–73.

101. Kim MS, Lim HB, Lee WH, Kim KM, Nam KY, Kim JY. Wide-field swept-source optical coherence tomography analysis of interocular symmetry of choroidal thickness in healthy young individuals. Invest Ophthalmol Vis Sci. 2021 Mar 1;62(3):5.

102. Yiu G, Pecen P, Sarin N, Chiu SJ, Farsiu S, Mruthyunjaya P, et al. Characterization of the choroid-scleral junction and suprachoroidal layer in healthy individuals on enhanced-depth imaging optical coherence tomography. JAMA Ophthalmol. 2014 Feb;132(2):174–81.

103. Kirby MA, Li C, Choi WJ, Gregori G, Rosenfeld P, Wang R. Why choroid vessels appear dark in clinical OCT images. In: Ophthalmic Technologies XXVIII [Internet]. International Society for Optics and Photonics; 2018 [cited 2021 Jan 28]. p. 1047428. Available from: https://www.spiedigitallibrary.org/conference-proceedings-of-spie/10474/1047428/Why-choroid-vessels-appear-dark-in-clinical-OCT-images/10.1117/12.2291057.short

104. Wang RK, Kirby M, Li C, Choi WJ, Gregori G, Rosenfeld PJ. An explanation for why choroidal blood vessels appear dark on clinical OCT images. Invest Ophthalmol Vis Sci. 2017 Jun 23;58(8):4754–4754.

105. Otsu N. A threshold selection method from gray-level histograms. IEEE Transactions on Systems, Man, and Cybernetics. 1979 Jan;9(1):62–6.

106. Wiley.com [Internet]. [cited 2021 Aug 5]. Design and Analysis of Clinical Experiments | Wiley. Available from: https://www.wiley.com/en-us/Design+and+Analysis+of+Clinical+Experiments+-p-9780471349914

107. Say EAT, Shah SU, Ferenczy S, Shields CL. Vol. 2011, Journal of Ophthalmology. Hindawi; 2011 [cited 2021 Feb 3]. p. e385058 Optical coherence tomography of retinal and choroidal tumors. Available from: https://www.hindawi.com/journals/joph/2011/385058/

108. Joachim N, Colijn JM, Kifley A, Lee KE, Buitendijk GHS, Klein BEK, et al. Five-year progression of unilateral age-related macular degeneration to bilateral involvement: the Three Continent AMD Consortium report. Br J Ophthalmol. 2017 Sep;101(9):1185–92.

109. Gattoussi S, Cougnard-Grégoire A, Korobelnik JF, Rougier MB, Delyfer MN, Schweitzer C, et al. Choroidal thickness, vascular factors, and age-related macular degeneration: the alienor study. RETINA. 2019 Jan;39(1):34–43.

110. Fan D, Hua R. Different imaging characteristics between unilateral and bilateral polypoidal choroidal vasculopathy. Photodiagnosis Photodyn Ther. 2019 Jun;26:1–7.

111. Scassellati-Sforzolini B, Mariotti C, Bryan R, Yannuzzi LA, Giuliani M, Giovannini A. Polypoidal choroidal vasculopathy in Italy. Retina. 2001;21(2):121–5.

112. Orduna E, Sanchez-Cano A, Luesma MJ, Perez-Navarro I, Abecia E, Pinilla I. Interocular symmetry of choroidal thickness and volume in healthy eyes on optical coherence tomography. Ophthalmic Res. 2018;59(2):81–7.

113. Chen FK, Yeoh J, Rahman W, Patel PJ, Tufail A, Cruz LD. Topographic variation and interocular symmetry of macular choroidal thickness using enhanced depth imaging optical coherence tomography. Invest Ophthalmol Vis Sci. 2012 Feb 1;53(2):975–85.

114. Bhayana AA, Kumawat D, Kumar V, Chandra M, Chandra P, Sihota R, et al. Interocular asymmetry in choroidal thickness in healthy Indian population using swept-source optical coherence tomography. Indian J Ophthalmol. 2019 Jul;67(7):1252–3.

115. Manbachi A, Hoi Y, Wasserman BA, Lakatta EG, Steinman DA. On the shape of the common carotid artery, with Implications for blood velocity profiles. Physiol Meas. 2011 Dec;32(12):1885–97.

116. Zeiss CJ, Tu DC, Phan I, Wong R, Treuting PM. 21 - Special Senses: Eye. In: Treuting PM, Dintzis SM, Montine KS, editors. Comparative Anatomy and Histology (Second Edition) [Internet]. San Diego: Academic Press; 2018 [cited 2021 Feb 4]. p. 445–70. Available from: https://www.sciencedirect.com/science/article/pii/B978012802900800021X

117. Wenn CM, Newman DL. Arterial tortuosity. Australas Phys Eng Sci Med. 1990 Jun;13(2):67–70.

118. Kutoglu T, Yalcin B, Kocabiyik N, Ozan H. Vortex veins: anatomic investigations on human eyes. Clin Anat. 2005 May;18(4):269–73.

119. Hiroe T, Kishi S. Dilatation of asymmetric vortex vein in central serous chorioretinopathy. Ophthalmol Retina. 2018 Feb;2(2):152–61.

120. Reiner A, Fitzgerald MEC, Mar ND, Li C. Neural control of choroidal blood flow. Prog Retin Eye Res. 2018 May;64:96–130.

121. Van Allen MW. Collateral Circulation to the Eye in Occlusion of the Internal Carotid Artery: Observations on the Influence of External Carotid Flow on Retinal Artery Pressure. AMA Arch Neurol. 1960 Jan 1;2(1):74.

122. Tamler E, Takahashi E. Collateral circulation to the eye. Am J Ophthalmol. 1961 Sep;52:381–4.

123. Xie Z, Wang G, Cheng Y, Zhang Q, Le MN, Wang RK. Optical coherence tomography angiography measures blood pulsatile waveforms at variable tissue depths. Quant Imaging Med Surg. 2021 Mar;11(3):907–17.

124. Eser I, Durrie DS, Schwendeman F, Stahl JE. Association between ocular dominance and refraction. J Refract Surg. 2008 Sep;24(7):685–9.

125. Ehrenstein WH, Arnold-Schulz-Gahmen BE, Jaschinski W. Eye preference within the context of binocular functions. Graefes Arch Clin Exp Ophthalmol. 2005 Sep;243(9):926–32.

126. Woodman-Pieterse EC, Read SA, Collins MJ, Alonso-Caneiro D. Regional changes in choroidal thickness associated with accommodation. Invest Ophthalmol Vis Sci. 2015 Oct 1;56(11):6414–22.

127. Fujimura F, Handa T, Kawamorita T, Shoji N. The effect of ocular dominance on accommodation and miosis under binocular open viewing conditions. Open Journal of Ophthalmology. 2017 Jul 10;7(3):158–66.

128. Breher K, Ohlendorf A, Wahl S. Myopia induces meridional growth asymmetry of the retina: a pilot study using wide-field swept-source OCT. Scientific Reports. 2020 Jul 2;10(1):10886.

129. Yang M, Wang W, Xu Q, Tan S, Wei S. Interocular symmetry of the peripapillary choroidal thickness and retinal nerve fibre layer thickness in healthy adults with isometropia. BMC Ophthalmol [Internet]. 2016 Oct 19 [cited 2021 Jan 26];16. Available from: https://www.ncbi.nlm.nih.gov/pmc/articles/PMC5069918/

130. Jiang X, Shen M, Wang L, de Sisternes L, Durbin MK, Feuer W, et al. Validation of a Novel Automated Algorithm to Measure Drusen Volume and Area Using Swept Source Optical Coherence Tomography Angiography. Translational Vision Science & Technology. 2021 Apr 14;10(4):11.

131. Toto L, Borrelli E, Mastropasqua R, Antonio LD, Doronzo E, Carpineto P, et al. Association between outer retinal alterations and microvascular changes in intermediate stage age-related macular degeneration: an optical coherence tomography angiography study. British Journal of Ophthalmology. 2017 Jun 1;101(6):774–9.

132. Spaide RF. OUTER RETINAL ATROPHY AFTER REGRESSION OF SUBRETINAL DRUSENOID DEPOSITS AS A NEWLY RECOGNIZED FORM OF LATE AGE-RELATED MACULAR DEGENERATION. RETINA. 2013 Oct;33(9):1800.

133. Steinberg JS, Saßmannshausen M, Fleckenstein M, Fimmers R, Oishi A, Holz FG, et al. Correlation of Partial Outer Retinal Thickness With Scotopic and Mesopic Fundus-Controlled Perimetry in Patients With Reticular Drusen. Am J Ophthalmol. 2016 Aug;168:52–61.

134. Ooto S, Hangai M, Tomidokoro A, Saito H, Araie M, Otani T, et al. Effects of age, sex, and axial length on the three-dimensional profile of normal macular layer structures. Invest Ophthalmol Vis Sci. 2011 Nov 11;52(12):8769–79.

135. Arepalli S, Srivastava SK, Hu M, Kaiser PM, Dukles N, Reese JL, et al. Assessment of inner and outer retinal layer metrics on the Cirrus HD-OCT Platform in normal eyes. PLOS ONE. 2018 Oct 4;13(10):e0203324.

136. Waldstein SM, Vogl WD, Bogunovic H, Sadeghipour A, Riedl S, Schmidt-Erfurth U. Characterization of Drusen and Hyperreflective Foci as Biomarkers for Disease Progression in Age-Related

Macular Degeneration Using Artificial Intelligence in Optical Coherence Tomography. JAMA Ophthalmology. 2020 Jul 1;138(7):740–7.

137. Wang DL, Agee J, Mazzola M, Sacconi R, Querques G, Weinberg AD, et al. Outer Retinal Thickness and Fundus Autofluorescence in Geographic Atrophy. Ophthalmol Retina. 2019 Dec;3(12):1035–44.

138. Le NM, Song S, Zhou H, Xu J, Li Y, Sung CE, et al. A noninvasive imaging and measurement using optical coherence tomography angiography for the assessment of gingiva: An in vivo study. J Biophotonics. 2018 Dec;11(12):e201800242.

139. Ibne Mokbul M. Optical Coherence Tomography: Basic Concepts and Applications in Neuroscience Research. J Med Eng. 2017;2017:3409327.

140. Welzel J. Optical coherence tomography in dermatology: a review. Skin Res Technol. 2001 Feb;7(1):1–9.

141. Xu X, Wang RK. Synergistic effect of hyperosmotic agents of dimethyl sulfoxide and glycerol on optical clearing of gastric tissue studied with near infrared spectroscopy. Phys Med Biol. 2004 Feb 7;49(3):457–68.

142. Wang RK, Tuchin VV. Enhance light penetration in tissue for high resolution optical imaging techniques by the use of biocompatible chemical agents. Journal of X-Ray Science and Technology. 2002 Jan 1;10(3–4):167–76.

143. Gong P, Heiss C, Sampson DM, Wang Q, Yuan Z, Sampson DD. Detection of localized pulsatile motion in cutaneous microcirculation by speckle decorrelation optical coherence tomography angiography. JBO. 2020 Sep;25(9):095004.

144. Gong P, Es'haghian S, Harms KA, Murray A, Rea S, Kennedy BF, et al. Optical coherence tomography for longitudinal monitoring of vasculature in scars treated with laser fractionation. Journal of Biophotonics. 2016;9(6):626–36.

145. Wang-Evers M, Casper MJ, Glahn J, Luo T, Doyle AE, Karasik D, et al. Assessing the impact of aging and blood pressure on dermal microvasculature by reactive hyperemia optical coherence tomography angiography. Sci Rep. 2021 Jun 28;11(1):13411.

146. Parmar S, Khodasevych I, Troynikov O. Evaluation of Flexible Force Sensors for Pressure Monitoring in Treatment of Chronic Venous Disorders. Sensors (Basel). 2017 Aug 21;17(8):1923.

147. Faber GS, Koopman AS, Kingma I, Chang CC, Dennerlein JT, van Dieën JH. Continuous ambulatory hand force monitoring during manual materials handling using instrumented force shoes and an inertial motion capture suit. J Biomech. 2018 Mar 21;70:235–41.

148. Schofield JS, Evans KR, Hebert JS, Marasco PD, Carey JP. The effect of biomechanical variables on force sensitive resistor error: Implications for calibration and improved accuracy. J Biomech. 2016 Mar 21;49(5):786–92.

149. Stassi S, Cauda V, Canavese G, Pirri CF. Flexible Tactile Sensing Based on Piezoresistive Composites: A Review. Sensors (Basel). 2014 Mar 14;14(3):5296–332.

150. documents.pub [Internet]. [cited 2022 Mar 14]. FSR Integration Guide - [PDF Document]. Available from: https://documents.pub/document/fsr-integration-guide.html

151. McNeill J, Crivello M, Mendelson Y, Sen D, Dunn R, Hickle K. Flexible sensor for measurement of skin pressure and temperature in a clinical setting. In: 2016 IEEE SENSORS. 2016. p. 1–3.

152. Baran U, Choi WJ, Li Y, Wang RK. Tail artifact removal in OCT angiography images of rodent cortex. J Biophotonics. 2017 Nov;10(11):1421–9.

153. Chu Z, Lin J, Gao C, Xin C, Zhang Q, Chen CL, et al. Quantitative assessment of the retinal microvasculature using optical coherence tomography angiography. J Biomed Opt. 2016 Jun 1;21(6):66008.

154. Zhao Q, Yang WL, Wang XN, Wang RK, You QS, Chu DZ, et al. Repeatability and Reproducibility of Quantitative Assessment of the Retinal Microvasculature Using Optical Coherence Tomography Angiography Based on Optical Microangiography. Biomedical and Environmental Sciences. 2018 Jun 1;31(6):407–12.

155. Wolak ME, Fairbairn DJ, Paulsen YR. Guidelines for estimating repeatability. Methods in Ecology and Evolution. 2012;3(1):129–37.

156. Sapozhnikova VV, Kuranov RV, Cicenaite I, Esenaliev RO, M.d DSP. Effect on blood glucose monitoring of skin pressure exerted by an optical coherence tomography probe. JBO. 2008 Mar;13(2):021112.

157. Chan EK, Sorg B, Protsenko D, O'Neil M, Motamedi M, Welch AJ. Effects of compression on soft tissue optical properties. IEEE Journal of Selected Topics in Quantum Electronics. 1996 Dec;2(4):943–50.

158. Tang P, Kirby MA, Le N, Li Y, Zeinstra N, Lu GN, et al. Polarization sensitive optical coherence tomography with single input for imaging depth-resolved collagen organizations. Light Sci Appl. 2021 Nov 24;10(1):237.

159. Abraham P, Fromy B, Merzeau S, Jardel A, Saumet JL. Dynamics of local pressure-induced cutaneous vasodilation in the human hand. Microvasc Res. 2001 Jan;61(1):122–9.

160. Murphy-Chutorian B, Han G, Cohen SR. Dermatologic Manifestations of Diabetes Mellitus: A Review. Endocrinology and Metabolism Clinics. 2013 Dec 1;42(4):869–98.

161. Laurent S, Agabiti-Rosei C, Bruno RM, Rizzoni D. Microcirculation and Macrocirculation in Hypertension: A Dangerous Cross-Link? Hypertension. 2022 Mar;79(3):479–90.

162. Bentov I, Reed MJ. The Effect of Aging on the Cutaneous Microvasculature. Microvasc Res. 2015 Jul;100:25–31.

163. Chen CH, Henry PD. Atherosclerosis as a microvascular disease: impaired angiogenesis mediated by suppressed basic fibroblast growth factor expression. Proc Assoc Am Physicians. 1997 Jul;109(4):351–61.

164. Rosenberry R, Nelson MD. Reactive hyperemia: a review of methods, mechanisms, and considerations. Am J Physiol Regul Integr Comp Physiol. 2020 Mar 1;318(3):R605–18.

165. Stano G, Di Nisio A, Lanzolla A, Percoco G. Additive manufacturing and characterization of a load cell with embedded strain gauges. Precision Engineering. 2020 Mar 1;62:113–20.

166. Huang Q, Zhao M, Zhao K. Alteration of vascular permeability in burn injury. MedicalExpress (São Paulo, online). 2014 Apr;1:62–76.

167. Deegan AJ, Wang RK. Microvascular imaging of the skin. Phys Med Biol. 2019 Mar;64(7):07TR01.

168. Olsen J, Holmes J, Jemec GB. Advances in optical coherence tomography in dermatology-a review. J Biomed Opt. 2018 Apr;23(4):1–10.

169. Zhao Y, Maher JR, Kim J, Selim MA, Levinson H, Wax A. Evaluation of burn severity in vivo in a mouse model using spectroscopic optical coherence tomography. Biomed Opt Express. 2015 Aug 13;6(9):3339–45.

170. Lindert J, Tafazzoli-Lari K, Tüshaus L, Larsen B, Bacia A, Bouteleux M, et al. Optical coherence tomography provides an optical biopsy of burn wounds in children-a pilot study. J Biomed Opt. 2018 Oct;23(10):1–6.

171. Deegan AJ, Mandell SP, Wang RK. Optical coherence tomography correlates multiple measures of tissue damage following acute burn injury. Quant Imaging Med Surg. 2019 May;9(5):731–41.

172. Jackson DM. Diagnosis in the Management of Burns. Br Med J. 1959 May 16;1(5132):1263–7.

173. Hettiaratchy S, Dziewulski P. ABC of burns: pathophysiology and types of burns. BMJ. 2004 Jun 12;328(7453):1427–9.

174. Askaruly S, Ahn Y, Kim H, Vavilin A, Ban S, Kim PU, et al. Quantitative Evaluation of Skin Surface Roughness Using Optical Coherence Tomography In Vivo. IEEE J Sel Top Quantum Electron. 2019 Feb;25(1):7202308.

175. Gong P, Es'haghian S, Wood FM, Sampson DD, McLaughlin RA. Optical coherence tomography angiography for longitudinal monitoring of vascular changes in human cutaneous burns. Exp Dermatol. 2016 Sep;25(9):722–4.

176. Mertens DM, Jenkins ME, Warden GD. Outpatient burn management. Nurs Clin North Am. 1997 Jun;32(2):343–64.

177. Amoh Y, Li L, Yang M, Moossa AR, Katsuoka K, Penman S, et al. Nascent blood vessels in the skin arise from nestin-expressing hair-follicle cells. Proc Natl Acad Sci U S A. 2004 Sep 7;101(36):13291–5.

178. Liu JQ, Zhao KB, Feng ZH, Qi FZ. Hair follicle units promote re-epithelialization in chronic cutaneous wounds: A clinical case series study. Exp Ther Med. 2015 Jul;10(1):25–30.

179. Rowan MP, Cancio LC, Elster EA, Burmeister DM, Rose LF, Natesan S, et al. Burn wound healing and treatment: review and advancements. Crit Care. 2015 Jun 12;19:243.

180. Jaspers MEH, Feroldi F, Vlig M, de Boer JF, van Zuijlen PPM. In vivo polarization-sensitive optical coherence tomography of human burn scars: birefringence quantification and correspondence with histologically determined collagen density. J Biomed Opt. 2017 Dec;22(12):1–8.

181. Orgill DP. Excision and skin grafting of thermal burns. N Engl J Med. 2009 Feb 26;360(9):893–901.

182. Johnson TM, Ratner D, Nelson BR. Soft tissue reconstruction with skin grafting. J Am Acad Dermatol. 1992 Aug;27(2 Pt 1):151–65.

183. Ratner D. Skin grafting. Semin Cutan Med Surg. 2003 Dec;22(4):295–305.

184. Achora S, Muliira JK, Thanka AN. Strategies to promote healing of split thickness skin grafts: an integrative review. J Wound Ostomy Continence Nurs. 2014;41(4):335–9; quiz E1-2.

185. Carvalho JCO, Palero JA, Jurna M. Real-time imaging of suction blistering in human skin using optical coherence tomography. Biomed Opt Express. 2015 Dec 1;6(12):4790–5.

186. Dhillon M, Carter CP, Morrison J, Hislop WS, Currie WJR. A comparison of skin graft success in the head & neck with and without the use of a pressure dressing. J Maxillofac Oral Surg. 2015 Jun;14(2):240–2.

187. Erel E, Sinha M, Nancarrow JD. The “pull out” tie-over dressing. J Plast Reconstr Aesthet Surg. 2008;61(4):460–1.

188. Knapik A, Kornmann K, Kerl K, Calcagni M, Contaldo C, Vollmar B, et al. Practice of split-thickness skin graft storage and histological assessment of tissue quality. J Plast Reconstr Aesthet Surg. 2013 Jun;66(6):827–34.

189. Zdichavsky M, Jones JW, Ustuner ET, Ren X, Edelstein J, Maldonado C, et al. Scoring of skin rejection in a swine composite tissue allograft model. J Surg Res. 1999 Jul;85(1):1–8.

190. Stekelenburg CM, Simons JM, Tuinebreijer WE, van Zuijlen PPM. Analyzing contraction of full thickness skin grafts in time: Choosing the donor site does matter. Burns. 2016 Nov;42(7):1471–6.

191. Hauser J, Lehnhardt M, Daigeler A, Langer S, Steinau HU, Vogt PM. Photoplanimetric evaluation and impedance measurement of split-thickness skin grafts: a new model for objective wound-healing assessment in clinical trials. Skin Res Technol. 2009 May;15(2):168–71.

192. Gould DJ, Reece GP. Skin graft vascular maturation and remodeling: a multifractal approach to morphological quantification. Microcirculation. 2012 Oct;19(7):652–63.

193. Timar-Banu O, Beauregard H, Tousignant J, Lassonde M, Harris P, Viau G, et al. Development of noninvasive and quantitative methodologies for the assessment of chronic ulcers and scars in humans. Wound Repair Regen. 2001;9(2):123–32.

194. Reif R, Qin J, An L, Zhi Z, Dziennis S, Wang R. Quantifying optical microangiography images obtained from a spectral domain optical coherence tomography system. Int J Biomed Imaging. 2012;2012:509783.

195. Braza ME, Fahrenkopf MP. Split-Thickness Skin Grafts. In: StatPearls [Internet]. Treasure Island (FL): StatPearls Publishing; 2023 [cited 2023 Jul 14]. Available from: http://www.ncbi.nlm.nih.gov/books/NBK551561/

196. Frueh FS, Sanchez-Macedo N, Calcagni M, Giovanoli P, Lindenblatt N. The Crucial Role of Vascularization and Lymphangiogenesis in Skin Reconstruction. Eur Surg Res. 2018;59(3–4):242–54.

197. Lindenblatt N, Calcagni M, Contaldo C, Menger MD, Giovanoli P, Vollmar B. A new model for studying the revascularization of skin grafts in vivo: the role of angiogenesis. Plast Reconstr Surg. 2008 Dec;122(6):1669–80.

198. Simman R, Phavixay L. Split-thickness skin grafts remain the gold standard for the closure of large acute and chronic wounds. J Am Col Certif Wound Spec. 2011 Sep;3(3):55–9.

199. Norrmén C, Tammela T, Petrova TV, Alitalo K. Biological basis of therapeutic lymphangiogenesis. Circulation. 2011 Mar 29;123(12):1335–51.